SCUOLA DI DOTTORATO
UNIVERSITÀ DEGLI STUDI DI MILANO-BICOCCA

Department of Physics

PhD program in Physics and Astronomy Cycle XXXVI

Exploring Novel Scintillating Materials and Light Production Mechanisms for Next-Generation High Energy Physics Detectors

Surname: **Cala'** Name: **Roberto**

Registration number: 848345

Tutor: **Prof. Marco Paganoni**

Co-Tutor: **Dr. Etiennette Auffray**

Supervisor: **Prof. Marco Pizzichemi**

Coordinator: **Prof. Stefano Ragazzi**

ACADEMIC YEAR 2022/2023

Riassunto

I cristalli scintillatori hanno tradizionalmente trovato ampio impiego nell'ambito di precedenti esperimenti in fisica delle alte energie sia nei calorimetri omogenei, che in quelli a campionamento. Negli ultimi anni si sono registrati progressi significativi all'interno di gruppi di ricerca che lavorano con scintillatori, in particolar modo per ciò che riguarda nuovi processi ultra-veloci di emissione di luce e lo sviluppo di materiali innovativi. L'R&D in corso in questo ambito è di fondamentale importanza, in quanto è centrale per soddisfare le esigenti richieste dei futuri rivelatori progettati per collider ad alta luminosità, dove una straordinaria tolleranza alla radiazione incidente e timing ultraveloce sono parametri critici.

L'obiettivo di questa tesi di dottorato è sia esplorare il potenziale dei nuovi materiali scintillanti nell'ambito della fisica delle alte energie, sia concepire e testare prototipi destinati all'impiego in futuri esperimenti nei collider. I risultati di queste ricerche potrebbero apportare un contributo significativo allo sviluppo di rivelatori a cristalli innovativi e capaci di operare in modo efficace sia in ambienti a bassa che ad alta luminosità.

La ricerca si è concentrata sull'individuazione di cristalli scintillanti promettenti, e ha portato alla selezione dei BSO e BGSO come candidati per calorimetria dual-readout. Le campagne di caratterizzazione condotte su questi campioni hanno rivelato ottime prestazioni temporali per cristalli con frazione di Ge comprese tra il 30 % e il 50 %. Inoltre, sono state valutate le proprietà temporali dei campioni di BaF_2 dopati con ittrio a basse energie, rivelando una riduzione della componente lenta della scintillazione del BaF_2 senza un impatto significativo sulla cross-luminescenza. Questa emissione al di sotto del nanosecondo offre il potenziale per un timing preciso e una riduzione del pile-up in ambienti ad alta radiazione. Inoltre, sono stati testati scintillatori di perovskite organico-inorganico bidimensionali, i quali hanno mostrato risultati promettenti in termini di proprietà scintillanti e temporali.

Oltre ad indagare le proprietà dei cristalli, sono state esaminate le prestazioni temporali di vari materiali promettenti come rivelatori di particelle cariche di alta en-

ergia mediante simulazioni Monte Carlo e successivamente in campagne testbeam. Molti cristalli scintillatori, principalmente delle dimensioni di $2 \times 2 \times 10$ mm^3, sono stati accoppiati a fotomoltiplicatori al silicio (SiPM) e letti tramite elettronica ad alta frequenza per rivelare minimum ionizing particles (MIPs) di 150 GeV. Scintillatori standard come LSO:Ce,Ca, LYSO:Ce e GFAG, materiali cross-luminescenti come BaF_2 e BaF_2:Y, e cristalli che sfruttano la luce Cherenkov per il timing, come BGSO e $PbWO_4$, sono stati misurati e molti di essi hanno raggiunto una risoluzione temporale per singolo detector σ inferiore a 20 ps.

L'ultima attività intrapresa ha riguardato l'esplorazione della capacità di dual readout di un cristallo di $PbWO_4$ di grandi dimensioni utilizzando tubi fotomoltiplicatori (PMT), sia con che senza filtri ottici per discriminare tra la luce Cherenkov e la luce di scintillazione. L'obiettivo finale di questa indagine è di testare un metodo di discriminazione delle forme d'onda per estrarre dei parametri per compensare le perdite di energia nelle shower adroniche. Questa indagine è iniziata con simulazioni Monte Carlo, seguite dalla costruzione e test di un piccolo prototipo posto poi sul fascio e irraggiato con elettroni e pioni ad alta energia.

Abstract

Scintillating crystals have traditionally found extensive use in both homogeneous and sampling calorimeters in previous high-energy physics experiments. Recent years have witnessed significant advancements within the scintillator community, particularly concerning novel, fast light-emission processes and innovative materials. This ongoing R&D is of utmost importance as it is central to meeting the demanding requirements of future detectors designed for high-luminosity colliders, where exceptional radiation tolerance and ultra-fast timing performance are critical benchmarks.

The objective of this PhD thesis is both to explore the potential of emerging scintillating materials within the realm of high energy physics and to conceive and test small prototypes intended for deployment in future collider experiments. The outcomes of these investigations might lead to a substantial contribution to the development of innovative crystal-based detectors capable of operating effectively in both low and high count rates environments.

The R&D efforts focused on identifying promising scintillating crystals, leading to the selection of BSO and mixed BGSO crystals as candidates for dual-readout calorimetry. Characterization campaigns conducted on these samples unveiled optimal timing performance within the range of 30 % to 50 % Ge fractions. Additionally, the timing properties of yttrium-doped BaF_2 samples were evaluated at low energies, revealing a reduction in the slow component of BaF_2 scintillation without significant impact on the cross-luminescent component. This sub-nanosecond emission offers the potential for precise time tagging and reduced pile-up in high radiation environments. Furthermore, two-dimensional organic-inorganic perovskite scintillators were tested, demonstrating promising results in terms of both scintillating and timing properties.

Beyond the investigation of crystal properties, the timing performance of several promising materials as high-energy charged particle detectors was examined through Monte Carlo simulations and subsequently in testbeam campaigns. Many pixel scintillators, mainly sized at $2 \times 2 \times 10$ mm^3, were coupled with silicon photomultipliers (SiPMs) and read out using high-frequency electronics to detect 150 GeV min-

imum ionizing particles. Standard scintillators, such as LSO:Ce,Ca, LYSO:Ce and GFAG, cross-luminescent materials, like BaF_2 and BaF_2:Y, and crystals exploiting Cherenkov light for timing, such as BGSO and $PbWO_4$, were measured and many of them achieved a single-detector time resolution $\sigma < 20$ ps.

The last activity undertaken involved exploring the dual readout capacity of a sizeable $PbWO_4$ crystal employing photomultiplier tubes (PMTs), both with and without optical filters to discriminate between Cherenkov and scintillation light. The final objective of this endeavour was to investigate a pulse shape discrimination method for extracting valuable information to compensate for energy losses in hadronic showers. This investigation commenced with preliminary Monte Carlo simulations, followed by the construction and testing of a small prototype under high-energy electrons and pions.

Contents

Introduction **2**

I Theoretical Background **4**

1 Calorimetry **5**
1.1 Radiation-Matter Interaction . . . 6
1.1.1 Heavy charged particles . . . 6
1.1.2 Electrons and positrons . . . 7
1.1.3 Photons . . . 8
1.1.4 Radiation length . . . 9
1.2 Electromagnetic Showers . . . 10
1.3 Hadronic Showers . . . 11
1.4 Energy Resolution in Calorimeters . . . 14
1.5 Compensation Issue in Hadronic Calorimeters . . . 17
1.6 The Dual Readout Approach . . . 18
1.6.1 Analysis procedure . . . 19
1.7 The Vertex Reconstruction Problem in Harsh Radiation Environments 22
1.7.1 The Need for Charged Particles Timing Detectors . . . 22

2 The Scintillation and Cherenkov Mechanisms **26**
2.1 The Scintillation Mechanism . . . 27
2.2 Properties of the Scintillators . . . 28
2.2.1 Optical Properties . . . 28
2.2.2 Photoluminescence . . . 29
2.2.3 Light Yield, Light Output and Light Transport Efficiency . . . 29
2.2.4 Scintillation Kinetics . . . 30
2.2.5 Timing properties . . . 31
2.2.6 Radiation hardness . . . 31

2.3 Inorganic Scintillators . . . 32
2.4 Organic Scintillators . . . 33
2.5 Fast Light Emission Processes . . . 33
2.5.1 Cross-luminescence . . . 34
2.5.2 The Cherenkov Effect . . . 35

II Development and Characterization of Scintillators 38

3 Characterization Methods 39
3.1 Transmission . . . 39
3.2 Photoluminescence . . . 40
3.3 Light Output . . . 40
3.4 Scintillation Kinetics . . . 42
3.4.1 Scintillation Kinetics under X-ray Irradiation . . . 42
3.4.2 Scintillation and Cherenkov Kinetics under 511 keV γ-ray irradiation . . . 44
3.5 Coincidence Time Resolution (CTR) at 511 keV . . . 45

4 Mixed BGSO and BSO Crystals 49
4.1 BGO and BSO in the Scintillators Panorama . . . 49
4.2 Tuning Scintillation and Timing Properties: Mixed BGSO Crystals . . . 50
4.2.1 Samples . . . 50
4.2.2 Transmission Spectra . . . 51
4.2.3 Light Output and Energy Resolution . . . 53
4.2.4 Scintillation Kinetics under X-ray Excitation . . . 55
4.2.5 Coincidence Time Resolution at 511 keV . . . 59
4.3 Study of BSO Dual-Readout Capabilities . . . 62
4.3.1 Scintillation Kinetics and Cherenkov Yield at 511 keV . . . 64
4.4 Conclusions . . . 65

5 Cross-luminescent scintillators 67
5.1 Barium Fluoride State of the Art . . . 67
5.2 Suppressing BaF_2 STE Emission through Yttrium-doping . . . 69
5.2.1 Samples . . . 69
5.2.2 Transmission Spectra . . . 69
5.2.3 Light Output . . . 70
5.2.4 Scintillation Kinetics under X-ray Irradiation . . . 72
5.2.5 Coincidence Time Resolution at 511 keV and Vacuum-UV sensitive SiPMs . . . 75
5.3 Optical Filters for BaF_2 Cross-luminescent Light Selection . . . 78
5.3.1 Optical Filters and Measurement Conditions . . . 78
5.3.2 Emission-Time Delay Distributions . . . 78

5.3.3 Relative Light Output Estimation . . . 79
5.4 Cesium-based cross-luminescent materials development: $CsCaCl_3$ . . . 81
5.4.1 Sample and its Growing Process . . . 82
5.4.2 Radioluminescence . . . 82
5.4.3 Scintillation Kinetics under X-ray Irradiation . . . 84
5.4.4 Coincidence Time Resolution at 511 keV . . . 87
5.5 Conclusions and Outlook . . . 88

6 Hybrid Organic-Inorganic Perovskite Scintillators 90
6.1 State of the Art . . . 90
6.2 Undoped and Lithium-doped PEA_2PbBr_4 Crystals . . . 92
6.2.1 Crystallographic Structure and Samples . . . 92
6.2.2 Light Output . . . 93
6.2.3 Scintillation Kinetics under X-ray Excitation . . . 95
6.2.4 Coincidence Time Resolution at 511 keV . . . 96
6.3 Other $A_2B_{n-1}Pb_nX_{3n+1}$ ($n = 1,2$) HOIP Scintillators . . . 97
6.3.1 Coincidence Time Resolution at 511 keV . . . 98
6.4 Conclusions . . . 100

III Materials Investigation for MIPs Timing Detectors 102

7 Simulation Studies for MIPs Timing Detectors 103
7.1 Simulation Setup: Geometry, Radiation-Matter Interaction, Light Generation and Propagation . . . 104
7.2 Analog Pulse Production and Timestamp Extraction . . . 105
7.3 Simulated Materials and SiPMs . . . 106
7.4 Simulations Outputs . . . 107
7.4.1 Energy Deposition and Time Performance Evaluation . . . 107
7.4.2 LYSO:Ce Pixel Length Scan . . . 108
7.4.3 Time Resolution across Various Materials . . . 109

8 Testbeam Campaigns for Studies on Charged Particle Timing Detectors 112
8.1 Materials and Methods . . . 113
8.1.1 Testbeams Facility . . . 113
8.1.2 Testbeam Setups . . . 113
8.1.3 Materials Tested: Crystals and SiPMs . . . 116
8.2 Data analysis . . . 119
8.3 Results Discussion . . . 124
8.3.1 2022 Testbeam . . . 124
8.3.2 2023 Testbeam . . . 128
8.4 Measurements-Simulations Matching . . . 129

8.5 Conclusions 130

IV Studies on Dual Readout Calorimetry 133

9 Simulation Studies for Dual Readout Capability in $PbWO_4$ 134
9.1 The Simulation Framework 135
9.2 Dual Readout Capability in a Variable-size $PbWO_4$ Crystal 135
9.3 Key Features of the Simulated Pulses 137
9.4 Extrapolation of the f_{em} through machine learning techniques 140

10 Testbeam Campaigns for Dual-Readout Studies 143
10.1 Materials and Methods 143
10.2 Forward-backward Anisotropy Studies 144
10.3 Optical Filters Studies 147
10.4 Pulse Discrimination with R7600U-M4 PMT 148
10.4.1 Measurements-Simulations Matching 153
10.5 Conclusions and Outlook 153

V Conclusions and Outlook 156

Conclusions and Outlook 157

Bibliography 167

Acknowledgements 169

Introduction

Throughout the past century, Particle Physics has played a transformative role in advancing human understanding of the fundamental laws that govern the universe. This journey of exploration has been marked by a remarkable synergy between theoretical ideas and experimental observations, led by the joint collaboration between physicists and engineers from all over the world. It reached a pinnacle in 2012 with the discovery of the Higgs boson at the Large Hadron Collider (LHC) located at CERN, through the collaborative efforts of two multi-purpose experiments, CMS and ATLAS.

The Higgs boson's discovery aligns with the expectations of the Standard Model, which stands as the most comprehensive framework we have to describe three of the four fundamental forces in nature, namely the electromagnetic, weak, and strong forces. However, the Standard Model leaves unanswered some fundamental questions, including the mystery of the matter-antimatter imbalance in the universe. Consequently, the seek for hints into new physics via particle colliders demands either higher collision energies or increased statistical data via higher collision rates. Simultaneously, a sophisticated data analysis is essential to discern rare events from a dominating background.

Particle detectors are pivotal in the pursuit of new physics in future experiments. To address the challenges posed by the anticipated increase in particle flux at next-generation colliders, it is of great importance to conduct R&D on ultra-fast and radiation hard detector materials.

This PhD thesis focuses on exploring the potential of innovative scintillating materials and light generation mechanisms to meet the fundamental requirements of calorimetry at future particle colliders. This exploration encompasses investigations conducted at both the material level and the production of small prototypes measured in dedicated testbeam campaigns.

The work in this PhD thesis is organized into five parts:

- Part I provides an overview of calorimetry, introducing concepts such as the dual readout approach and MIP timing detectors, and light generation processes, including scintillation and Cherenkov emission;
- Part II details the research activities focused on scintillating materials tailored to the specific needs of detectors in future particle experiments;
- Part III presents studies conducted on charged particles timing detectors, beginning with the introduction of the Monte Carlo simulation framework developed and subsequently discussing the testbeam activities undertaken;
- Part IV showcases work done through Monte Carlo simulations and experimental measurements to investigate the dual readout capability in a lead-tungstate crystal ($PbWO_4$);
- Finally, Part V offers conclusions and a discussion of the next steps.

Part I

Theoretical Background

Chapter 1

Calorimetry

Calorimeters are a branch of particle detectors whose primary purpose is to measure the energy of an incident particle. A calorimeter traditionally consists of a block of material which absorbs a particle and its products generating a measurable signal related to the incoming particle energy [1, 2, 3]. Historically born for studies on cosmic rays [4], the interest in such detectors grew during the '60s for particle experiments in accelerators. One of the features that make calorimeters so attractive to the scientific community is their sensitivity to both charged and neutral particles, also resulting in the possibility to indirectly detect neutrinos via missing energy. Furthermore, calorimeters may be designed to provide further information, e.g. particle identification and position, through detector transverse and longitudinal segmentation.

The signal is proportional to the energy deposited by the shower produced by the incident particle in the active material for most of the calorimeters employed in collider experiments. The principle of signal generation in a calorimeter depends on its material: for instance, in scintillators-based calorimeters, it can be scintillation light, or when semiconductors or gas-sensitive materials are employed, it can be ionization charge.

Calorimeters are historically divided into two categories: homogeneous and sampling [5].

In homogeneous calorimeters, the entire detector is made of active material. They can achieve excellent energy resolution at the expense of cost and compactness. Both L3 $Bi_4G_3O_{12}$ (BGO) and CMS $PbWO_4$ (PWO) ECAL are examples of homogeneous calorimeters [6, 7].

In sampling calorimeters, the detector also comprises a passive absorber alternating

with layers of active materials. Compared to the homogeneous ones, they are more compact due to the high density and stopping power of the passive material. However, only a fraction of the energy deposited is converted into a detectable signal, thus worsening the energy resolution. Examples are the CMS Cu-plastic scintillators hadronic calorimeter and ATLAS metal-liquid Argon calorimeter [8, 9].

Due to the different matter interaction mechanisms of electrons and photons compared to hadrons, calorimeters are usually designed and optimized for either electromagnetic (ECAL) or hadronic particle (HCAL) detection. However, the utilization of a single calorimeter for electrons, photons and hadrons detection may be beneficial, as discussed in [10, 3].

This introductory chapter initiates by offering insights into the fundamental physical processes governing calorimetry. It commences with a discussion of the theoretical framework surrounding radiation-matter interactions and then proceeds to explore the distinctive characteristics of electromagnetic and hadronic showers. Additionally, the concept of energy resolution within a calorimeter and the main parameters for its determination are presented. The chapter also delves into the challenge of hadronic shower compensation and elaborates on the dual readout approach designed to address this challenge in a comprehensive manner. To conclude, it provides an overview of the issue related to vertex position reconstruction in high-dose environments and illustrates the solution implemented by the CMS experiment through the incorporation of a charged particle timing detector.

1.1 Radiation-Matter Interaction

1.1.1 Heavy charged particles

Charged particles are known to ionize the medium in which they pass through. The mass stopping power (i.e. the energy loss dE over the distance dx per unit of density) depends on the particle momentum as illustrated in Figure 1.1 and can be modelled through the Bethe-Bloch formula [11]:

$$\langle -\frac{dE}{dx} \rangle = K z^2 \frac{Z}{A} \frac{1}{\beta^2} \left[\frac{1}{2} \ln \left(\frac{2 m_e c^2 \beta^2 \gamma^2}{I} \right) - \beta^2 - \frac{\delta(\beta\gamma)}{2} \right]. \tag{1.1}$$

The particle energy loss mechanism occurs through multiple collisions inside the material. For such reason, the thinner the traversed medium, the wider the distribution of the energy lost by the incoming charged particle (Landau-Vavilov distribution) becomes.

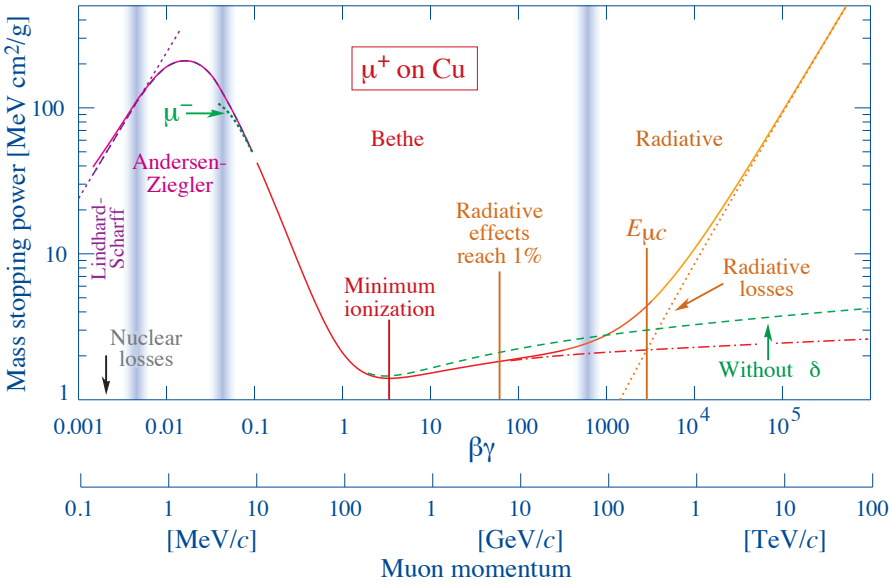

Figure 1.1: Mass stopping power $\langle -dE/dx \rangle$ for muons in copper. From reference [11].

1.1.2 Electrons and positrons

The ionization process for electrons and positrons differs from the one described by the Bethe-Bloch formula due to their mass, which is identical to that of their targets, and the interchangeability with the electrons ionized. The dependency on the incoming particle energy is the following:

$$\langle -\frac{dE}{dx} \rangle_{ion} \propto \log(E). \tag{1.2}$$

Besides ionization, electrons and positrons may run into several other processes (e.g. Møller scattering, Bhabha scattering, positron annihilation), as shown in Figure 1.2. The dominant process at high energies is given by the bremsstrahlung, whose linear energy loss grows proportionally to the particle energy. In such process, a photon is emitted by the electron or positron which is deflected in a nucleus electric field [5, 11].

To describe the development of an electromagnetic shower, it can be helpful to introduce the critical energy E_c, defined as the energy at which the ionization and bremsstrahlung losses are equal. The critical energy can be empirically evaluated at the few percent level as [11]:

$$E_c = \frac{610 \text{ MeV}}{Z + 1.24} \qquad \text{for solids and liquids,} \tag{1.3}$$

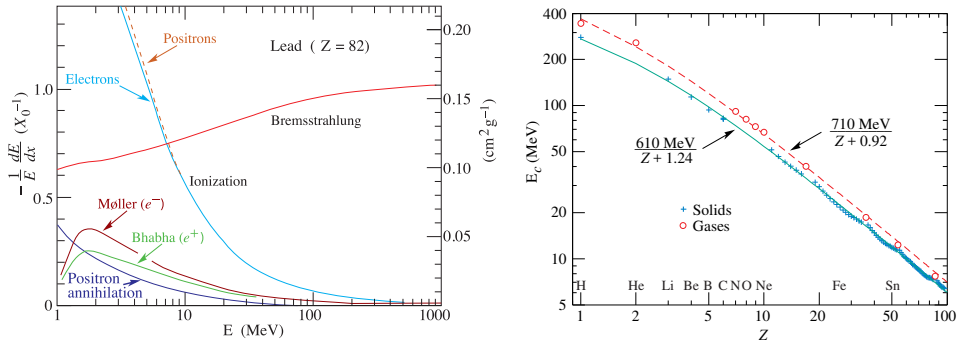

Figure 1.2: Electrons and positrons energy loss processes (left) and their critical energy dependency from Z in solids and gases (right). From reference [11].

$$E_c = \frac{710 \text{ MeV}}{Z + 0.92} \qquad \text{for gases.} \tag{1.4}$$

1.1.3 Photons

Photons may lose energy in a medium through different processes (see Figure 1.3):

Photoelectric effect ($\sigma_{p.e.}$), in which the photon is completely absorbed by an atom, with a consequent electron ejected;

Rayleigh scattering ($\sigma_{Rayleigh}$), in which the photon scatters elastically on an atom changing its direction;

Compton scattering ($\sigma_{Compton}$), in which the photon shares part of its energy with an electron bonded to an atom and changes its direction;

Pair production on nuclei or electrons (k_{nuc}, k_e), in which the photon creates a e^+e^- pair;

Photonuclear interaction ($\sigma_{g.d.r.}$), in which the photon breaks the target nucleus.

The contributions to the photon cross section may vary significantly between light and heavy elements, as shown in Figure 1.3. However, in general, the photoelectric effect is the dominant one at the low-end of the energy spectrum (below a few hundreds of keV), Compton scattering cross section is the highest in the middle region (from few hundreds of keV to few MeV) and pair production dominates at higher energies.

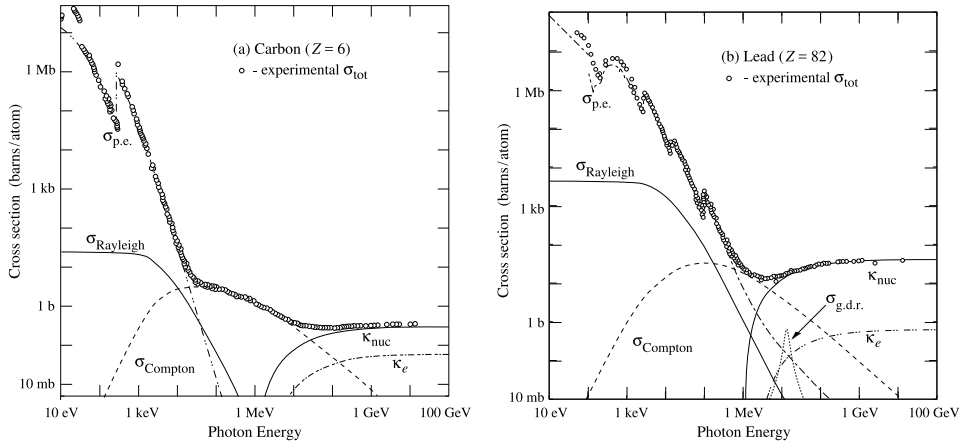

Figure 1.3: Photons interaction cross sections in carbon (left) and lead (right). From reference [11].

1.1.4 Radiation length

The parameter which describes the mean path of both high-energy electrons and photons for losing their energy in a medium is given by the radiation length X_0. It is the average distance traversed by an electron to reduce its energy by a factor $1/e$ via bremsstrahlung emission or 7/9 of the average travel length for a photon to create an e^+e^- pair [11]. The radiation length can be evaluated as:

$$X_0 = \frac{716.4 \cdot A}{Z(Z+1)\ln\left(\frac{287}{\sqrt{Z}}\right)} \quad \mathrm{g/cm^2}. \tag{1.5}$$

In a mixture or compound the radiation length can be approximated as:

$$\frac{1}{X_0} = \sum \frac{w_i}{X_i}, \tag{1.6}$$

where w_i and X_i represent the mass fraction and the radiation length of the i-th component, while in an object composed of multiple materials, it can be estimated as:

$$\frac{1}{X_0} = \sum \frac{V_i}{X_i}, \tag{1.7}$$

where V_i and X_i are the volume fraction and radiation length of the i-th material.

1.2 Electromagnetic Showers

When a high-energy photon, electron or positron travels through a medium, it generates a cascade process in which a large amount of secondary particles is produced. Energetic electrons and positrons release energy by generating bremsstrahlung photons, while photons by producing e^+e^- pairs. Therefore bremsstrahlung and pair production energy losses create a circular mechanism leading to the development of an electromagnetic particle shower inside the material. The secondary particle production stops when electrons and positrons are slowed down below the critical energy for which the energy losses due to the material ionization are higher than those due to radiation emission [3].

The quantity which describes the longitudinal development of an electromagnetic shower is the radiation length X_0, defined as the mean distance needed by an electron to reduce its energy to a factor $1/e$ through bremsstrahlung emission. On the other hand, the mean distance taken by a photon to occur in a e^+e^- conversion is $\frac{9}{7}X_0$, leading to a slightly retarded shower start with respect to electrons or positrons. Nevertheless, for both particles, the average longitudinal profile of a shower can be analytically described with a Γ distribution:

$$\frac{dE}{dt} = E_0 \cdot b \cdot \frac{(bt)^{a-1}e^{-bt}}{\Gamma(a)}, \tag{1.8}$$

where E_0 is the energy of the primary particle, $t = x/X_0$ the distance from the shower starting point in X_0 units, $b \simeq 0.5$, $\alpha = bt_{max} + 1$ and t_{max} is the position where the distribution reaches its maximum. The shower maximum longitudinal position moves logaritmically with E_0, as shown in Figure 1.4, and occurs at:

$$t_{max} = \log(E_0/E_c) - 0.5 \qquad \text{for } \mathrm{e}^{\pm}, \tag{1.9}$$

$$t_{max} = \log(E_0/E_c) + 0.5 \qquad \text{for } \gamma. \tag{1.10}$$

An electromagnetic shower also develops transversally due to electrons' multiple scattering with nuclei's Coulomb electrical field. The quantity which governs the transversal size of an electromagnetic shower is the Molière radius, defined as:

$$R_M = \frac{1}{m_e c^2 \sqrt{4\pi/\alpha}} \cdot \frac{X_0}{E_c} = 21.1 \text{ MeV} \cdot \frac{X_0}{E_c}. \tag{1.11}$$

Differently from the radiation length, the Molière radius is less material dependent. On average, 90% of the shower is contained within a cylinder of radius R_M, while 95% of it is within a $2R_M$ cylinder. In a similar fashion as described for the radiation

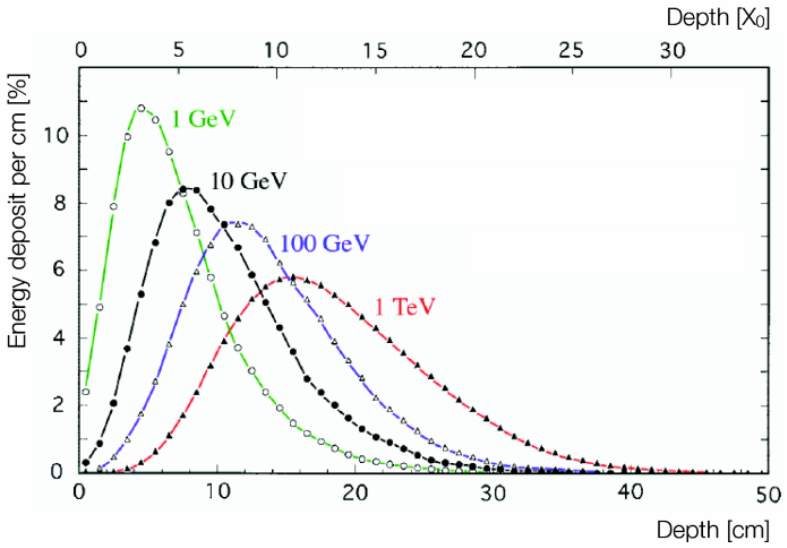

Figure 1.4: Longitudinal shower profiles for showers generated by electrons with different energies in copper. On the horizontal axes, both depth in cm and X_0 units are given, while the fraction of energy deposited per cm by the showering particles is provided on the vertical axis. From reference [3].

length, if the absorbing material is composed of a mixture of elements with different X_0^i and critical energies E_c^i, the effective Molière radius may be evaluated as

$$\frac{1}{R_M} = \frac{1}{E_c} \sum \frac{w^i E_c^i}{X_0^i}, \tag{1.12}$$

where w_i is the mass fraction of the i-th element. For a calorimeter made of several different materials, the effective Molière radius is calculated weighting on the volume fractions V_i:

$$\frac{1}{R_M} = \frac{1}{E_c} \sum \frac{V^i E_c^i}{X_0^i}. \tag{1.13}$$

1.3 Hadronic Showers

Because of their different nature, hadrons interact with matter in a significantly different and more complicated way compared to electrons, positrons and photons [12, 5, 3]. When a charged hadron traverses a medium, atoms ionization will occur in a continuous stream of events. However, after travelling for a certain path, the hadron may interact strongly with an atomic nucleus. The effect of this nuclear reaction opens a wide range of possibilities with the result of a drastic change in the hadron

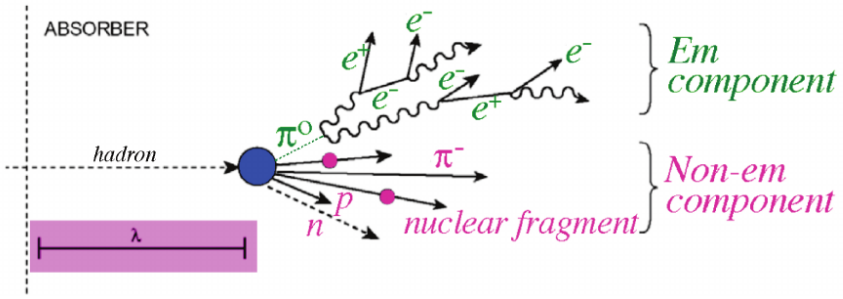

Figure 1.5: Simple schematic model of a hadronic shower development. Incident hadron may run into a wide range of processes leading to a complex response of the calorimeter. From reference [3].

identity and the production of one or more secondary particles. On the other hand, the neutral hadrons do not ionize the traversed material, making nuclear interactions the only processes through which they may lose their energy. Furthermore, a large fraction of the primary hadron energy can be lost both for breaking the nuclear binding energy or through non-detectable neutrinos production: these processes do not bring energy deposition inside the detection and contribute to the "invisible-energy" of the calorimeter.

The particles generated after the first nuclear interaction can release their energy both through medium ionization and new induced strong interactions with other nuclei, thus enhancing a cascade of secondaries to be produced and a shower to be developed (see Figure 1.5). The main particles produced by strong interactions are pions and nucleons. On average, about one-third of the secondaries produced are π^0s, which create electromagnetic showers within the hadronic one through decay channels such as $\pi^0 \to \gamma\gamma$.

Similarly to electromagnetic showers, a quantity which measures the longitudinal development of a hadronic shower can be defined: the interaction length λ_I in a medium is the average distance needed for a hadron to reduce its energy to a factor $1/e$ via inelastic interactions and can be evaluated as:

$$\lambda_I = \frac{A}{\sigma_{inel} \cdot \rho \cdot N_{Av}} \simeq 35 \cdot A^{1/3} \ \ \mathrm{g/cm^2}, \tag{1.14}$$

where $\sigma_{inel} \propto A^{2/3}$ is the cross section for inelastic collisions for protons. The longitudinal development of a hadronic shower can be described through a sum of Γ distributions with the form of Eq. 1.8, representing the purely electromagnetic component of the shower, convoluted with a decreasing exponential function modelling the purely hadronic shower profile. The shower maximum longitudinal position depends logarithmically on the energy and its value (in λ_I units) can be approximately

calculated through the empirical formula:

$$t_{max}^{had} \simeq 0.2 \cdot \log E(\text{GeV}) + 0.7. \tag{1.15}$$

The mean transverse momentum of the secondary particles also causes a transverse development of the shower with 95% of its energy contained within a cylinder of radius $R_{had} \simeq \lambda_I$.

Due to the significant energy losses in nuclear fragmentation processes and undetected neutrinos, the signal generated by a hadronic shower is intrinsically lower with respect to an electromagnetic shower created by primary particles with identical energy. The quantity introduced to account for this difference in a calorimeter is the e/h ratio, where e and h represent the responses generated by electromagnetic and hadronic showers, respectively. This ratio depends solely on the intrinsic characteristics of the calorimeter, such as its materials, geometry, and signal generation mechanisms, and remains independent of the incident particle's energy. The ratio e/π between the signal produced by electrons and charged pions of the same energy can provide an energy-dependent indirect measurement of the e/h ratio as follows:

$$\frac{e}{\pi}(E) = \frac{e/h}{1 + (e/h - 1) \cdot f_{\text{em}}(E)}, \tag{1.16}$$

in which $f_{\text{em}}(E)$ is the average fraction of energy associated with the electromagnetic component of the shower. An example of f_{em} distribution in a shower generated by a 150 GeV π^- and its dependence on energy is shown in Figure 1.6. The energy dependence of f_{em} was studied in detail both theoretically and experimentally, leading to the following approximated expression:

$$f_{\text{em}}(E) = 1 - \left(\frac{E}{E_0}\right)^{k-1}, \tag{1.17}$$

where E_0 is a scale factor corresponding to the average energy needed for producing one pion (usually 0.7 - 1.0 GeV), while $k - 1$ can vary between 0.8 and 0.9 and depends on the average multiplicity of mesons generated by an interaction and the average fraction of π^0 produced in the reactions.

In many circumstances, segmenting a calorimeter in sections for separate electromagnetic and hadronic particle detection may result more effective. The increased complexity in hadronic shower development makes it significantly more challenging to achieve good energy resolution values in hadronic calorimeters compared to electromagnetic ones due to the larger volumes required and the higher intrinsic fluctuations. Furthermore, the large amount of material needed to contain hadronic showers require the development of more sophisticated and cost-effective technologies to allow good performance in hadron energy measurement.

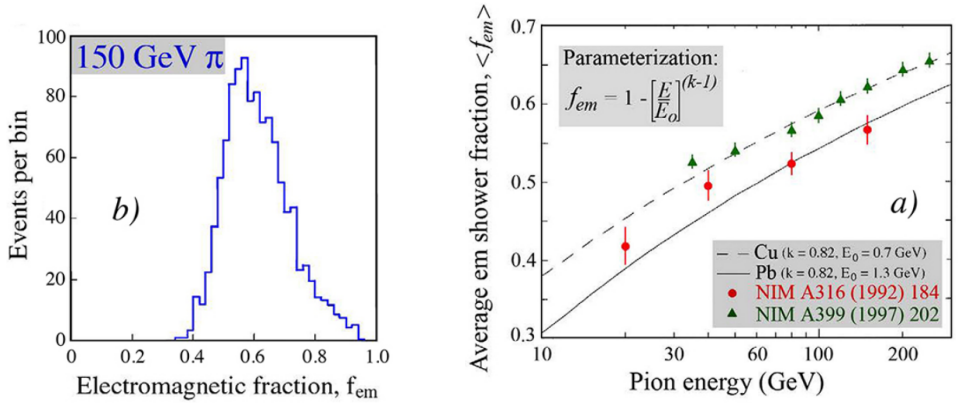

Figure 1.6: Left: distribution of the electromagnetic fraction f_{em} in a hadronic shower generated by 150 GeV π^- in lead. Right: evolution of the average f_{em} with energy for showers developing in copper and lead both measured experimentally in [13, 14] and theoretically evaluated from Eq. 1.17. From reference [15].

Besides the measurement of single hadrons, in high energy particle colliders hadronic calorimeters should also provide a precise measurement of particle jets. Accurate measurement of jet energies and their transverse momentum is of utmost significance for numerous physics analyses. However, jets represent a serious hurdle for hadronic calorimeters since they are composed of many particles (e.g. hadrons, neutrons, muons, neutrinos and electromagnetic particles) interacting with matter through a wide spectrum of processes. The performance of jets measurements in hadronic calorimeters may be improved through ad-hoc strategies, e.g. the particle flow approach [16].

1.4 Energy Resolution in Calorimeters

If a monochromatic beam of energy E_0 is shoot on a calorimeter, the output signal will be a distribution of a measurable quantity with a certain width related to the nature of the calorimeter and of the incident beam. There are two key properties defining the response of a calorimeter: linearity and resolution.

The signal proportionality to the energy of the incoming particle makes the calorimeter response linear. It is crucial for a good calorimeter to exhibit a linear response in the energy range of particles it is supposed to measure. This may be a difficult task in some cases, since many sources related to the nature of the calorimeter itself and the instrumentation employed for signals detection may contribute to a non-linear response. Linearity may become a serious issue, especially for hadronic showers as they

have an energy-dependent electromagnetic fraction. This problem may be overcome through strategies, known as compensation techniques, which will be introduced in Section 1.5.

The resolution of a calorimeter is usually defined as the ratio between the standard deviation and the average of the energy distribution. The fluctuations of a calorimeter response depend on the particle energy and can be divided according to their origin in a stochastic or sampling term s, scaling with $1/\sqrt{E}$, a noise term n, depending on the energy as $1/E$, and an energy independent constant term c [17]. Therefore the energy resolution of a calorimeter can be parametrized as the sum in quadrature of these contributions:

$$\frac{\sigma_E}{E} = \frac{s}{\sqrt{E}} \oplus \frac{n}{E} \oplus c, \tag{1.18}$$

where E is in GeV. This is a simplified way to model the dependency of the resolution of a calorimeter on energy, which may be different, especially for hadronic calorimeters.

The **sampling** term s takes into account all the statistical fluctuation sources such as [17]:

Shower fluctuations. They are intrinsic to the probabilistic process of the shower development and related to the number of particles N generated as

$$\frac{\sigma_E}{E} \propto \frac{\sigma_N}{N} \propto \frac{1}{\sqrt{N}}, \tag{1.19}$$

according to Poisson statistics.

Photostatistics fluctuations. In light-based calorimeters, the amount of photons N_{pe} produced and detected is affected by Poissonian fluctuations as follows:

$$\frac{\sigma_E}{E} \propto \frac{\sigma_{N_{pe}}}{N_{pe}} \propto \frac{1}{\sqrt{N_{pe}}}. \tag{1.20}$$

Such contribution can be neglected for processes in which a large amount of photons is generated. However, it may become dominant for calorimeters in which only a low number of photons is generated (e.g. detectors exploiting Cherenkov emission).

Sampling fluctuations. In sampling calorimeters, only part of the energy deposited by the shower is measured, leading to further statistical fluctuations. Given the thickness t in radiation length units of the active material and the sampling fraction f_{samp} of the calorimeter, defined as the ratio between active material and absorber, the following dependence was observed [15]:

$$\frac{\sigma_E}{E} \propto \sqrt{\frac{t}{f_{samp}} \cdot \frac{1}{E}}. \tag{1.21}$$

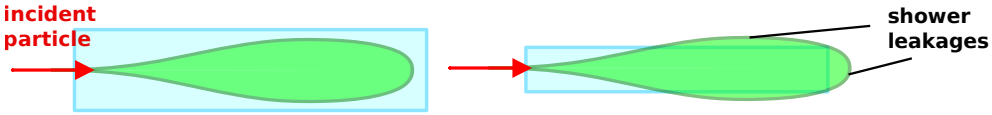

Figure 1.7: Left: representation of a calorimeter in which a shower is fully contained. Right: longitudinal and transversal shower leakage in a small-size calorimeter.

Landau fluctuations. They arise in thin active layers in which the energy loss distribution is described by a highly-skewed Landau-Vavilov distribution instead of a Gaussian one. Such contribution is usually negligible in solid and liquid calorimeters but may be largely significant for gaseous detectors (even above 10%) [17].

Track length fluctuations. Secondary particle scattering at different angles thus travelling through different absorber thicknesses. Therefore event-by-event fluctuations around the mean emission angle affect the response of the calorimeter.

Fluctuation in hadronic showers. As already discussed before, the hadronic shower is formed by an electromagnetic and hadronic part. The electromagnetic fraction f_{em} of a shower depends on the energy and the large and non-Poissonian variations in f_{em} significantly affect the energy resolution of the calorimeter. This contribution gets more prominent the more the ratio e/h differs from 1. This is the reason why hadronic calorimeters exhibit a much worse energy resolution with respect to electromagnetic calorimeters.

The term n independent of the particle energy accounts for electronic **noise**. A source of noise at room temperature is given by the thermal agitation of charge carriers inside a conductor, whose fluctuations sum to the output signal in a way independent of the particle energy.

Finally, all contributions that are proportional to the particle energy are grouped in a **constant** term c, thus being the dominant ones at high energies. Possible energy proportional sources may be:

Shower leakages, either longitudinally or transversally, which affect the energy reconstruction of the incident particle (see Figure 1.7).

Response non-uniformity of the calorimeter, due to calibration error, inhomogeneities, or non-linear response of the electronics.

In the design of a calorimeter, it is crucial to identify and evaluate all these contributions to minimize them and mitigate their impact on the detector resolution.

1.5 Compensation Issue in Hadronic Calorimeters

As previously discussed, the response for hadronic and electromagnetic particles is not the same in a calorimeter due to the nature of the detector. The quantity that provides an estimation of such response difference is given by the e/h ratio, whose value can be extrapolated by measuring e/π signal ratios at various energies. In most of cases, calorimeters exhibit e/h values larger than 1 due to the "invisible-energy" loss in hadronic showers. In such a case, the calorimeter is referred to as undercompensating. Nonetheless, some hadronic calorimeters may exhibit $e/h < 1$, meaning that they are overcompensating, within particular conditions. In both cases, the calorimeter presents a non-linear response to hadrons due to f_{em} dependence on energy [15].

To overcome this issue, a sampling calorimeter may be idealized tuning geometries and active materials in such a way that e/h is forced to be 1 (compensated calorimeter). e/h calculation requires an accurate evaluation accounting for the contributions of each type of particle generated in the hadronic shower. In formulae, the response to hadrons h may be parametrized as:

$$h = f_{ion} \cdot I + f_n \cdot N + f_\gamma \cdot \Gamma + f_B \cdot B, \tag{1.22}$$

where f_{ion}, f_n, f_γ and f_B are the fraction of ionizing particles, neutrons, and photons produced from nuclear reactions and nuclear binding energy, while I, N, Γ and B represent the response for each kind of particle. Therefore, through accurate geometry and materials choices, it is possible to overcome the undercompensation issue (e.g. exploiting hydrogen to amplify neutrons response).

As shown in Figure 1.8, the response of typical calorimeters to the electromagnetic shower component not only differs from that of the hadronic component but even from the response to minimum ionizing particles (MIPs). The reason for such disparity is related to the fact that electromagnetic shower composition changes going deeper in the calorimeter and, in the late stages, most of its energy is released via soft γs interacting either through Compton scattering or photoelectric effect. In conventional calorimeters, the sampling fraction (i.e. the fraction of energy contributing to the detectable signal) for such component is very different from that of the MIPs which populate the early stage of the shower development. The quantity which measures such a discrepancy is the ratio e/mip. A $e/mip \neq 1$ may have significant implications for certain aspects of calorimeter performance, even if the calorimeter is designed to be compensating ($e/h = 1$).

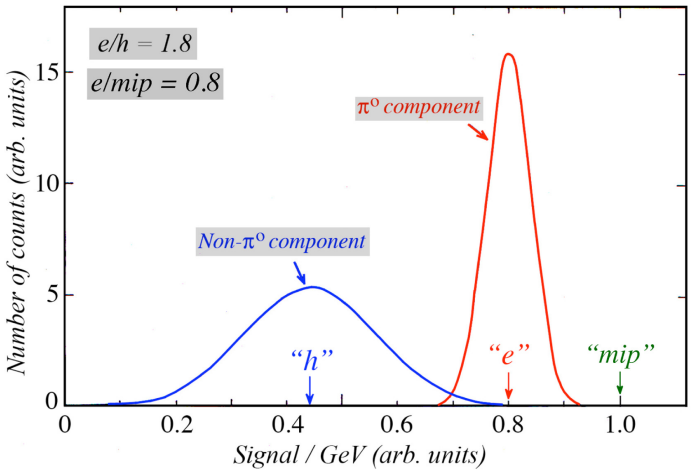

Figure 1.8: Distributions of the signal per unit deposited energy for both the electromagnetic and non-electromagnetic components of the hadron showers, normalized to the response for minimum ionizing particles ("*mip*"). The average values of the electromagnetic and non-electromagnetic distributions represent the electromagnetic response ("*e*") and the non-electromagnetic response ("*h*") of the calorimeter. From reference [15].

1.6 The Dual Readout Approach

One of the main drawbacks brought by the compensation approach is given by the need for high-Z absorber material (e.g. lead or uranium), which may lead to a e/h equal to 1 by reducing the response for electromagnetic showers and increasing the one for neutrons. However, the small e/mip value achieved for these materials (usually ~ 0.6) brings large response non-linearities for low-energy hadrons, since these particles mainly lose energy through ionization of the absorber medium, rather than shower development (see Figure 1.9). This mainly affects the resolution of high-energy jets such as the ones generated in the hadronic decay of the W and Z intermediate vector boson, since a large fraction of their energy is produced through low-energy hadrons.

Besides hardware compensation strategies to restore a linear response to hadrons, an alternative is provided by the measurement of the f_{em} event-by-event. A possible technique named the dual readout approach was investigated by the DREAM collaboration and exploits the Cherenkov light produced in the shower [19, 20]. This method takes advantage of the fact that the Cherenkov light is mostly generated in the electromagnetic part of a hadronic shower. This happens because electrons and positrons are relativistic for energies higher than ~ 200 keV. In contrast, the protons generated in nuclear reactions which dominate the purely hadronic part of the shower are non-relativistic.

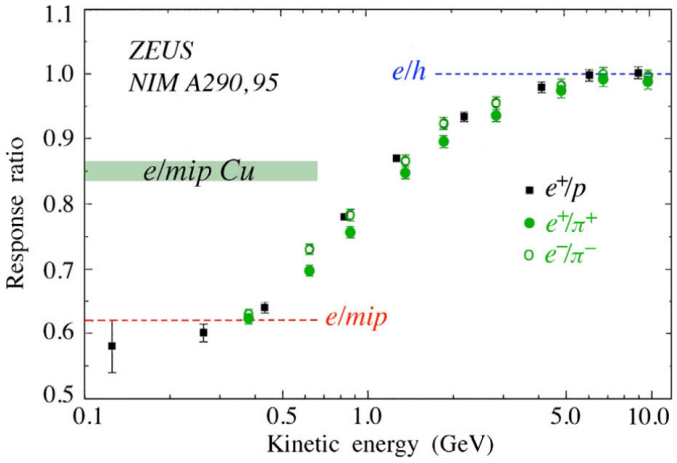

Figure 1.9: The response ratio of the compensating ZEUS calorimeter to electrons and (low-energy) hadrons is equal to 1.0 for energies above GeV. However, at low energies, the hadron response increases due to the absence of nuclear interactions and the consequent losses in nuclear binding energy. The experimental data are from [18]. From reference [15].

Therefore, by comparing the signals coming from scintillation and Cherenkov light, it is possible to reconstruct the electromagnetic fraction of the event and obtain the total shower energy using the e/h value of the calorimeter.

1.6.1 Analysis procedure

As previously discusses, a calorimeter meant for dual readout produced two separate signals for scintillation $\langle S \rangle$ and Cherenkov $\langle C \rangle$. It is possible to easily calibrate both signals with electrons of energy E so that $\langle S \rangle = \langle C \rangle = E$ and the calorimeter response for electromagnetic showers is $R_{em} = \langle S \rangle / E = \langle C \rangle / E = 1$. On the other hand, for hadronic showers, the output signals account for an electromagnetic shower component and a non-electromagnetic one which contributes with different weights, in formulae:

$$S = E \left[f_{\text{em}} + \frac{1}{(e/h)_S} (1 - f_{\text{em}}) \right], \tag{1.23}$$

$$C = E \left[f_{\text{em}} + \frac{1}{(e/h)_C} (1 - f_{\text{em}}) \right]. \tag{1.24}$$

In general, $f_{\text{em}} < 1$, resulting in a hadronic response different from 1 and smaller reconstructed energy.

Plotting the experimental data points for hadrons showers in a C/E vs S/E graph, a straight line connecting the point $[(h/e)_S, (h/e)_C]$, corresponding to $f_{\text{em}} = 0$, to

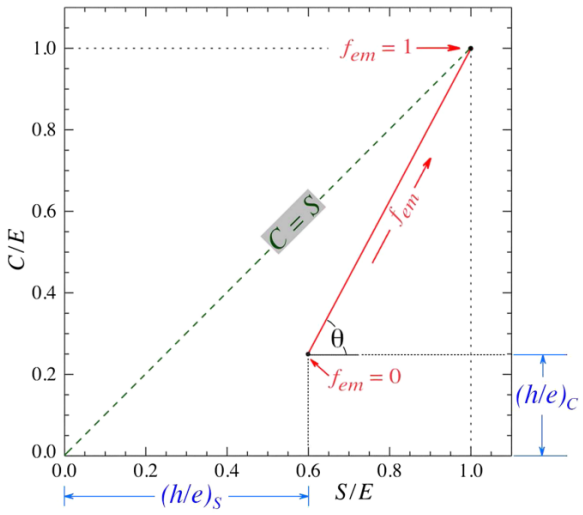

Figure 1.10: The data points for hadron showers detected with a dual-readout calorimeter are situated along the straight red line providing a graphical representation of Equations 1.23 and 1.24. On the other hand, the data points for electromagnetic showers in this calorimeter are clustered around the intersection point of this line with the $C = S$ line, i.e. the point (1,1). From reference [20].

the point (1,1), for $f_{\text{em}} = 1$ is obtained, while the points for electromagnetic showers group around this second position (see Figure 1.10).

Once the e/h values are extrapolated from this plot, the f_{em} can be evaluated combining Equations 1.23 and 1.24 as:

$$f_{\text{em}} = \frac{(h/e)_C - (C/S)(h/e)_S}{(C/S)\,[1 - (h/e)_S] - [1 - (h/e)_C]}. \tag{1.25}$$

The slope of the line in Figure 1.10 around which the data points are located only depends on the $(e/h)_S$ and $(e/h)_C$ values and are energy-independent. The more $(e/h)_S \neq (e/h)_C$, i.e. the red line distances from the $C = S$ bisector, the better the method works. Defining the parameter independent by energy:

$$\chi = \cot\theta = \frac{1 - (h/e)_S}{1 - (h/e)_C}, \tag{1.26}$$

the energy of a particular hadron shower can be reconstructed from the measured scintillation and Cherenkov signals as:

$$E = \frac{S - \chi C}{1 - \chi}. \tag{1.27}$$

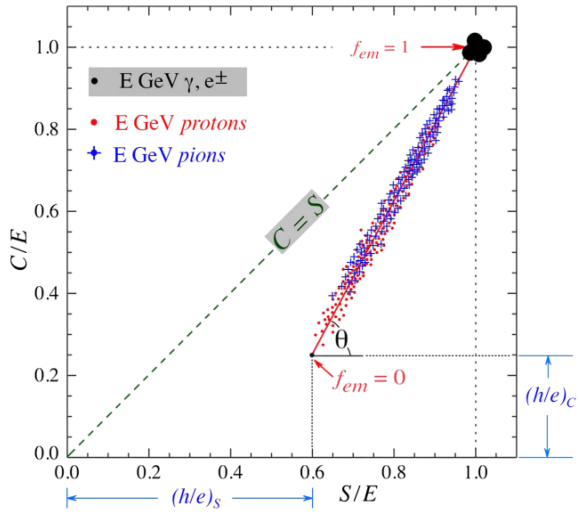

Figure 1.11: The S-C diagram represents the signals from a generic dual-readout calorimeter. The data points corresponding to both protons and pions events are concentrated along the straight red line. Nonetheless, the data points for protons and pions exhibit distinct distributions due to differences in the electromagnetic shower fraction. From reference [20].

Curiously, signals distributions produced in a dual readout calorimeter by pions, protons, and kaon beams of the same energy share the same average despite different f_{em} distributions produced by their shower. An example of this phenomenon can be observed in Figure 1.11, demonstrating that Equation 1.27 can be universally employed for all types of hadrons and for jets.

Dual readout is therefore an interesting approach allowing the elimination of some drawbacks of intrinsically compensating calorimeters such as the high-Z absorber requirement and stringent geometries to tune the detectors sampling fraction.

1.7 The Vertex Reconstruction Problem in Harsh Radiation Environments

Many of the future colliders are expected to achieve extremely high luminosities: as an example, the LHC will enter the high luminosity era (known as HL-LHC) in 2027 which will provide about 20 times more data with respect to Run 2 [21]. The parameters that determine the luminosity reached by a collider are the number of particles per bunch N_1 and N_2, their transverse sizes σ_x and σ_y, the frequency of revolution f of these bunches and their number N_b, and they are related as follows [22]:

$$\mathcal{L} = \frac{N_1 N_2 f N_b}{4\pi\sigma_x\sigma_y}. \tag{1.28}$$

In order to increase the luminosity to $\sim 10^{35}$ cm^{-2}s^{-1}, the LHC is going to reduce the bunches' transverse dimensions to increase their collision rate. As a result, the amount of proton-proton collisions will be between 140 and 200 for each bunch crossing. Such a large amount of collision pile-up will generate an increase in the spatial overlap of tracks, seriously challenging the reconstruction algorithms.

1.7.1 The Need for Charged Particles Timing Detectors

As studied in detail by the CMS collaboration [23], the knowledge of precise timing information for tracks may bring large benefits in reducing the pile-up effects. The reason behind this lies in the fact that the individual collisions in every bunch crossing are slightly time spread. As a matter of fact, the bunches usually are a few centimetres long, meaning that some nanoseconds are required to fully traverse one with the other. An example of a distribution of vertices within a bunch crossing is represented in Figure 1.12, where, for the HL-LHC, a $\sim$ 4.5 cm and 180 - 200 ps spatial and time RMS spread is predicted [21]. Through a time information knowledge with the precision of 30 - 40 ps it would be possible to divide the beam spot into consecutive time clusters reducing the number of vertices per exposure to $\sim$ 40 (see Figure 1.13). To face such a harsh pile-up environment, a possible solution may be to add an ad-hoc timing detector in front of the calorimeter for minimum ionizing particles (MIPs) measurement from charged particles with excellent time resolution. This represents the solution offered by the CMS MIP Timing Detector (MTD), whose resolution is expected to be 30 - 40 ps [23].

This kind of detector may be beneficial for several reasons:

> **Mitigation of pile-up**. As previously discussed, this represents the main advantage brought by a MIP timing detector. Such reduction also improves event reconstruction and isolation of photons and lepton and the resolution of the missing transverse momentum.

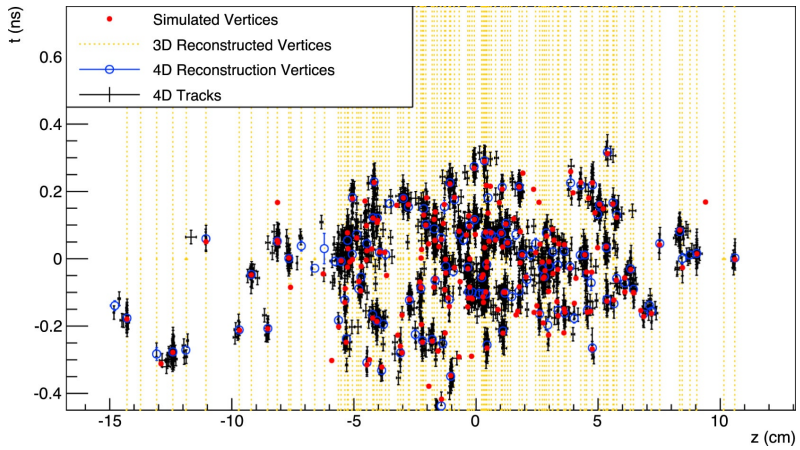

Figure 1.12: Simulated and reconstructed vertices in a bunch crossing with 200 pileup interactions, considering a MIP timing detector with approximately 30 ps time resolution covering the barrel and endcaps. The red dots represent the simulated vertices, while the vertical yellow lines indicate 3D-reconstructed vertices (without using timing information). Instances of vertex merging are visible throughout the display in the 3D-reconstructed vertices. The black crosses and blue open circles represent tracks and vertices reconstructed using a method that incorporates the time information, referred to as "4D". With the use of time information, many of the vertices that appeared merged in the spatial dimension are now clearly separated. From reference [23].

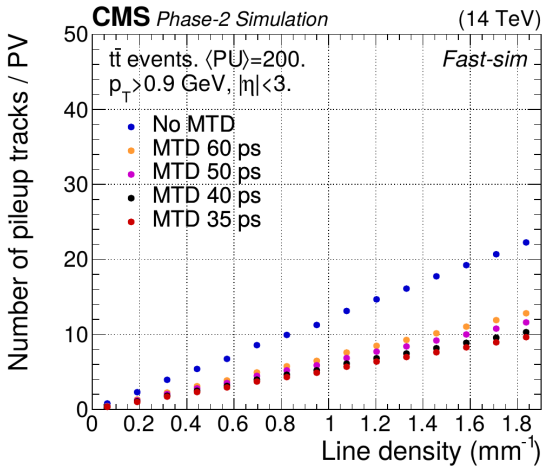

Figure 1.13: Number of pile-up tracks misassociated with the hard interaction vertex plotted against the collision line density for various MIP timing detectors' time resolutions. From reference [23].

Identification of charged hadrons using the time-of-flight information (e.g. for pions, kaons or protons). This is possible for transverse momenta up to a few GeV bringing benefits on the heavy ions physics and proton-proton collisions QCD studies.

Potential search for long-lived particles (LLP) predicted by some physics beyond the Standard Model. A timing detector can provide the enhanced capability to obtain their relativistic velocity β, and, under certain conditions, reconstruct their mass, through displaced vertices precise time measurement.

Chapter 2

The Scintillation and Cherenkov Mechanisms

Scintillation is a luminescence phenomenon originating from ionizing radiation in transparent dielectric media [24]. Such a process may occur in different ways depending on the medium considered. However, in general, scintillators contain luminescence centers that, when excited, return to their ground state emitting radiation. A large variety of scintillators are employed for different applications including particle physics, medical imaging, radiation detection, homeland security and defence and astrophysics.

Scintillating materials can be in solid, liquid or gaseous state and most of them can be gathered in two categories based on their chemical composition: inorganic and organic scintillators.

Besides scintillation, a further light-generation mechanism commonly exploited for calorimetry application is Cherenkov radiation. The Cherenkov effect is an almost-prompt light production process which occurs whenever a charged particle travels through a dielectric medium with a velocity higher with respect to the speed of light in that medium.

This chapter commences by offering a comprehensive overview of the scintillation mechanism, highlighting its fundamental physics. It proceeds to discuss the common properties shared by scintillators. The chapter then delves into the distinct characteristics of both inorganic and organic scintillators and concludes with a description of some fast light emission processes such as cross-luminescence and Cherenkov radiation.

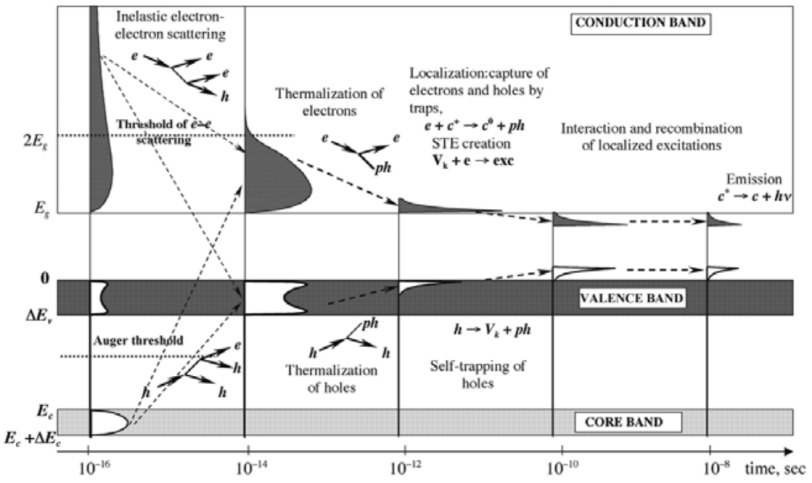

Figure 2.1: Illustrative representation of relaxation and thermalization of electrons and holes in a scintillator. From reference [24]

2.1 The Scintillation Mechanism

As already mentioned above, scintillators are traditionally classified based on their chemical composition into inorganic and organic. Inorganic scintillators can exhibit luminescence either intrinsically or through the introduction of luminescent ions via doping. Organic scintillators produce luminescence through the transitions of free valence electrons occupying molecular orbits.

The luminescent properties of scintillating crystals are a result of their band structure, where only specific energy levels are permitted within the crystal. The scintillator crystalline structure includes a core band, a valence band and a conduction band, each containing other sub-bands. The region between the conduction and valence bands is known as the bandgap, and commonly referred to as the "forbidden gap" (see Figure 2.1).

When energetic particles interact with a scintillator, some atoms in the material are ionized and "hot" electrons are freed from their bound state. Each generated "hot" electron experiences electron-electron scattering and Auger processes within the material. These interactions result in the generation of additional electron-hole pairs through inelastic scattering with electrons from the scintillator lattice. This continues until the electron's energy decreases below the ionization threshold, which is typically twice the bandgap energy. While a substantial number of electrons and holes are produced during this process, they still possess excessive kinetic energy to

occupy the luminescence centers.

In the subsequent step, both electrons and holes undergo thermalization via phonon scattering, which are essentially lattice vibrations. The energy they lose during this phase does not contribute to the eventual production of scintillation light in the crystal and is, in this sense, dissipated. This thermalization process continues until the electrons reach the lower portion of the conduction band and the holes reach the upper part of the valence band.

At this point, electrons and holes are localized through interactions with defects and impurities present in the crystal. As a result, electrons and holes become trapped by various types of traps or through self-trapping mechanisms. Depending on the specific trap, these excited states can persist and remain trapped for a relatively extended period, often on the order of hundreds of nanoseconds or even longer, before recombination occurs. Ultimately, electrons and holes will recombine, either through non-radiative or radiative processes. Radiative recombination results in the emission of scintillation light with a wavelength corresponding to the bandgap of the crystal. Non-radiative recombination also takes place within the scintillator, leading to energy losses.

This description outlines the scintillation process in an ionic crystal. However, two distinct categories of scintillators are noteworthy: one containing rare earths, exemplified by LSO and LYSO doped with Ce, which is not crucial for this thesis work, and the other featuring core-valence luminescence, such as BaF_2, discussed more in detail in Section 2.5 [24].

2.2 Properties of the Scintillators

As described in the previous section, the scintillation process results in the generation of light within the crystal. The various steps in the propagation of this light, from its generation to the point at which it is detected by the photodetector, play a crucial role in shaping the fundamental characteristics of the scintillator. This section delves into the discussion of these important properties.

2.2.1 Optical Properties

The light generated in a scintillator has to travel inside the material in order to reach the photodetector and produce a detectable signal. Passing through the medium, the emitted photons may run into some processes, which mainly are absorption, Fresnel reflections and Rayleigh scattering. The probability of these effects depends on some properties of the material such as its refractive index, bandgap width and amount of defects in its lattice. It is possible to quantify these effects by measuring the intensity I of light through the scintillator with a monochromatic beam of intensity I_0 and

wavelength λ as

$$T(\lambda) = \frac{I(\lambda)}{I_0(\lambda)}. \tag{2.1}$$

This quantity is defined as the transmission of the scintillator and it is usually measured using a spectrophotometer providing a monochromatic beam of variable wavelength.

A further parameter which is of interest for scintillators is absorbance, defined as:

$$A(\lambda) = -\log_{10} T(\lambda). \tag{2.2}$$

Transmission and absorbance spectra may offer insights into luminescence centers in the material.

2.2.2 Photoluminescence

Differently from scintillation in which the luminescence centers' excitation is induced by ionizing radiation, photoluminescence is the emission of optical photons induced by light-excitation of a dielectric medium.

The wavelength distribution of the emitted photons in a scintillator is referred to as the photoluminescence emission spectrum. In order to provide an overview of the energy levels involved in scintillation, the excitation spectra, i.e. the distribution obtained varying the excitation at a fixed emission wavelength, are usually provided with emission ones.

2.2.3 Light Yield, Light Output and Light Transport Efficiency

The capability of a scintillator to convert the energy released in the material by ionizing radiation to a detectable light is of key importance. The average amount of light quanta produced per MeV of energy deposited is named the light yield of the scintillator.

The measurement of light yield is challenging due to light trapping inside the material for total internal reflection. This phenomenon occurs whenever a photon reaches the interface between the scintillator and a second medium with a lower refractive index with an incidence angle larger than:

$$\theta_l = \arcsin\frac{n_2}{n_1}, \tag{2.3}$$

where n_1 and n_2 are the refractive indexes of the scintillator and the external medium respectively.

For this reason, the quantity which is most quoted is the light output, defined as the number of photons detected out at one surface of the scintillator per MeV of energy deposited. The ratio between light output and light yield gives the light transport efficiency (LTE) of the scintillator, which depends on factors including the index of refraction, internal defects and inhomogeneities, geometry and surface state of the sample.

Some precautions in the measuring processes may be adopted to improve light extraction from a scintillator, some of which are:

Surface polishing. It allows a more efficient light transport towards the readout detector avoiding photons diffusion of the surface.

Wrapping. Whenever a photon reaches a surface with an incident angle lower than θ_l, it is refracted and escapes the scintillator. For this reason, the utilization of reflective materials like Teflon to wrap the samples may be instrumental in reflecting back those photons and increasing their chance to be detected.

Sample-detector coupling. The employment of optical greases or glues between the sample extraction face(s) and the detector(s) with refractive intermediate refractive indices between the two is beneficial in increasing the critical angle at the extraction surface, resulting in a larger amount of detected photons.

Surface polishing, wrapping and optical couplings act both decreasing the average path travelled by a photon in the material, i.e. reducing self-absorption probability, and increasing its chance of reaching the photodetector. As a result, the LTE improves significantly [25].

2.2.4 Scintillation Kinetics

The time evolution of the scintillation intensity $f(t)$ is a relevant aspect of a scintillator. Due to the fast dynamics of the first part of the scintillation process, the intensity of emission $f(t)$ grows exponentially with one or more rise time constants $\tau_{r,i}$ of $\sim\ 10^{-12} - 10^{-11}$ s. The emission maximum is reached close to the moment when all the luminescence centers are filled. Then $f(t)$ decreases exponentially with behaviour depending on the number of excited luminescence centers N_i for each component, their relative intensity R_i and their decay constants $\tau_{d,i}$. A first-order order formula to describe $f(t)$ is given by sums of bi-exponential functions as:

$$f(t|\theta) = \Theta(t-\theta)\sum_{i=1}^{N} R_i \cdot \frac{e^{-(t-\theta)/\tau_{d,i}} - e^{-(t-\theta)/\tau_{r,i}}}{\tau_{d,i} - \tau_{r,i}}, \tag{2.4}$$

where θ is the scintillation process starting time and Θ is the Heavyside function.

In the case of multiple luminescence centers with different decay times, a figure of merit that describes the de-excitation part of the scintillation kinetics is provided by

the effective decay time $\tau_{d,eff}$, defined as:

$$\frac{1}{\tau_{d,eff}} = \sum_{i=1}^{N} \frac{R_i}{\tau_{d,i}}. \tag{2.5}$$

2.2.5 Timing properties

Good timing performance is more and more becoming a crucial requirement in recent years in many different applications. As an example, time resolutions below $\sim$ 20 ps are required for spurious events rejection in the high luminosity environments expected at future colliders or time-tagging of O(10 ps) precision would bring huge benefits for metabolic images reconstruction in Time-of-Flight Positron Emission Tomography (TOF-PET) [26, 27].

The timing of a scintillating detector is a measurement of the precision to reconstruct the incident particle interaction moment. This measurement is performed by assigning a timestamp to the signal generated event by event. Commonly used techniques for timestamp extraction include leading edge discrimination, where the timestamp is determined when the signal pulse crosses a predefined amplitude threshold, and constant fraction discrimination (CFD), where such threshold is set at a certain fraction of the pulse amplitude.

It can be proven that the time resolution achieved by a scintillator, defined as the standard deviation σ_t (for high energy physics applications) or the full-width-at-half-maximum FWHM_t (for medical applications) of the timestamps distribution, depends on the light output LO and the rise and decay times τ_r and τ_d of the scintillator as follows:

$$\sigma_t \quad \text{or} \quad \mathrm{FWHM}_t \propto \sqrt{\frac{\tau_r \tau_d}{LO}}. \tag{2.6}$$

This means that to achieve good timing, a scintillator should have both fast emission kinetics and high light output.

2.2.6 Radiation hardness

A further property of scintillators is given by their radiation tolerance. The interaction of ionizing radiation with the crystal lattice inevitably alters the composition of the material producing new traps and defects, which may be of different nature. As a result, the properties of the material may degrade in several ways. The light yield can be reduced due to new color centers formation resulting in new absorption bands or due to defects reducing the mobility of charge carriers and the pair recombination efficiency. Besides this effect, the characteristics of emitted light, e.g. emission peaks and decay time, may be influenced by the interaction of ionizing radiation with the luminescence centers. A further effect produced by high energy hadron ionization

is the activation of the scintillating material, generating induced radioactivity and background phosphorescence.

The capability of a scintillator to preserve its properties unchanged after irradiation is referred to as radiation hardness. This is not a well-defined quantity, since many parameters contribute to its evaluation. For the majority of the inorganic scintillators, radiation damage may lead to a loss in transmission as the main effect. Such a loss is often quantified by measuring the radiation-induced absorption length spectrum in wavelength defined as:

$$K(\lambda) = \frac{1}{L} \log \frac{T_{\text{before}}(\lambda)}{T_{\text{after}}(\lambda)}, \tag{2.7}$$

being L the thickness of the sample traversed a monochromatic beam, and T_{before} and T_{after} its transmission before and after irradiation.

High luminosities expected in future colliders will generate a huge amount of ionizing radiation and deliver large doses to the particle detection system. For such a reason, radiation hard materials investigation is becoming of crucial importance in calorimetry.

2.3 Inorganic Scintillators

Inorganic scintillators are usually crystalline materials which contain an activator impurity. In such a case, the scintillation process derives from the electronic band structure of the crystal.

Within these scintillators, the electron-hole recombination may, in some cases, be intrinsic, occurring directly within the material bandgap. However, for most materials, their inherent scintillating properties may not be sufficient. As a result, they are doped with an activator that serves as a luminescent center within the crystal lattice. These activators, typically rare earth ions (e.g., Ce^{3+}), create intermediate energy levels in the forbidden band, leading to a reduction in the bandgap.

Inorganic scintillators usually are dense materials composed of high-Z elements, making them suitable for high stopping power applications. At a first order, the light yield coming from ionizing radiation of energy E_0 is given by [28]:

$$LY = \frac{E_0}{\beta E_g} \cdot S \cdot Q, \tag{2.8}$$

being E_g the scintillator band gap, βE_g the energy needed on average for an e-h pair creation, S the energy transport efficiency to the luminescence centers and Q their radiative efficiency at a given temperature. Since some of these parameters like S may depend on the ionization density, a different LY may be achieved varying ionizing particles.

2.4 Organic Scintillators

Organic scintillators are a kind of scintillating material that consists of aromatic hydrocarbon compounds containing embedded benzene ring structures. In these materials, ionizing radiation excites valence band electrons, whose relaxation produces a visible or ultra-violet photon. The time scale of this process is within a few nanoseconds, so faster with respect to inorganic scintillators.

These materials can be either plastic or liquid depending on their composition. Plastic scintillators consist of a hosting polymer matrix, usually made of polystyrene, containing organic scintillating components. Plastic scintillators are widely employed due to their low production cost, versatility and tunability. They can achieve light outputs up to 10 000 ph/MeV and decay times between hundreds of ps and few ns. The typical density of these compounds is slightly above 1 g/cm^3 and their Z_{eff} is also low. For these reasons, these materials are often employed for particle detection and sampling calorimeters, but they are not suited for applications requiring high stopping power, e.g. homogenous calorimeters or gamma spectroscopy.

Light output of plastic scintillator is not uniform, but decreases with ionizing density as follows [29]:

$$\frac{dL}{dx} = L_0 \frac{dE/dx}{1 + k_B \cdot dE/dx}, \tag{2.9}$$

being dL/dx the luminescence per unit of length, dE/dx the energy deposited by ionization per unit of length, L_0 the luminescence at a fixed low ionization density and k_B a scintillator-dependent parameter named Birks' constant. Scintillation kinetics and light output in plastic materials might significantly depend on the ionizing particle type. Such property can be employed for some particle identification applications using pulse shape analysis.

2.5 Fast Light Emission Processes

As already discussed in the previous two sections, the conventional scintillation mechanisms in inorganic materials are unlikely to produce emission kinetics in the ns scale, while organic compounds can achieve the ns scale at the cost of low light yield and stopping power. The production of prompt or almost-prompt photons may be of large interest for high-dose timing applications.

In the following, two key examples of fast emission processes, i.e. cross-luminescent scintillation and Cherenkov radiation mechanism, will be presented and discussed.

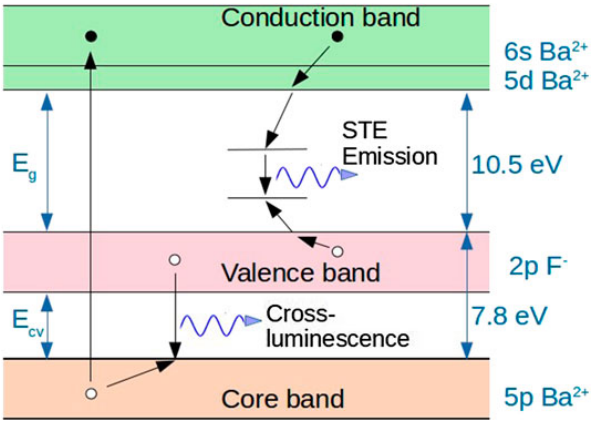

Figure 2.2: Illustrative representation of the band-gap diagram for BaF_2 along with corresponding emission mechanisms. From reference [34]

2.5.1 Cross-luminescence

Cross-luminescence, also referred to as core-valence luminescence [30, 31] or Auger-free luminescence [32, 33], is a scintillation process in which an electron is excited from the core to the conduction band. The scintillation process is due to the recombination of the resulting hole in the core band with an electron in the valence band (see Figure 2.2).

This process can be observed only if the bandgap E_{cv} between the bottom of the valence band and the top of the core band is sufficiently large and where the energy difference E_g between the conduction and the valence bands is larger than E_{cv} [30, 31, 32, 33]. If the material does not exhibit the latter, the crystal would reabsorb its own cross-luminescent light with the result of electrons excitation from the valence to the conduction band. The e-h pairs produced in this way would then recombine either radiatively via "standard" scintillation or non-radiatively. A further obstacle to cross-luminescence in such a case is given by non-radiative Auger recombination, which is a much faster process and therefore probabilistically much more enhanced.

For such a reason, materials exhibiting cross-luminescence usually have a large E_g with the result of luminescence in the deep UV. The cross-luminescent mechanism is extremely fast, with a decay time ranging from a few ns down to hundreds of ps. The reason for this lies in the fact that the number of electrons with whom a hole can be paired is much larger in the valence band with respect to the conduction band. Therefore, the recombination probability is higher and the scintillation kinetics is faster.

In a cross-luminescent material, the bandwidth of the emitted light is strictly related

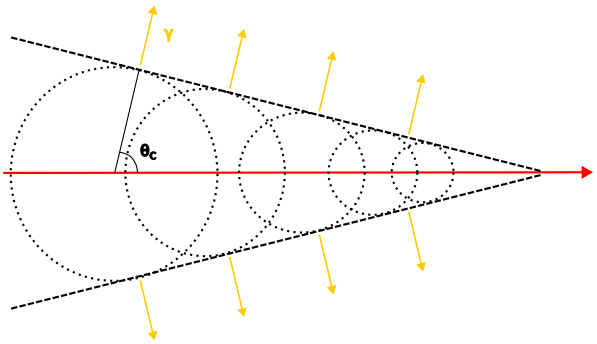

Figure 2.3: The Cherenkov light produced by a charged particle is emitted at a fixed angle θ_c given by its velocity v and the refractive index of the medium n.

to the bandwidth of the valence band. In fact, holes in the core band can recombine with electrons of any of the sub-bands contained in the valence band, producing different emission reflecting the density of states in the valence band.

2.5.2 The Cherenkov Effect

As already introduced at the beginning of this section, Cherenkov radiation is a prompt light production process which may be beneficial for many timing applications. This phenomenon was discovered and explained in 1934 by the scientist Pavel Alekseyevich Cherenkov.

Whenever a charged particle traverses a dielectric medium with a velocity higher with respect to the light velocity in that medium, such particle generates a perturbation of the material electromagnetic field which propagates as Cherenkov light. Given the velocity of the particle v and the refractive index of the medium n, the Cherenkov photons are emitted if

$$v > \frac{c}{n} = v_{lim}. \tag{2.10}$$

The photons are emitted at an angle

$$\cos\theta_c = \frac{c}{nv}, \tag{2.11}$$

with respect to the charged particle direction (see Figure 2.3).

The number of photons emitted per unit wavelength $d\lambda$ and per unit path length dL of the particle is expressed by the following equation

$$\frac{d^2N_{ph}}{dLd\lambda} = 2\pi\alpha z^2 \frac{1}{\lambda^2} \cdot \left(1 - \frac{c^2}{n^2 v^2}\right), \tag{2.12}$$

being $\alpha = 1/137$, z the charge of the particle in units of e and λ the wavelength of the photon. This equation shows a dependence of the number of Cherenkov photons generated with $1/\lambda^2$, meaning that the light emission is mostly in the UV region.

Comparing Cherenkov radiation with scintillation light two differences of crucial importance can be noted:

- the number of Cherenkov photons is, in general, much lower with respect to the number of photons produced in a scintillation process for the same amount of energy deposited
- differently from scintillation being an isotropic process, the Cherenkov process is highly non-isotropic since the emitted photons are produced along a cone with an opening angle of θ_c around the axis of motion of the particle.

The advantage that makes Cherenkov radiation extremely suitable for applications in high luminosity environments is its almost-prompt emission [35, 36, 37, 38]. These results in time signals which are much shorter with respect to those produced by scintillating materials.

Part II

Development and Characterization of Scintillators

Chapter 3

Characterization Methods

The part dedicated to the development and characterization of scintillators in this thesis begins with a comprehensive description of the test benches utilized to measure the essential characteristics of the materials under investigation.

The following chapter commences with an overview of the test benches designed for measuring sample transmission and photoluminescence spectra. It then introduces the bench employed to evaluate the light output of the materials. Following that, the chapter elaborates on the test benches used to investigate the scintillation kinetics of the samples. These setups involve the use of either X-ray or 511 keV gamma irradiation. In conclusion, an overview of the test bench specifically designed for assessing the timing performance of two crystals detected in coincidence, known as the Coincidence Time Resolution (CTR) setup, is provided.

3.1 Transmission

The transmission spectra were measured using a Perkin Elmer Lambda 650 UV/VIS spectrophotometer whose main parts are shown in Figure 3.1. The instrument is provided with two lamps, a halogen-tungsten one operating between 314 and 900 nm and a deuterium lamp working down to 190 nm. Their light passes through a monochromator and then split into two branches. One of the monochromatic light beams, whose intensity can be tuned by means of an iris, traverses the crystal sample placed on a moving stage. The other beam is instead employed to monitor instrumentation drift during the acquisition. Both beams are focalized on a photomultiplier measuring their intensity.

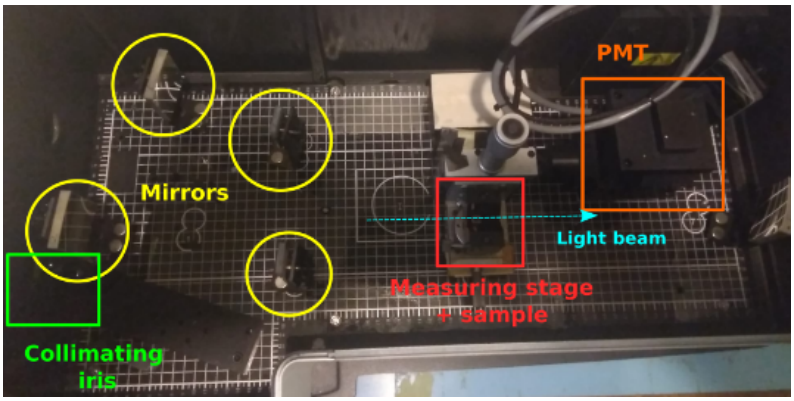

Figure 3.1: Picture of the instrumentation employed to measure crystal samples' transmission.

3.2 Photoluminescence

The photoluminescence emission spectra were measured with a Perkin Elmer LS55 spectrofluorimeter. A monochromatic beam with a tunable wavelength is produced by the instrument and directed towards the sample. The photoluminescence light intensity is then measured in output at 90° as a function of the wavelength. Some filters can also be employed to reduce the intensity of the detected light.

3.3 Light Output

The light output measurements were performed using photomultiplier tubes located in a light-tight box kept at 18 °C (see Figure 3.2) and connected to a DT5720A CAEN digitized via an attenuator. The digitizer works in charge integration mode on a tunable gate.

The photomultipliers employed are a Hamamatsu R2509, operated at 2500 V and mainly sensitive to blue light, and a Hamamatsu H6610, biased at 2100 V and used for UV light detection. Their quantum efficiency spectra are plotted in Figure 3.3.

The samples are usually Teflon-wrapped on all faces except the one coupled to the PMT. Several sources may be employed for their excitation, with ^{137}Cs (662 keV) being the reference one.

For the light output evaluation of a sample, a preliminary acquisition has to be realized to identify the ADC channel corresponding to the signal due to single photoelectron events. Then the following equation can be employed to estimate the light output of

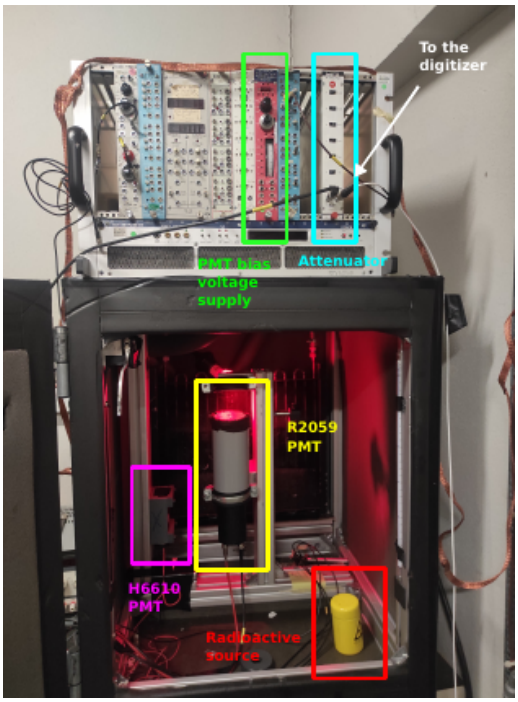

Figure 3.2: Picture of the setup employed to measure crystals' light output.

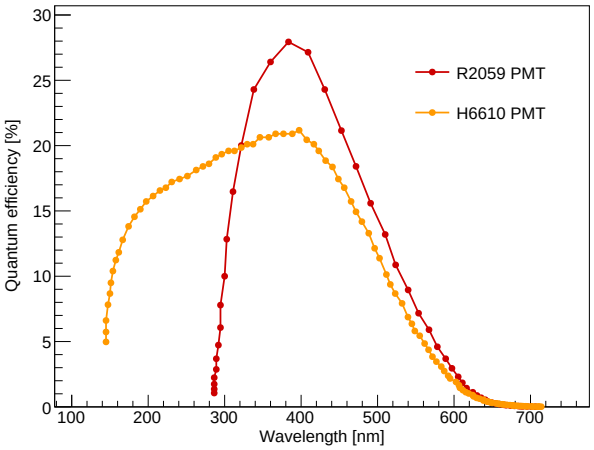

Figure 3.3: Quantum efficiencies of the Hamamatsu R2059 and H6610 PMTs from datasheets.

the sample:

$$LO = \frac{1}{E_\gamma} \frac{\mu_{\text{sample}} \times C_{\text{sample}}}{\mu_{\text{sphe}} \times C_{\text{sphe}}} \times 10^{A/20} \times \frac{1}{\langle QE \rangle}, \tag{3.1}$$

being E_γ the energy of the ionizing photon, μ_{sample} and μ_{sphe} the position in ADC channels of the sample photopeak and the single photoelectron peak respectively, C_{sample} and C_{sphe} the charge sensitivity values of the digitizer for the sample and single photoelectron measurements, A the attenuation in decibel and $\langle QE \rangle$ the average quantum efficiency of the sample.

3.4 Scintillation Kinetics

In order to measure the emission kinetics of the samples, two test benches were employed, the former exploiting X-ray as irradiation source, the latter 511 keV γ-rays irradiation. Both setups exploit a Time Correlated Single Photon Counting (TCSPC) technique to determine the time-emission profiles of the samples by measuring the time of emission of single scintillation photons [39, 40, 41].

In a TCSPC setup, a start detector opens a time window in which an event may occur. Then another photodetector acts as a stop detector giving the moment in which a photon produced by the sample under test is detected. The time delay distribution is a convolution between the impulse response function (IRF) of the setup and the emission time distribution of the sample.

3.4.1 Scintillation Kinetics under X-ray Irradiation

In the first test bench, a PicoQuant Pulse Diode Laser (PDL 800-B) emitting at 405 nm provides the start signal through an external trigger and acts as an excitation source of a Hamamatsu X-ray tube (XRT N5084) with a Tungsten anode. The tube is biased at 40 kV and provides X-rays within a 0 - 40 keV continuous energy spectrum with a mean energy of about 9 keV. The X-ray beam is therefore directed towards the sample under test after crossing a brass collimator. The scintillation light is collected in reflection mode by a Hybrid Photomultiplier tube from Berker & Hickl (HPM 100-07) working in TCSPC mode. The signal in output from the HPM is processed by an ORTEC amplifier and timing discriminator (Model 9237) and acted as a stop detector of the scintillation photons' arrival at a Time to Digital Converter (TDC). A picture of the setup is provided in Figure 3.4.

The IRF of the setup is obtained through the convolution of the pulse laser response, the X-ray tube response and the HPM single photon time resolution. The IRF FWHM is about 160 ps (see Figure 3.5).

A more detailed description of the test bench is given in [42].

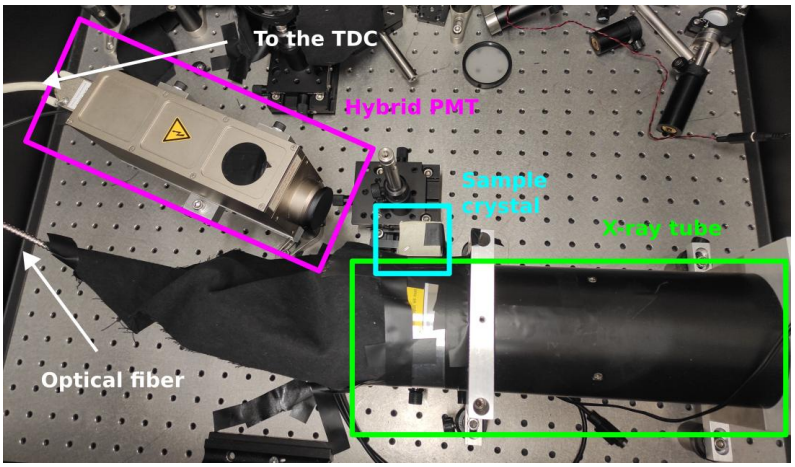

Figure 3.4: Picture of the setup for scintillation kinetics measurements under X-ray irradiation.

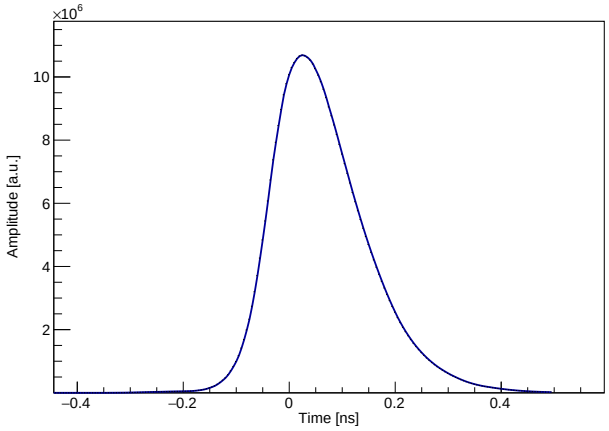

Figure 3.5: Impulse response function (IRF) of the test bench exciting the samples through X-ray irradiation. Its FWHM is about 160 ps.

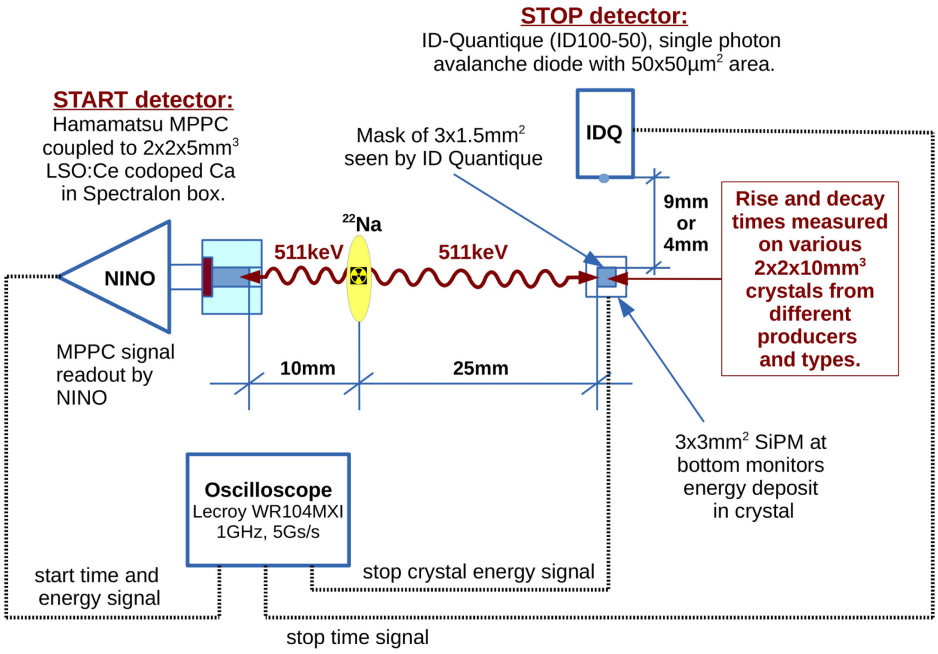

Figure 3.6: Schematic of the TCSPC setup measuring the scintillation and Cherenkov kinetics under 511 keV γ-rays irradiation. From reference [42].

3.4.2 Scintillation and Cherenkov Kinetics under 511 keV γ-ray irradiation

A second test bench measuring samples emission kinetics exploits the two back-to-back emitted 511 keV γ photons created by the annihilation of a positron resulting from the β^+ decay of a ^{22}Na source. Setup and instrumentation are shown in Figure 3.6 described in detail in [42, 43].

The start detector is a $2 \times 2 \times 5$ mm^3 LSO:Ce,0.4%Ca wrapped in several layers of Teflon and coupled to a Hamamatsu S13360-3050CS SiPM using a thin layer of Cargille Meltmount glue ($n = 1.58$). The signal produced by the SiPM is split into two branches: the former is fed into a NINO ASIC ultrafast discriminator [44] to extract the time information, and the latter is used to collect the energy deposition.

A single photon avalanche diode (SPAD) with 50×50 mm^2 active area produced by ID-Quantique (IDQ100-50) acts as a stop detector for the light emitted by the sample. Such a SPAD was chosen for its low dark rate (down to 20 Hz) and narrow IRF. Additionally, the energy detected out of the sample at each coincidence event is measured through a 3×3 mm^2 Ketek SiPM (PM3350) placed below the sample.

In order to measure the IRF of the detection chain, a $2 \times 2 \times 5$ mm^3 PbF_2 sample black-painted on all surfaces except the one facing the IDQ was employed. PbF_2 does not scintillate but produces a large amount of Cherenkov radiation compared to many other materials due to its high refractive index and large transparency range. The black paint is employed both to shield the IDQ from light emitted by the Ketek SiPM epoxy layer and to suppress internal reflections inside the crystal. Being Cherenkov a prompt light emission process, this method allows to precisely determine the IRF of the detection chain. The IRF can be well-described by a Gaussian function with a 52 ps standard deviation.

3.5 Coincidence Time Resolution (CTR) at 511 keV

The coincidence time resolution (CTR) measured at 511 keV is among the main figures of merit of a time-of-flight PET scanner. It is usually expressed in terms of FWHM of the delay distribution between the detection time of two back-to-back 511 keV photons emitted by positron annihilation. Through CTR measurements it is possible to evaluate and compare the timing performance of different samples and materials.

A test bench described in detail in [45, 46] was employed for CTR measurements (see Figures 3.7 and 3.8). A ^{22}Na source emitting a positron via β^+ decay is placed between two crystals read out by SiPMs. A sample may be measured either against a reference sample of known CTR contribution or in coincidence with an identical one. Usually, the samples are wrapped in several layers of Teflon and coupled with Cargille Meltmount glue to a SiPM. Similarly as in the reference detector used in the setup exploiting 511 keV γ-rays irradiation for scintillation and Cherenkov kinetics measurements, the SiPMs' signals are split in a first branch read out by discrete custom-made high-frequency electronics [47, 46] for the time signal measurement and a second one read out by an analog operational amplifier for the energy signal. The pulses are then digitized using a LeCroy DDA735Zi oscilloscope with 3.5 GHz bandwidth and 20 Gs/s sampling rate. Some features of interest of the pulses, e.g. amplitude, charge, threshold crossing timestamp and rise time, are recorded for offline analysis.

As already shown in Equation 2.6, the time resolution of a scintillator is strictly related to its scintillating properties. However, besides these, both the sample geometry and the light detector properties contribute to the achieved time performance. To understand their contribution it is useful to introduce two extra quantities:

- the **photon travel spread** (**PTS**), which both combines fluctuations related to the incoming γ-ray interaction point and the time from a photon creation to its detection;
- the **single photon time resolution** (**SPTR**), a property that measures the performance of the photodetector.

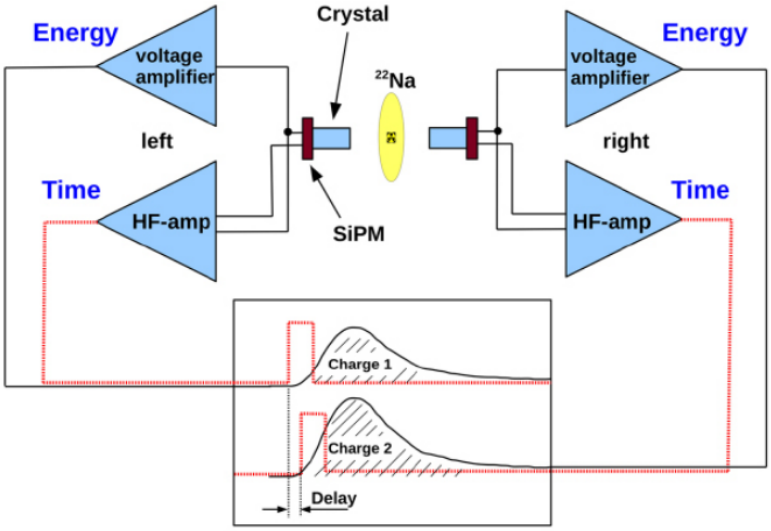

Figure 3.7: Schematic of the CTR setup measuring samples at 511 keV. From reference [46].

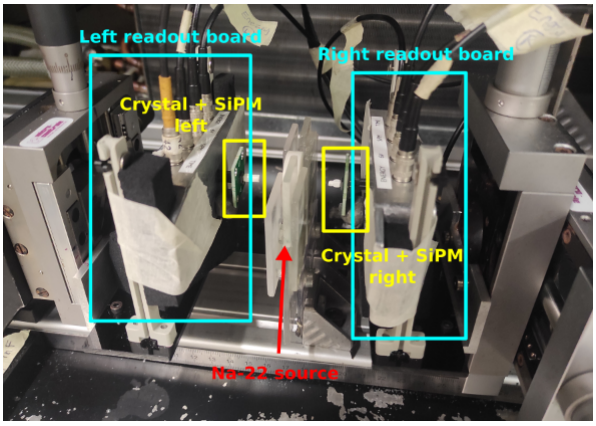

Figure 3.8: Picture of two crystals detected in coincidence in the setup measuring CTR.

Both these contributions are included in the following formula [48]:

$$\mathrm{CTR} = \sqrt{\frac{\tau_{d,\mathrm{eff}} \cdot (1.57 \cdot \tau_r + 1.13 \cdot \sigma_{\mathrm{SPTR*PTS}})}{\mathrm{PDE} \cdot \mathrm{LO}}}, \tag{3.2}$$

both deduced theoretically and proven experimentally [49]. $\sigma_{\mathrm{SPTR*PTS}}$ is a parameter obtained from the convolution of the SPTR of the detector and the PTS of the sample.

Chapter 4

Mixed BGSO and BSO Crystals

The first materials investigated in this thesis were BGO, BSO, and mixed BGSO ($Bi_4(Ge_xSi_{1-x})_3O_{12}$) crystals. The aim was to gain insights into the tunability of their scintillation and timing properties and to assess their potential as candidates for dual readout calorimetry applications.

The chapter commences by providing an overview of the advantages and limitations of BGO and BSO as inorganic scintillators and the role they had and have in the scintillators panorama. Subsequently, it delves into the two research directions pursued. The first involves a characterization campaign focused on measuring the scintillating and timing properties of BGSO samples with varying Ge fractions. The second line of research investigates the dual readout capability of a BSO sample through the use of dedicated optical filters.

4.1 BGO and BSO in the Scintillators Panorama

High-density scintillating crystals have been widely employed in calorimetry because of their excellent energy resolution when detecting electromagnetic showers [6, 7, 50]. On the other hand, their large e/h ratio does not make them suitable for accurate hadrons detection [51]. Due to recent developments in photodetector technologies [52], there has been a growing interest in these materials because of the possibility to exploit Cherenkov light in addition to scintillation light in dual readout calorimetry to improve the resolution for hadronic showers and jets [53]. Among these crystals, the possibility to discriminate Cherenkov radiation from scintillation light was effectively proven for bismuth germanate ($Bi_4Ge_3O_{12}$ or BGO), despite the huge divergence between its scintillation yield and the number of Cherenkov photons produced (about

1 % of the total) [54, 55].

Because of its high density, short radiation length and relatively high light yield, BGO was a material largely used in particle physics experiments, with the L3 electromagnetic calorimeter at LEP e^+e^- collider as an example [6]. However, as a drawback, this crystal has a large decay time ($\sim$ 300 ns) and moderate radiation tolerance limiting its application in harsh radiation environments in which fast timing and high radiation resistance are key figures of merit.

A possible alternative to BGO that is being of interest in recent years is bismuth silicate ($Bi_4Si_3O_{12}$ or BSO), a crystal that shares the same lattice structure as BGO with germanium atoms replaced with silicon ones. BSO exhibits a factor three shorter decay time ($\sim$ 100 ns) and about a factor ten better radiation hardness with respect to BGO [56, 57, 58]. Besides that, the transmission cut-off in BSO is blue-shifted compared to that of BGO allowing the exploitation of a wider wavelength range to extract Cherenkov radiation from such material. These properties combined with its low light output, yielding a much enhanced Cherenkov-scintillation light fraction with respect to BGO, make BSO a leading competitor for applications in dual readout calorimetry at future collider experiments.

A significant limitation of BSO arises from the challenge associated with growing large-sized crystals due to its near-congruent melting composition. A possible solution to overcome this issue may be the growth of mixed crystals by partial replacement of silicon with germanium in the host [59].

A characterization campaign of the scintillating and timing properties of two sets of mixed BGSO crystals ($Bi_4(Ge_xSi_{1-x})_3O_{12}$, with x varying from 0 to 1) was launched to compare the results obtained with pure BGO and BSO samples. The results obtained are published in *"Characterization of mixed $Bi_4(Ge_xSi_{1-x})_3O_{12}$ for crystal calorimetry at future colliders"* on Nuclear Instruments and Methods in Physics Research Section A [60].

4.2 Tuning Scintillation and Timing Properties: Mixed BGSO Crystals

4.2.1 Samples

Two different sets of mixed BGSO samples with percentages of germanium x ranging from 0 % to 100 % were characterized for this study. The first batch was grown with the Czochralski technique by Shonan Institute of Technology in Fujisawa (Japan) and consists of optically polished plate-shaped samples of dimension $\sim 6 \times 6 \times 0.7$ mm^3 having Ge fraction x equal to 0, 0.1, 0.3, 0.5, 0.7, 0.9 and 1 (see Figure 4.1). The second set was also grown using the Czochralski method by the Institute for Scintillation

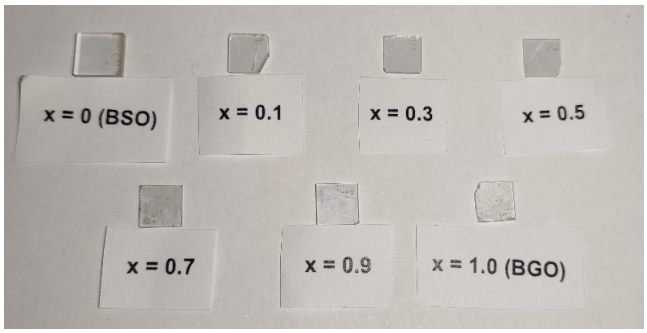

Figure 4.1: Picture of the plate-shaped BGSO samples grown with variable concentrations of Ge by Shonan Institute of Technology in Fujisawa, Japan.

Materials of NAS (Ukraine) and cut from the ingot to pixels of variable dimensions (about $5 \times 6 \times 7$ mm^3) and surface polishing state, with $x = 0$, 0.1, 0.4 and 0.9.

From each pixel sample produced by the Institute for Scintillation Materials of NAS, two $2 \times 2 \times 3$ mm^3 pixels were cut and mirror-polished for better SiPM pairing for the CTR measurements. The pure BSO bulk pixel was not cut for testing its scintillation and Cherenkov kinetics at 511 keV, as described in Section 4.3.

4.2.2 Transmission Spectra

The transmission spectra obtained for the plate-shaped samples are reported in Figure 4.2. The results indicate that the transmission at wavelengths above 500 nm is similar for all the samples with good transparency down to about 300 nm. On the other hand, the cut-off wavelength below which the sample absorbs the incident light varies with the Ge fraction x. Plotting the cut-off wavelength, defined as the wavelength at which the transmittance is 40 % of the value in the stability region, against x, an overall increase of the cut-off wavelength can be noticed moving from BSO to BGO (see Figure 4.3). The data point associated with the $x = 1$ sample is off this trend, due to its poor surface condition.

A difference in wavelength cut-off of about 13 nm was measured between pure BSO and BGO plate-shaped samples, in line with what was reported in literature [55]. Such a blue-shifted cut-off is beneficial for enlarging the wavelength range for Cherenkov photons extraction from the sample, thus enhancing their number.

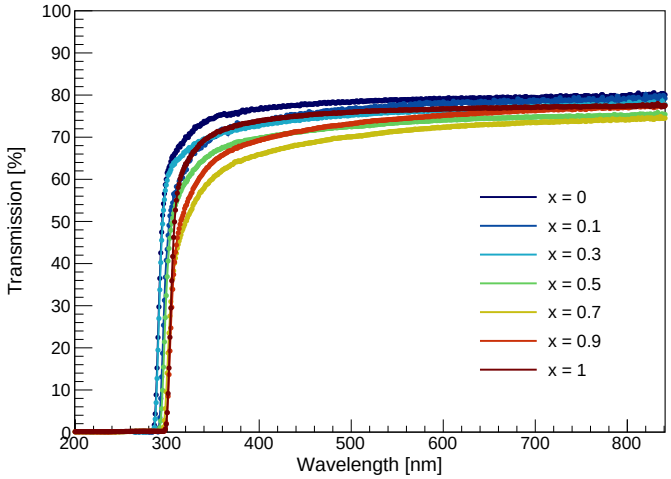

Figure 4.2: Trasmission spectra measured for the plate-shaped samples with variable Ge fraction x along their thinnest dimension. Adapted from reference [60].

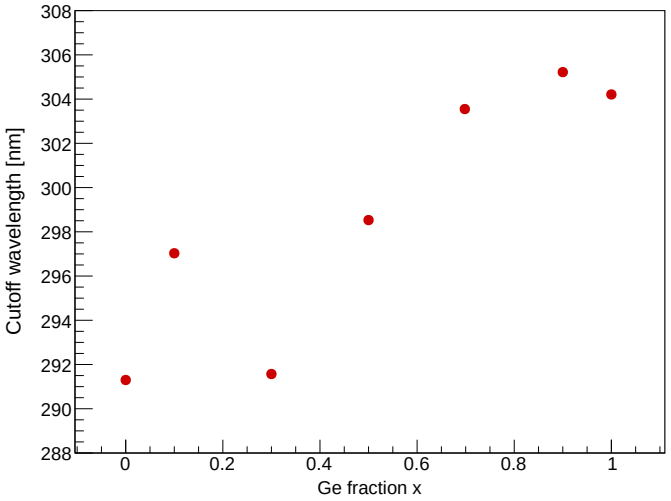

Figure 4.3: Cut-off wavelength in transmission, calculated at 40 % from the stability region, against the Ge fraction x. Adapted from reference [60].

Plate-shaped samples ($6 \times 6 \times 0.7$ mm^3)		
x	**Light output** (photons/MeV)	**Energy resolution FWHM** (%)
0	2000 ± 100	24.8 ± 0.2
0.1	2100 ± 110	25.2 ± 0.5
0.3	1900 ± 100	24.4 ± 0.3
0.5	2600 ± 130	23.5 ± 0.3
0.7	3200 ± 160	20.5 ± 0.3
0.9	7200 ± 360	13.1 ± 0.2
1	8800 ± 440	12.1 ± 0.2

Pixels ($2 \times 2 \times 3$ mm^3)		
x	**Light output** (photons/MeV)	**Energy resolution FWHM** (%)
0.1	1560 ± 80	27.4 ± 1.4
	1470 ± 70	27.9 ± 1.5
0.4	1980 ± 100	23.9 ± 0.8
	2110 ± 110	25.2 ± 0.9
0.9	3120 ± 160	19.8 ± 0.6
	3850 ± 190	22.0 ± 0.6

Table 4.1: Measured light output and energy resolution FWHM for both sets of samples.

4.2.3 Light Output and Energy Resolution

The results obtained in terms of light output and energy resolution are reported in Table 4.1 and plotted against x in Figure 4.4 and Figure 4.5. The light output does not vary significantly up to ~ 0.3 and then rapidly increases with the Ge fraction. It can be noticed that the light output measured for the $x = 0.9$ pixels is much lower with respect to the plate-shaped samples: an explanation for this is given by impurities and internal defects of the sample generated during its growth which affect its light transmission efficiency.

The light output achieved for the plate-shaped BSO sample is 22 % of the BGO one. Such result is in agreement with literature [56].

The energy resolution follows an opposite trend, being constant at low Ge fraction and decreasing at high x. A correlation plot between energy resolution FWHM and light output of the tested samples is presented in Figure 4.6 and the points were fitted

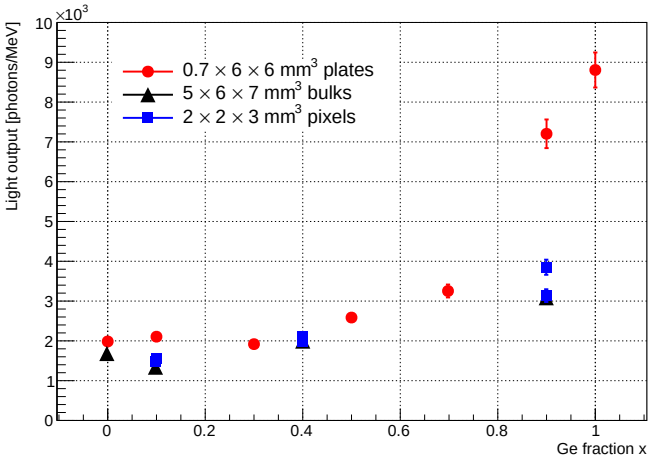

Figure 4.4: Light output of the tested samples versus their Ge fraction x. From reference [60].

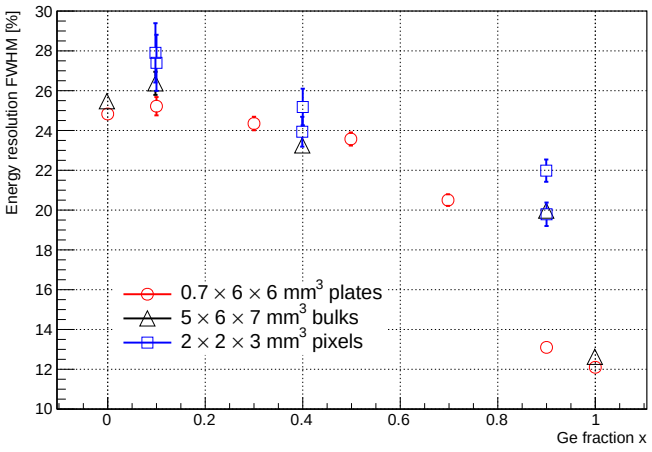

Figure 4.5: Energy resolution FWHM measured out of charge integrated spectra versus the Ge fraction x of the tested samples. From reference [60].

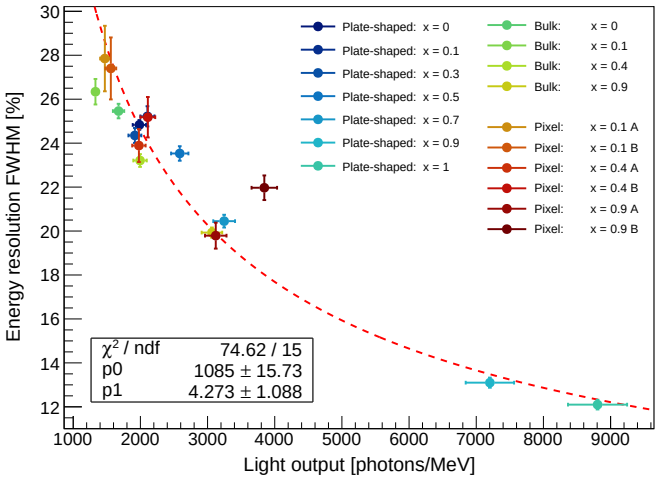

Figure 4.6: Energy resolution FWHM against light output measured for each tested sample. Adapted from reference [60].

using the following function:

$$\mathrm{ER} = \frac{a}{\sqrt{\mathrm{LO}}} \oplus b, \tag{4.1}$$

being a and b parameters of the fit related to photostatistics and intrinsic light output respectively.

4.2.4 Scintillation Kinetics under X-ray Excitation

The scintillation kinetics of the samples was measured using the X-ray TCSPC setup and employing a 500 nm (with 40 nm FWHM) bandpass filter in front of the hybrid PMT window. The emission-time profiles obtained were parametrized with the bi-exponential function of Equation 2.4 having three decay time components and convoluted with the IRF of the setup. The distribution measured for one of the $x = 0.4$ pixels is shown in Figure 4.7 by way of example.

The rise and decay time components achieved and the effective decay times calculated are reported in Table 4.2. The scintillation rise time values of the plate-shaped samples are all below the resolution of the setup ($\sim$ 25 ps).

The samples scintillation kinetics exhibits an initial accelerated part approximated by the fastest decay time components $\tau_{d,1}$ and $\tau_{d,2}$. The reason behind this relies on a locally achieved high density of elementary excitations within the ionization track

Plate-shaped samples ($6 \times 6 \times 0.7$ mm^3)							
x	τ_{d1} (ns)	R_1	τ_{d2} (ns)	R_2	τ_{d3} (ns)	R_3	$\tau_{d,eff}$ (ns)
0	2.9	1.5 %	27	9.7 %	107	88.8 %	58.6 ± 2.0
0.1	2.9	1.9 %	34	23.6 %	124	74.5 %	51.3 ± 2.1
0.3	2.4	1.5 %	24	13.1 %	101	85.5 %	49.9 ± 1.8
0.5	3.1	1.6 %	33	19.3 %	136	79.2 %	59.4 ± 2.2
0.7	3.5	1.4 %	37	15.4 %	160	83.3 %	75.1 ± 2.7
0.9	3.9	1.0 %	45	9.5 %	235	89.5 %	117.1 ± 4.1
1	2.5	0.6 %	47	8.0 %	321	91.4 %	144.5 ± 5.5

Pixels ($2 \times 2 \times 3$ mm^3)								
x	τ_r (ps)	τ_{d1} (ns)	R_1	τ_{d2} (ns)	R_2	τ_{d3} (ns)	R_3	$\tau_{d,eff}$ (ns)
0.1	91	4.7	2.8 %	42	25.1 %	114	72.1 %	54.9 ± 2.1
0.4	63	3.0	1.9 %	35	22.3 %	127	75.9 %	53.8 ± 2.2
0.9	63	5.7	1.4 %	52	11.6 %	236	87.0 %	118.3 ± 4.2

Table 4.2: Parameters of the triple exponential used to fit the data from the measurements with the TCSPC setup for all the samples tested. τ_r is the rise time, $\tau_{d,i=1,2,3}$ are the decay time components and $R_{i=1,2,3}$ their corresponding abundances. An uncertainty of 10%, 6% and 2% can be assumed on the values of τ_{d1}, τ_{d2} and τ_{d3} extracted from the distributions respectively.

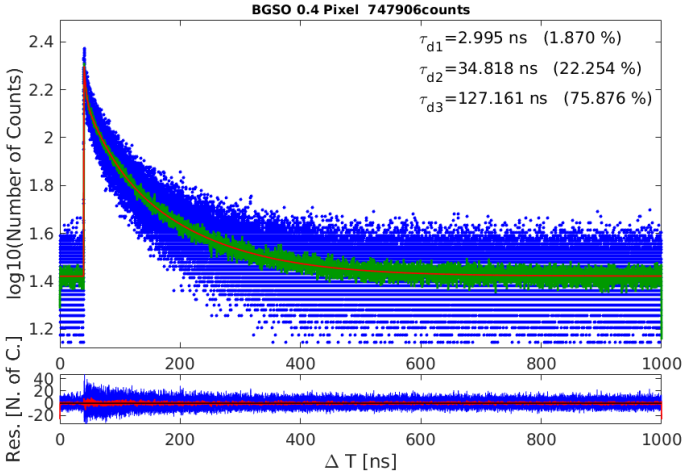

(a) Full scintillation range

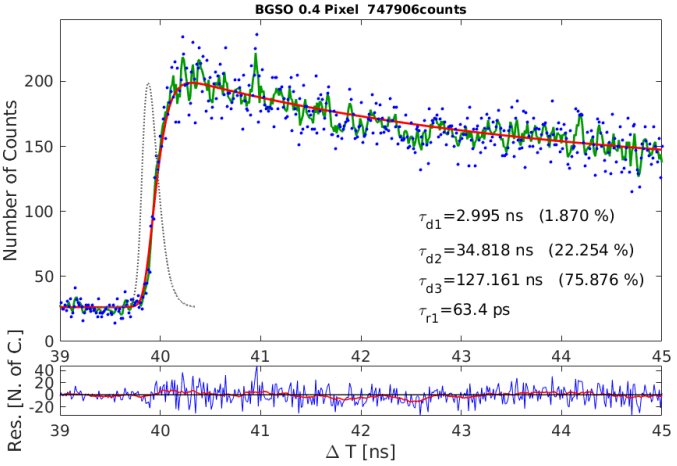

(b) Rising edge

Figure 4.7: Emission-time distribution obtained exciting a $x = 0.4$ BGSO pixel sample with X-rays. The black dotted line represents the IRF of the setup, the green line is a sliding average on a five bins window of the distribution to guide the eye, and the red solid line is the fit of the data points. From reference [60].

of the attenuated X-ray [61]. A three decay time components emission kinetics was also observed in previous studies [56, 62].

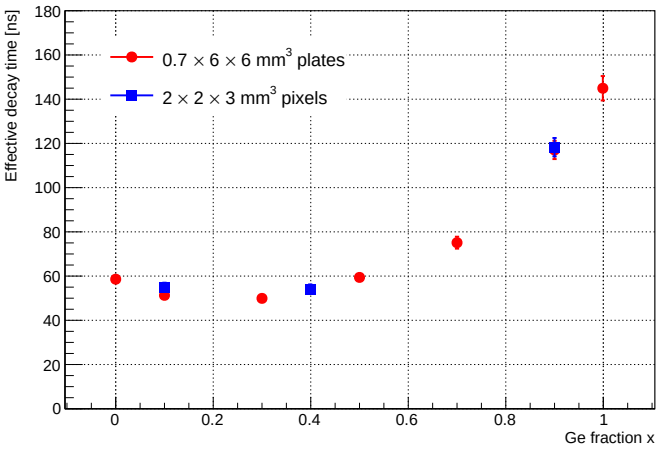

Figure 4.8: Effective decay time plotted against the Ge fraction x for both plate-shaped and pixels samples. From reference [60].

Plotting the effective decay time achieved against the Ge fraction x of the sample, an optimum of 49.9 ± 1.8 ns is reached for the $x = 0.3$ plate-shaped sample (see Figure 4.8). The samples' light output and effective decay time are linearly correlated as shown in Figure 4.9.

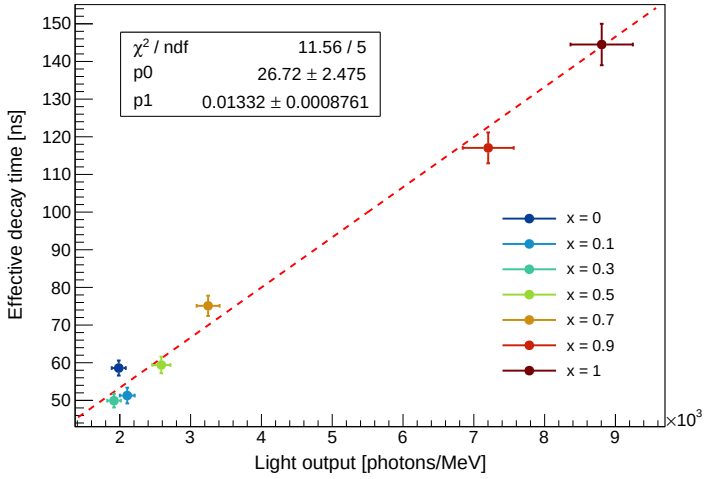

Figure 4.9: Effective decay time plotted against the light output of the plate-shaped samples. The red dotted line provides a good fit of the data points. Adapted from reference [60].

4.2.5 Coincidence Time Resolution at 511 keV

The CTR measurements were performed with the test bench described in Section 3.5.

On one hand, the plate-shaped samples were coupled with Cargille Meltmount glue to Broadcom SiPMs of 6×6 mm^2 active area and biased at 38 V and measured in coincidence against a reference $2 \times 2 \times 3$ mm^3 BGO crystal. To estimate the CTR of two identical plate-shaped samples ($\mathrm{CTR_{samp}}$), the contribution $\mathrm{CTR_{ref}}$ needs to be subtracted in quadrature from the measured value $\mathrm{CTR_{meas}}$ as follows:

$$\mathrm{CTR_{samp}} = \sqrt{2 \cdot \mathrm{CTR_{meas}^2} - \mathrm{CTR_{ref}^2}}, \tag{4.2}$$

being $\mathrm{CTR_{ref}}$ 157 ± 3 ps FWHM and 351 ± 10 ps FWTM.

On the other hand, each $2 \times 2 \times 3$ mm^3 pixel was Cargille Meltmount coupled to a 38 V powered Broadcom SiPM having 3.7×3.7 mm^2 active area and measured against an identical sample.

For the CTR evaluation, just the events with full energy deposition in both detectors were taken into account. Furthermore, a time-walk correction based on the rise time of the signal was applied in a similar way as illustrated in [63, 64]. Such a time-walk effect is related to fluctuations in the number of detected Cherenkov photons in each event. The CTR estimation is therefore extracted from time-walk corrected time

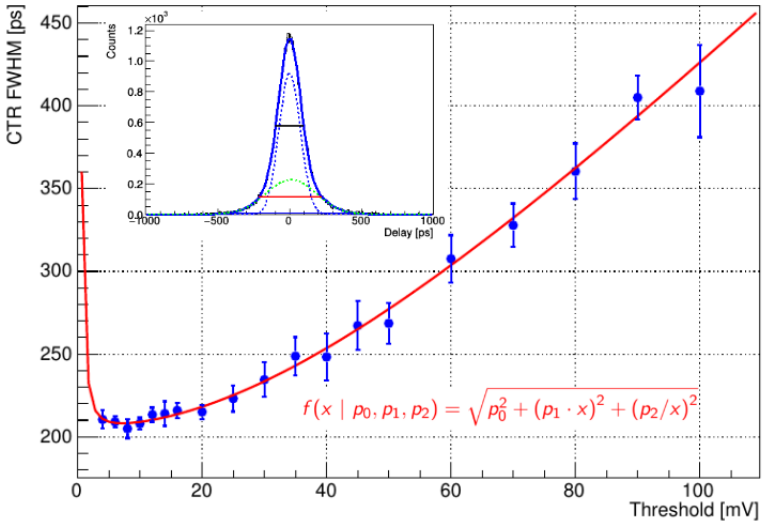

Figure 4.10: CTR FWHM plotted against the leading edge threshold set on the time signal for the $x = 0.4$ BGSO pixels. The red solid line represents the fit function. In the upper left corner of the figure, the delay distribution at a 10 mV threshold is depicted. The distribution is fitted using a double-Gaussian function, represented by the blue solid line, while its components are denoted by the blue and green dotted lines. The FWHM and FWTM of the distribution are indicated by the black and red horizontal lines, respectively. From reference [60].

delay distributions (see the inset plot in Figure 4.10). Fitting them with a double Gaussian function, both the FWHM and FWTM of the distributions were extracted.

The leading edge threshold θ set on the time signal for the timestamp extrapolation for each plate-shaped BGSO sample and each pair of BGSO pixels was varied to identify the settings proving the best time performance. Figure 4.10 shows an example of CTR FWHM plotted against the leading edge threshold set on the time branch of the signal for the $x = 0.4$ BGSO pixels pair. The trend of data points for each graph was modelled by summing in quadrature three contributions:

$$\mathrm{CTR}\,(\theta) = \sqrt{\mathrm{CTR}_0^2 + (p \cdot \theta)^2 + (n/\theta)^2}, \tag{4.3}$$

being CTR_0 a parameter intrinsic to the crystal and independant from θ, $p \cdot \theta$ a term related to photostatistics and n/θ a noise contribution term.

Both CTR FWHM and FWTM values were extracted from the fit minimum and reported in Table 4.3. Their values were also plotted against the Ge fraction of the sample under test in Figure 4.11. It can be observed that some mixed BGSO samples exhibit better timing with respect to pure BGO and BSO, with an optimum around

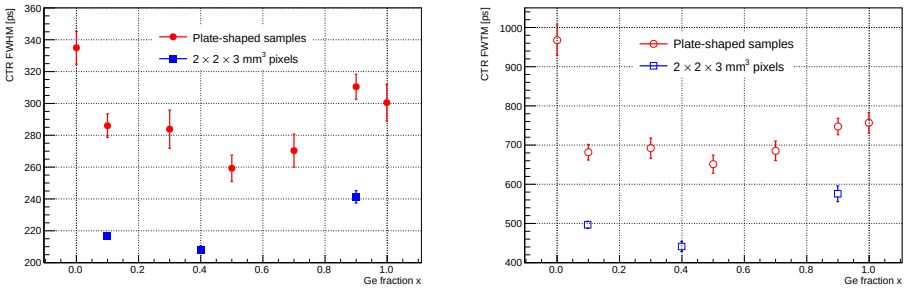

Figure 4.11: CTR FWHM (left) and FWTM (right) versus the Ge fraction x of each tested sample. From reference [60].

Plate-shaped samples ($6 \times 6 \times 0.7$ mm^3)		
x	**CTR FWHM** (ps)	**CTR FWTM** (ps)
0	335 ± 10	970 ± 39
0.1	286 ± 8	682 ± 20
0.3	284 ± 12	692 ± 26
0.5	259 ± 8	651 ± 23
0.7	270 ± 10	685 ± 25
0.9	311 ± 9	747 ± 21
1	300 ± 12	756 ± 26

Pixels ($2 \times 2 \times 3$ mm^3)		
x	**CTR FWHM** (ps)	**CTR FWTM** (ps)
0.1	217 ± 2	495 ± 9
0.4	208 ± 2	441 ± 13
0.9	244 ± 4	576 ± 20

Table 4.3: CTR FWHM and FWTM at 511 keV for both sets of samples.

$x \sim 0.5$ for both plate-shaped and pixel sets. The best-performing sample is the $x = 0.4$ pixels pair with a CTR of 208 ± 2 ps FWHM and 441 ± 13 ps FWTM.

It is important to highlight that the real timing performance of the plate-shaped samples should account for slightly different geometries and corner cracks for a more precise understanding of the behaviour of CTR varying the Ge fraction of the sample.

Specifically speaking, the BSO sample was thicker (~ 1 mm) and larger ($\sim 6 \times 7$ mm^2) with respect to the other samples. Being the BSO sample surface larger than its coupled SiPM active area (6×6 mm^2), around 16 % of the light would never be immediately detected resulting in a ~ 8 % worsening of the time resolution. Hence having a BSO crystal with the same geometry as the other samples would yield an improved CTR of 310 ± 12 ps FWHM and 898 ± 36 ps FWTM.

4.3 Study of BSO Dual-Readout Capabilities

Beyond the characterization campaign of the two sets of BGSO samples, the possibility to separate Cherenkov and scintillation emission in a BSO bulk crystal of dimension $\sim 5 \times 6 \times 7$ mm^2 has been demonstrated by exploiting optical filters.

This study was performed with the setup described in 3.4.2. Three different measurements were performed:

- placing a 500 nm bandpass filter (40 nm FWHM), called "scintillation filter" from now on, from Thorlabs between the sample and the IDQ sensor;
- placing a "Cherenkov filter" from Thorlabs transparent to light up to 400 nm and down to 670 nm between the crystal and the sensor;
- without any filter, acquiring a spectrally unresolved emission-time distribution.

The transmission spectra of the two filters employed for this study, the photon detection probability (PDP) of the SPAD and BSO scintillation and Cherenkov spectral distributions are shown in Figure 4.12. The BSO scintillation and Cherenkov spectra convoluted with the SPAD PDP are also plotted in Figure 4.13.

Knowing the scintillation emission profile $\mathrm{Em}(\lambda)$ of BSO, its Cherenkov spectrum $\mathrm{Ch}(\lambda) = a/\lambda^2$, the transmission spectrum $\mathrm{F}(\lambda)$ of the filter employed and the SPAD sensor $\mathrm{PDP}(\lambda)$, an analytical estimation of the expected ratio between Cherenkov and scintillation yield can be given by the following:

$$f = \frac{\int_{\lambda_{\min}}^{\lambda_{\max}} \mathrm{Ch}(\lambda)\ \mathrm{F}(\lambda)\ \mathrm{PDP}(\lambda)\ \mathrm{d}\lambda}{\int_{\lambda_{\min}}^{\lambda_{\max}} \mathrm{Em}(\lambda)\ \mathrm{F}(\lambda)\ \mathrm{PDP}(\lambda)\ \mathrm{d}\lambda}, \tag{4.4}$$

where $\lambda_{\min}$ and $\lambda_{\max}$ limit the wavelength range in which $\mathrm{PDP}(\lambda) \neq 0$.

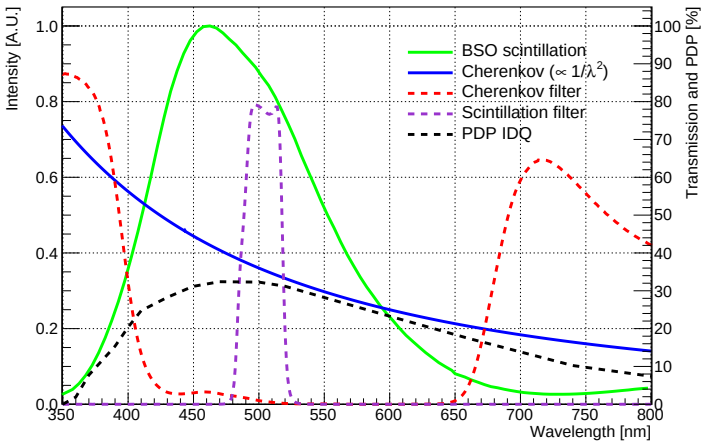

Figure 4.12: BSO scintillation and Cherenkov spectra, transmission spectra of the filters tested and photon detection probability of the ID-Quantique SPAD. From reference [60].

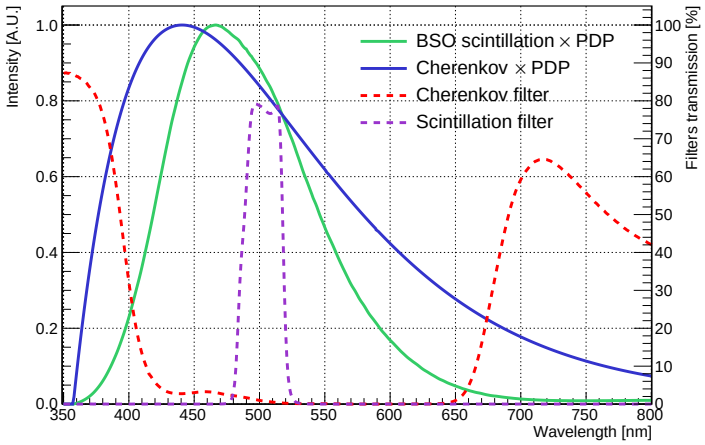

Figure 4.13: BSO scintillation and Cherenkov spectra convoluted with the PDP of the ID-Quantique SPAD and transmission spectra of the filters tested. From reference [60].

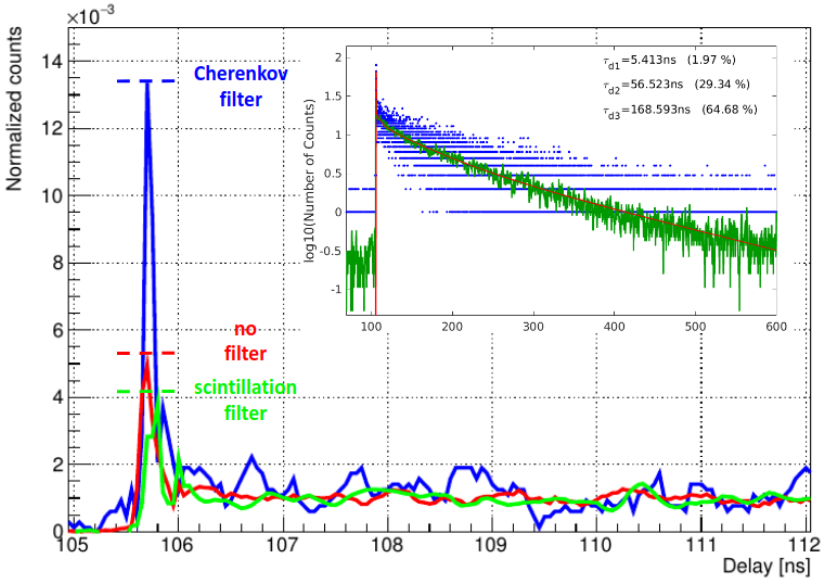

Figure 4.14: Zoomed view of the rising edge and Cherenkov part of the TCSPC measurements of the BSO sample under 511 keV irradiation. Additionally, on the upper right side of the figure, the decay region of the signal produced by the spectrally unresolved BSO measurement is shown. From reference [60].

4.3.1 Scintillation Kinetics and Cherenkov Yield at 511 keV

The rising edge of emission-time distributions accounting for both Cherenkov and scintillation contributions obtained in the three measurement conditions are displayed in Figure 4.14. All distributions were preliminarily normalized over the scintillation region with no Cherenkov influence (between 106.5 and 200 ns) after background subtraction. Depending on the measurement condition, a different Cherenkov peak high can be noticed. The scintillation filter suppresses the UV part of the Cherenkov light resulting in a lower amount of Cherenkov photons detected with respect to those produced through the scintillation mechanism, while the Cherenkov filter cuts out most of the scintillation yielding a more pronounced Cherenkov peak.

This result proves the capability to efficiently discriminate Cherenkov and scintillation light in BSO by means of dedicated optical filters. Such a separation may be achieved for instance using SiPMs with spectral responses enhancing either scintillation or Cherenkov light detection.

Under the assumption of perfect superposition of the three emission-time profiles of Figure 4.14 over their pure scintillation region, an estimate of the ratio $R = f_{\text{filter}}/f_{\text{no filter}}$ between the fraction of Cherenkov light detected in the configurations

with and without filter can be provided. The calculation of this ratio is performed after subtraction of the contribution related to scintillation from the Cherenkov peak height. The values extracted from the distributions are $R_{Cher}^{meas} = 3.1 \pm 0.6$ and $R_{scint}^{meas} = 0.7 \pm 0.1$ for the measurement with Cherenkov and scintillation filters respectively. On the other hand, the values for such ratios are analytically calculated through Equation 4.4 are $R_{Cher} = 3.19$ and $R_{scint} = 0.61$, which are in line with the experimental results.

4.4 Conclusions

The characterization campaign of the mixed BGSO samples revealed interesting features in terms of light output, scintillation kinetics and timing for possible exploitation of these materials for detector development in high-energy physics experiments. An optimum in terms of timing performances is achieved for germanium fraction between 30 % and 50 %. The best coincidence time resolution at 511 keV of 208 ± 2 ps was measured for the $x = 0.4$ BGSO $2 \times 2 \times 3$ mm^3 pixels pair, while the $x = 0.3$ BGSO plate-shaped sample exhibited the fastest scintillation kinetics, with an effective decay time of 49.9 ± 1.8 ns and a slow decay component of 101 ± 2 ns. Other samples have a lower slow decay time component with respect to pure BGO and BSO bringing benefit in pile-up rejection in harsh radiation environments. To sum up, the exploitation of mixed crystals can be an effective strategy for tuning the scintillating properties for a specific application.

Besides this study, the Cherenkov and scintillation emissions were efficiently discriminated in a BSO sample using optical filters transmitting in ad-hoc wavelength ranges.

BSO and optimized BGSO may be leading candidates for crystal-based dual readout calorimetry at future collider experiments given their faster decay time, lower light yield and better probability to efficiently detect their Cherenkov and scintillation light with respect to BGO.

Chapter 5

Cross-luminescent scintillators

Cross-luminescent emission, with its scintillation kinetics operating on a sub-nanosecond scale, stands out for its capability to generate almost-prompt photons, making it a valuable resource for precise time tagging.

The chapter provides an overview of the current state of knowledge regarding BaF_2. It then explores two distinct strategies employed to reduce the slow emission component associated with BaF_2. The first one involves the incorporation of yttrium as a dopant. A detailed characterization campaign was conducted on BaF_2 samples containing various concentrations of this dopant, and the results of this study are presented in this chapter. The second strategy entails the utilization of dedicated optical filters to selectively isolate specific wavelengths of light emitted by BaF_2. Finally, the chapter concludes by summarizing the findings of a characterization study conducted on another cross-luminescent material, $CeCaCl_3$.

5.1 Barium Fluoride State of the Art

Barium fluoride (BaF_2) was the first material in which cross-luminescence was observed. Its self-trapped exciton (STE) emission between the conduction and the valence band peaked around 320 nm and with a decay time of $\sim$ 630 ns was already known at the beginning of the '70s [65]. Its cross-luminescence emission was discovered approximately 10 years later [66]: it peaked at 220 nm and exhibited a decay time of $\sim$ 0.6 ns, thus establishing BaF_2 as the fastest inorganic scintillator of its time [32]. From a more accurate investigation of BaF_2 cross-luminescence, two main emission peaks, at 220 nm and at 195 nm, and a shoulder at $\sim$ 175 nm were observed on top of its normal scintillation emission [67].

Among the cross-luminescent materials, BaF_2 is one of the fastest and its light yield of 1 400 photons/MeV makes it also one of the brightest ones [68]. The combination of BaF_2 scintillating properties and its significantly low production cost with respect to other widely employed inorganic scintillators, e.g. lutetium-yttrium oxyorthosilicate (LYSO:Ce) or BGO, [69] make this material of large interest on a wide range of timing applications including medical imaging (e.g. TOF PET detectors) or high-luminosity particle physics [70, 71, 72, 73, 34, 49, 74, 75].

One of the crucial issues of BaF_2 in the past years was given by the challenging detection of its cross-luminescent light. Nonetheless, to meet the demand for deep-UV light detection in experiments based on liquid Xe, such as nEXO or PETALO [76, 77], recent advancements in solid-state detector research have resulted in a high sensitivity to deep-UV light detection [78, 52]. This opened the possibility to exploit BaF_2 cross-luminescence for timing applications.

A further drawback which limits the application of BaF_2 in high radiation environments is given by its slow STE emission. It compromises precise time tagging due to signals pile-up. Two possible strategies may be adopted to suppress the STE contribution, either by introducing a dopant into BaF_2 lattice [79, 80, 81, 73, 74], e.g. lanthanum, yttrium or cadmium, or exploiting dedicated optical filters to block light in the STE emission wavelength range and transmit in the deep UV. Nevertheless, suppressing part of the light production comes with the consequence of losing information, resulting in a degradation of the energy resolution due to the reduced amount of photons detected.

In the following section, both these strategies were explored and presented. On one hand, a characterization study of a BaF_2 set of samples doped with different amounts of yttrium was realized with a focus on the dopant effect on scintillation kinetics and timing. On the other hand, different emission-time profiles were acquired for an undoped BaF_2 sample selecting its emitted light via several optical filters to suppress or enhance either the cross-luminescent or the STE emission.

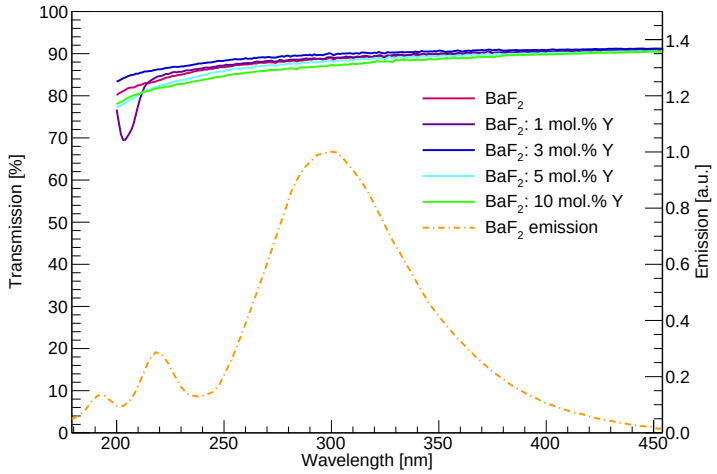

Figure 5.1: Transmission measurements of the $10 \times 10 \times 10$ mm^3 BaF_2 and BaF_2:Y samples compared to the undoped BaF_2 emission distribution taken from literature [72].

5.2 Suppressing BaF_2 STE Emission through Yttrium-doping

5.2.1 Samples

The BaF_2 samples characterized during this study were produced by the Shanghai Institute of Ceramics and had different geometries and various yttrium dopings. All samples present optically-polished surfaces and their size is either $3 \times 3 \times 3$ mm^3 or $10 \times 10 \times 10$ mm^3. Besides those, smaller $2 \times 2 \times 3$ mm^3 pixels were cut and mirror-polished at CERN out of $3 \times 3 \times 3$ mm^3 samples to allow CTR measurements with better performing SiPM of smaller active area.

The samples were doped with 1, 3, 5 or 10 mol.% yttrium and measured with undoped BaF_2 samples of the same dimensions.

5.2.2 Transmission Spectra

The transmission spectra measured for the $10 \times 10 \times 10$ mm^3 BaF_2 and BaF_2:Y samples are shown in Figure 5.1 both with the undoped BaF_2 photoluminescence spectrum taken from literature [72]. No significant difference can be noticed in varying the amount of yttrium in the sample. All samples exhibit good transparency down to $\sim$ 300 nm, and then they gradually start absorbing light. Therefore, the absorption

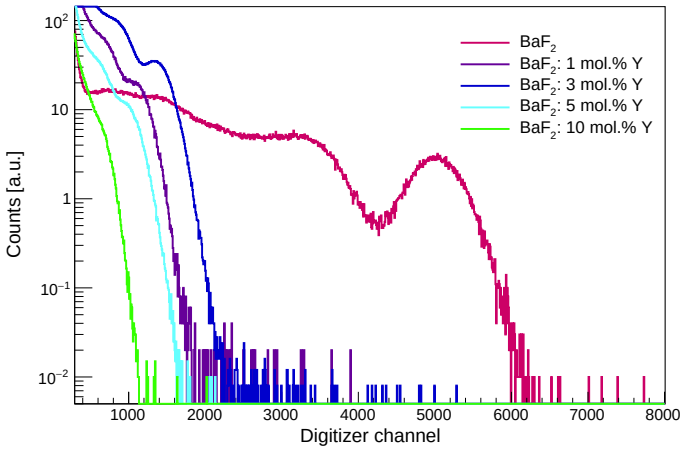

Figure 5.2: Integrated charge distributions of $3 \times 3 \times 3$ mm^3 BaF_2 and BaF_2:Y samples under 662 keV γ-ray irradiation.

region mostly affects the cross-luminescence component rather than the STE emission of the samples.

5.2.3 Light Output

The light output measurements were performed using a Hamamatsu vacuum-UV (VUV) sensitive PMT (model H6610). The $2 \times 2 \times 3$ mm^3 samples tested were dry-coupled to the PMT photocathode and wrapped in several layers of Teflon.

The light output of each sample was evaluated by comparison with a reference $2 \times 2 \times 5$ mm^3 LYSO:Ce pixel as follows:

$$\mathrm{LO}_{\mathrm{BaF_2}} = \frac{\mu_{\mathrm{BaF_2}}}{\mu_{\mathrm{LYSO}}} \cdot \frac{\langle \mathrm{QE} \rangle_{\mathrm{LYSO}}}{\langle \mathrm{QE} \rangle_{\mathrm{BaF_2}}} \cdot \mathrm{LO}_{\mathrm{LYSO}}, \tag{5.1}$$

being $\mu_{\mathrm{BaF_2}}$ and μ_{LYSO} the photopeak positions in ADC channels for the tested sample and the reference LYSO:Ce, $\langle \mathrm{QE} \rangle_{\mathrm{BaF_2}}$ and $\langle \mathrm{QE} \rangle_{\mathrm{LYSO}}$ the effective quantum efficiencies of the PMT for the tested sample and the reference and $\mathrm{LO}_{\mathrm{LYSO}}$ the light output of the reference crystal.

The integrated charge distributions obtained for all the BaF_2 samples tested are plotted in Figure 5.2. The measured values are reported in Table 5.1 and shown in Figure 5.3 as a function of the yttrium concentration.

Sample	**Light output** (ph/MeV)
BaF_2	3 700 ± 370
BaF_2: 1 mol.% Y	890 ± 90
BaF_2: 3 mol.% Y	1 100 ± 110
BaF_2: 5 mol.% Y	810 ± 80
BaF_2: 10 mol.% Y	530 ± 110

Table 5.1: Light output of $3 \times 3 \times 3\,\mathrm{mm}^3$ BaF_2 and BaF_2:Y samples.

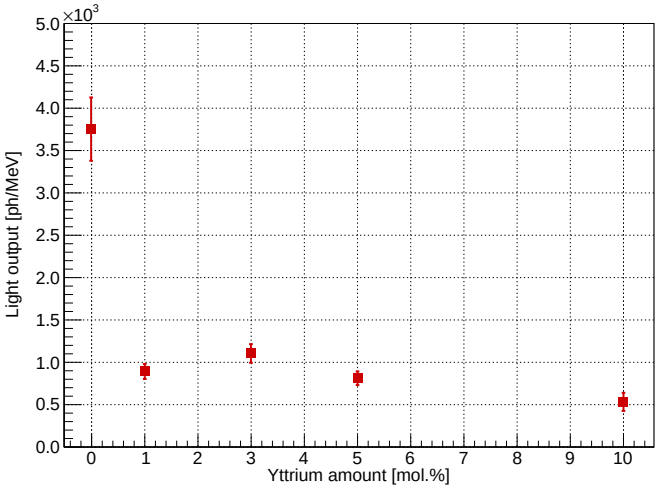

Figure 5.3: Measured light output under 662 keV γ-ray irradiation plotted against the amount of yttrium employed as a dopant for $3 \times 3 \times 3$ mm^3 BaF_2 and BaF_2:Y samples.

The outcome of these measurements demonstrated that the amount of detected photons decreases with the dopant concentration in the sample due to the yttrium effect of suppressing the STE emission. Even doping with small amounts of yttrium, e.g. 1 mol.%, generates a decrease of the light output of a factor ~ 4. The light output obtained for the undoped sample is in line with the ones measured in similar conditions with dry-coupling [34]. However, even from these measurements, a low number of photons is observed compared to BaF_2's intrinsic light yield of approximately 10 000 ph/MeV. This may be attributed to a combination of non-optimal Teflon reflectivity of UV light and self-absorption within the material.

5.2.4 Scintillation Kinetics under X-ray Irradiation

An example of emission-time distribution obtained for the BaF_2: 3 mol.% Y sample is presented in Figure 5.4. Previous studies have proved that BaF_2 cross-luminescence may be better modelled using two decay time components, one in the tens of picoseconds scale, the other between 600 and 800 ps [34, 74]. For this reason, three decay time components were used to fit the measured distribution, two accounting for the fast cross-luminescent emission and one for the slow STE component.

The values achieved for these three decay time components and their weights are reported in Table 5.2. The emission-time profiles obtained for the five samples are also superimposed in Figure 5.5 for a direct comparison. The increase in the yttrium amount has just a slightly significant impact on the decay times associated with the cross-luminescent components. On the other hand, the more yttrium is employed as a dopant, the more suppressed the STE component thus yielding a decreased decay time and its relative weight. The rise times obtained were all below the instrumental resolution.

Sample	τ_{d1} (ns)	R_1 (%)	τ_{d2} (ns)	R_2 (%)	τ_{d3} (ns)	R_3 (%)
BaF_2	0.038	0.5	0.707	5.2	643	94.4
BaF_2: 1 mol.% Y	0.030	1.4	0.698	29.8	294	68.8
BaF_2: 3 mol.% Y	0.040	1.3	0.711	27.8	318	70.1
BaF_2: 5 mol.% Y	0.027	1.4	0.689	31.8	303	66.9
BaF_2: 10 mol.% Y	0.060	5.5	0.704	51.4	145	43.1

Table 5.2: Parameters of the bi-exponential used to fit the data from the measurements with the TCSPC setup. $\tau_{d,i=1,2,3}$ are the decay time components and $R_{i=1,2,3}$ their corresponding abundances. An uncertainty of 10%, 6% and 3% can be assumed on the values of τ_{d1}, τ_{d2} and τ_{d3} extracted from the distributions respectively.

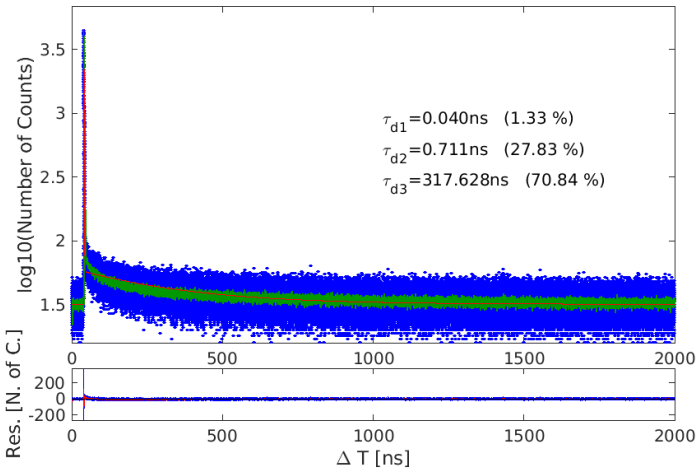

(a) Emission-time profile - STE emission

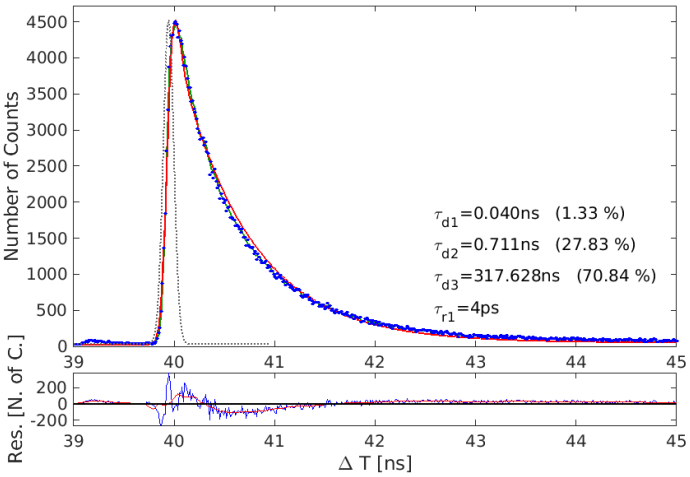

(b) Emission-time profile - Cross-luminescent component

Figure 5.4: TCSPC measurements of the BaF_2: 3 mol.% Y sample excited using a 9 keV X-ray beam. The black dotted line represents the IRF of the setup, the green line represents a sliding average of the distribution, and the red solid line is the fit of the data.

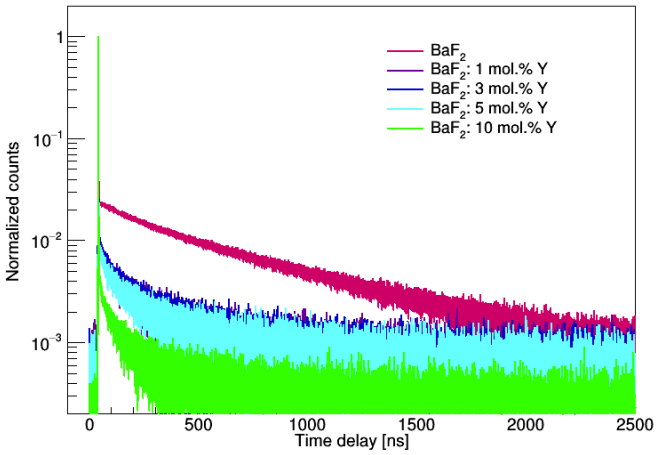

(a) Emission-time profile - STE emission

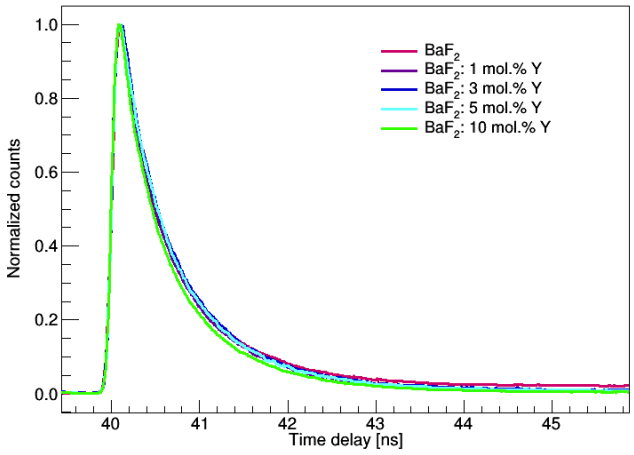

(b) Emission-time profile - Cross-luminescent component

Figure 5.5: Normalized scintillation distributions of the BaF_2 and BaF_2:Y samples excited by X-rays. (a) View of the falling part of the distributions, highlighting the slow emission of the sample. (b) Zoomed-in view of the rising edge and the cross-luminescent portion of the emission-time profiles. These plots serve to illustrate that an increase in yttrium concentration results in the suppression of the STE component, whereas the cross-luminescent part remains basically unaffected.

5.2.5 Coincidence Time Resolution at 511 keV and Vacuum-UV sensitive SiPMs

The majority of the SiPMs available on the market do not have sensitivity to vacuum UV (VUV) light. This is primarily due to the presence of a VUV light-absorbing protective layer, typically made of glass or epoxy, applied on top of the SiPM to safeguard the wire bonds and the detector itself. Additionally, there is an issue related to the mean penetration length of VUV light within the sensor: light with a wavelength of approximately 200 nm is generally absorbed within a few nanometers, causing electron-hole pairs to be generated in the uppermost part of the SiPM [52]. As a result, the photon detection efficiency of the SiPM is significantly degraded.

Vacuum ultraviolet high-density (VUV-HD) SiPMs have been specifically designed for experiments on dark matter research that utilize liquid xenon as a scintillating material. These SiPMs were developed independently by Hamamatsu Photonics K.K. (HPK) and Fondazione Bruno Kessler (FBK). Unlike other SiPMs, these devices do not feature the protective layer mentioned earlier, making them more susceptible to damage, especially when optical couplings are applied to their surface.

Devices from both producers were employed in this work. According to the datasheet, the Hamamatsu SiPMs (model S13370-6050CN) have a photon detection efficiency (PDE) of $\sim 24\,\%$ at 175 nm. However, a PDE of only $15\,\%$ at 175 nm was achieved from an independent measurement [78]. The HPK sensors have an active area of 6×6 mm^2 and single-photon avalanche diodes (SPADs) size of 50×50 μm^2. The breakdown voltage was measured to be 51.5 V.

The SiPMs produced by FBK feature an active area of 2.6×2.9 mm^2, and their square SPADs have a 35 μm pitch. According to [52], these SiPMs achieve a photon detection efficiency (PDE) of $\sim 22\,\%$ for deep UV light with a wavelength of 175 nm, and a PDE of up to $\sim 60\,\%$ can be reached at 410 nm. The measured breakdown voltage for these devices is approximately 33 V.

The CTR measurements of the BaF_2 and BaF_2:Y samples were realized against a reference $2 \times 2 \times 3$ mm^3 LSO:Ce, $0.4\,\%$ Ca pixel wrapped with several layers of Teflon and coupled using Cargille Meltmount glue to an FBK NUV-HD SiPM of 3×3 mm^2 active area. Both $2 \times 2 \times 3$ mm^3 and $3 \times 3 \times 3$ mm^3 BaF_2 and BaF_2:Y pixels were tested by coupling them with FBK and HPK VUV SiPMs, respectively. All BaF_2 and BaF_2:Y samples were wrapped with multiple layers of Teflon and dry-coupled to the photodetector. The measurements were conducted with the samples in a standing position to prevent them from falling off the SiPM. In the case of the $2 \times 2 \times 3$ mm^3, the face coupled to the sensor was one of the 2×2 mm^2 surfaces. The FBK SiPMs were powered at 39 V ($\sim$ 6 V overvoltage), while the Hamamatsu ones were biased at 61 V ($\sim$ 9.5 V overvoltage).

By considering events where the 511 keV γ-rays fully deposited their energy in both

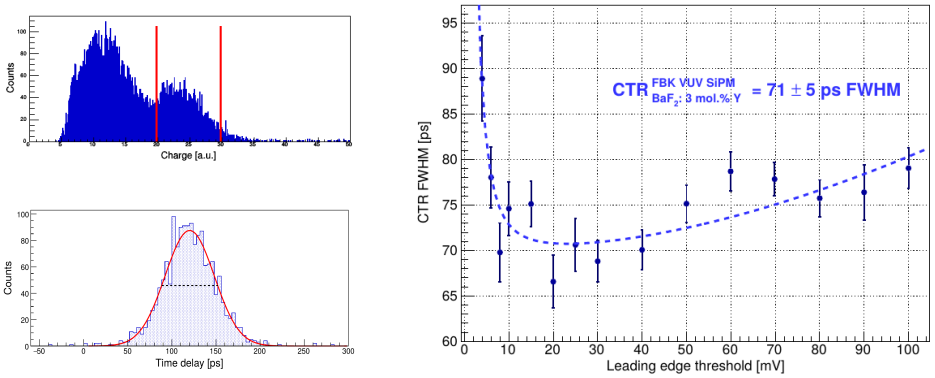

Figure 5.6: Left: charge and time delay distributions for a $2 \times 2 \times 3$ mm^3 3 mol. % Y-doped sample read out by an FBK SiPM, setting a 20 mV threshold on its time signal. Right: CTR FWHM plotted against the leading edge threshold set on the time signal for a $2 \times 2 \times 3$ mm^3 3 mol. % Y-doped BaF_2 sample coupled to an FBK device.

detectors, the CTR of each sample was determined based on the FWHM of the Gaussian function used to model the time delay distribution. To identify the optimal settings, a leading edge threshold scan was conducted on the time signal for each sample. Figure 5.6 shows an example of this scan for the 3 mol. % Y-doped sample measured with an FBK SiPM, and the CTR values were obtained from the fit minimum. The CTR FWHM values for BaF_2 and BaF_2:Y samples coupled to HPK and FBK VUV SiPMs were then plotted against the amount of yttrium used for doping the sample, as shown in Figure 5.7 and summarized in Table 5.3.

No significant difference is observed among samples with different concentrations of

Sample	**CTR FWHM at 511 keV** (ps)	
SiPM	*FBK*	*HPK*
BaF_2	71 ± 5	117 ± 5
BaF_2: 1 mol.% Y	81 ± 5	121 ± 5
BaF_2: 3 mol.% Y	71 ± 5	106 ± 5
BaF_2: 5 mol.% Y	82 ± 6	107 ± 5
BaF_2: 10 mol.% Y	76 ± 5	119 ± 5

Table 5.3: CTR FWHM at 511 keV of the BaF_2 and BaF_2:Y samples measured both with FBK and HPK SiPMs.

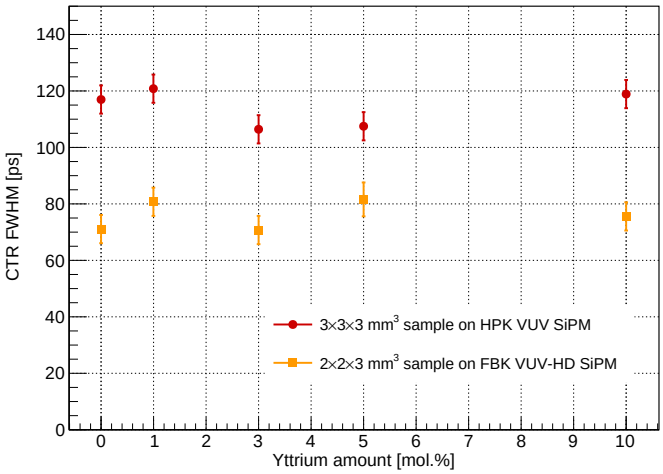

Figure 5.7: CTR FWHM plotted against the amount of yttrium used as dopant for the two sets of pixels and SiPMs tested in this study.

yttrium when coupled to SiPMs from the same manufacturer. This indicates that the time resolution in both BaF_2 and BaF_2:Y is solely influenced by the cross-luminescent component, with the STE emission playing no role. The crystals coupled to the FBK devices exhibited a CTR of approximately 75 ps FWHM, while a value of around 110 ps was achieved using the HPK SiPMs. Notably, the time performance obtained with the FBK VUV-HD SiPMs is in agreement with the results observed in [74].

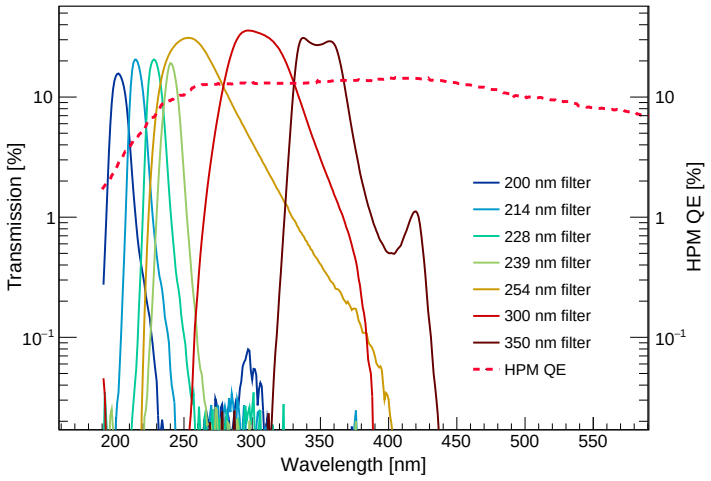

Figure 5.8: Filters transmission spectra and hybrid PMT quantum efficiency.

5.3 Optical Filters for BaF_2 Cross-luminescent Light Selection

5.3.1 Optical Filters and Measurement Conditions

The scintillation kinetics of an undoped $3 \times 3 \times 3$ mm^3 BaF_2 sample was also investigated under X-ray excitation with the setup described in Section 3.4.1, acquiring time delay distributions for different emission wavelength regions by exploiting seven UV transparent optical filters in front of the hybrid PMT photocathode. The filters, bought by Edmund Optics, underwent transparency range measurements using the transmission setup described in Section 3.1 (see the spectra in Figure 5.8).

The sample and the hybrid PMT were not moved throughout the measurement campaign. Both data acquisition times and the number of events collected were recorded for offline analysis.

5.3.2 Emission-Time Delay Distributions

The emission-time profiles acquired underwent a rescaling both in terms of acquisition times and fraction of light detected by the hybrid PMT through a factor

$$f_d = \int_{\lambda_{\min}}^{\lambda_{\max}} (\mathrm{T} \otimes \mathrm{QE})(\lambda) d\lambda, \tag{5.2}$$

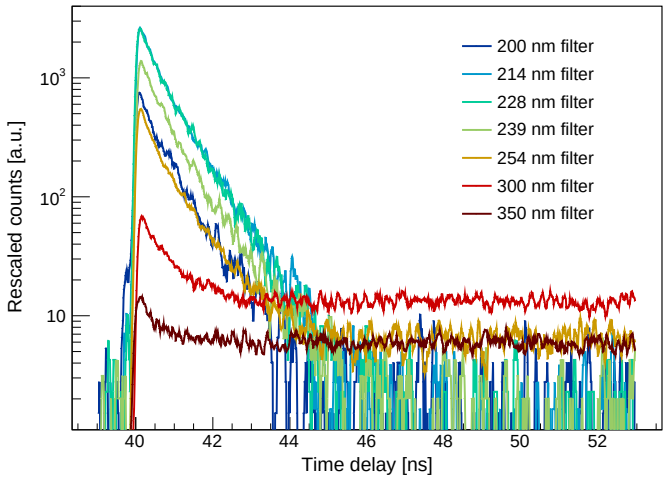

Figure 5.9: Time-rescaled scintillation emission distributions of an undoped BaF_2 sample obtained employing different optical filters in front of the hybrid PMT window.

where $T(\lambda)$ is the filter transmission, $QE(\lambda)$ the hybrid PMT quantum efficiency and λ_{min} and λ_{max} define the range over which the filter exhibits transparency. Figure 5.9 shows the rescaled profiles after background subtraction. On one hand, the distributions obtained employing the 254 nm, 300 nm and 350 nm filters show a dominant slow emission contribution and a low cross-luminescent component. On the other hand, a much larger contribution from cross-luminescence is observed, with partial or total suppression of the STE emission component, for the distributions obtained by measuring with filters with transparency centers less than or equal to 239 nm.

5.3.3 Relative Light Output Estimation

Based on the measured distribution of the undoped BaF_2 sample with no optical filter, a bi-exponential function with three components was employed in a similar fashion as illustrated for the BaF_2 samples doped with various concentrations of yttrium. The decay time components obtained from the fit are $\tau_{d1} = 0.039 \pm 0.004$ ns, $\tau_{d2} = 0.702 \pm 0.020$ ns, and $\tau_{d3} = 748 \pm 20$ ns.

Subsequently, the same fit was applied to the profiles measured with each filter, while keeping the decay time constants τ_{d1}, τ_{d2} and τ_{d3} fixed to the values obtained from the measurement without filter and with only their relative abundances being allowed to freely vary in the fit.

The abundances R of the three decay components were plotted against the mean wave-

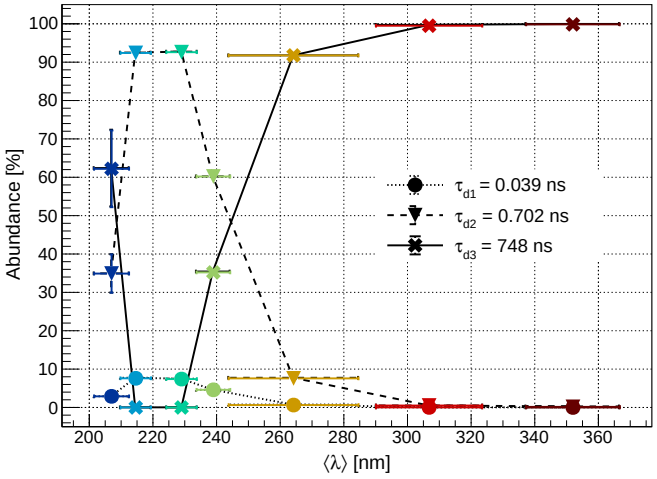

Figure 5.10: Abundances of the three decay time components versus the mean wavelength $\langle\lambda\rangle$ transmitted by the filter employed.

length transmitted by each filter, as depicted in Figure 5.10, and reported in Table 5.4. To estimate the relative light output of BaF_2 at different emission wavelengths, the integral associated with each delay distribution was evaluated and rescaled by time and the fraction of photons detected. By combining the information from the distribution integral with the abundances of the three decay components, an estimation of the relative light output for each decay time component was obtained for each distribution obtained with a UV transparent optical filter, as illustrated in Figure 5.11. The relative light output values were rescaled for the integral over the entire delay distribution obtained for the 300 nm centered filter. The data points in this plot replicate the emission spectra associated with the three components of BaF_2, and their superposition aligns with the typical photoluminescence emission distribution of BaF_2 outlined in Figure 5.1.

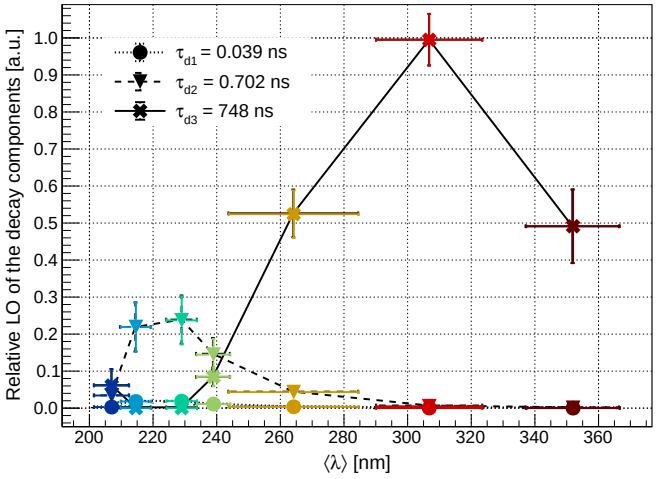

Figure 5.11: Relative light output associated with each decay time component plotted against the mean wavelength $\langle\lambda\rangle$ transmitted by the filter employed.

Filter	$\mathbf{R}(\tau_{d1} = 0.039\,\text{ns})$	$\mathbf{R}(\tau_{d2} = 0.702\,\text{ns})$	$\mathbf{R}(\tau_{d3} = 748\,\text{ns})$
200 nm	$2.9 \pm 0.2\,\%$	$34.9 \pm 0.2\,\%$	$62.2 \pm 0.4\,\%$
214 nm	$7.6 \pm 0.4\,\%$	$92.4 \pm 0.4\,\%$	$0.0 \pm 0.4\,\%$
228 nm	$7.4 \pm 0.4\,\%$	$92.6 \pm 0.4\,\%$	$0.0 \pm 0.4\,\%$
239 nm	$4.6 \pm 0.3\,\%$	$60.2 \pm 0.3\,\%$	$35.2 \pm 0.3\,\%$
254 nm	$0.63 \pm 0.04\,\%$	$7.6 \pm 0.1\,\%$	$91.8 \pm 0.1\,\%$
300 nm	$0.02 \pm 0.1\,\%$	$0.5 \pm 0.1\,\%$	$99.5 \pm 0.1\,\%$
350 nm	$0.0 \pm 0.2\,\%$	$0.1 \pm 0.2\,\%$	$99.9 \pm 0.2\,\%$

Table 5.4: Abundances of the three decay time components extracted from the bi-exponential fit of the data from the measurements of the emission kinetics of a BaF_2 sample applying different filters in front of the hybrid PMT photocathode.

5.4 Cesium-based cross-luminescent materials development: $CsCaCl_3$

Following the discovery of cross-luminescence in BaF_2 in 1982, extensive research was conducted on a wide range of cross-luminescent scintillators. However, despite these efforts, no material surpassing the performance of BaF_2 has been found, and the investigation into cross-luminescent scintillators has gradually diminished. As

of now, BaF_2 remains the sole commercially available cross-luminescent scintillator. However, as already illustrated in the past sections, its fast cross-luminescent emission in the deep UV does not match with the commonly used alkali metal-based PMTs and SiPMs. Research advancements in the field of detectors led to the development of PMTs and SiPMs capable to detect VUV light but only with low PDEs.

Numerical modelling conducted on cesium-based ternary chlorides demonstrated their UV-positioned cross-luminescent emission [82, 83], as previously reported in experimental studies [84, 85, 86, 87], exhibiting better compatibility with the spectral sensitivity of both PMTs' alkali metal-based photocathodes and commercially available SiPMs. In principle, cesium-based cross-luminescent may generate an ultra-fast signal with sufficient light output, making them suitable for fast timing applications.

Among the cesium-based ternary chlorides, $CsCaCl_3$ is one of the most promising candidates due to its fast scintillation kinetics lacking slow components and its light yield similar to that reached by cross-luminescence in BaF_2 ($\sim$ 1 400 photons/MeV). The limiting factors of this material are given by its low density (2.95 g/cm^3, compared to the 4.89 g/cm^3 of BaF_2) and Z_{eff} (42 versus 51 of BaF_2) yielding to a low stopping power for high-energy photons.

A systematic study of $CsCaCl_3$ sample scintillating and timing properties was performed to better understand its potentialities as a timing detector. The results of this characterization campaign are published in *"Ultraviolet cross-luminescence in ternary chlorides of alkali and alkaline-earth metals"* on Optical Materials: X [88].

5.4.1 Sample and its Growing Process

The $CsCaCl_3$ ingot was grown in the Institute of Physics and the Czech Academy of Sciences (FZU) in Prague by single-zone vertical Bridgman method exploiting a micro-pulling-down apparatus and starting from commercially available cesium chloride and calcium chloride. While the as-grown crystal appeared opaque due to the low quality of its surface, the bulk remained clear and transparent (see Figure 5.12). Subsequently, the samples were cut and polished from the as-grown ingot in FZU institute, transforming them into transparent 1.5 mm thick plates for optical evaluation and into $2 \times 2 \times 3$ mm^3 pixels for timing measurements.

5.4.2 Radioluminescence

Radioluminescence spectra were acquired at room temperature in the spectral range of 190–800 nm using a custom-made spectrofluorometer 5000 M, Horiba Jobin Yvon. The excitation source employed was a tungsten-cathode X-ray tube Seifert, operated at 40 kV and 15 mA. Further details of the setup are given in [88].

The radioluminescence spectrum of the $CsCaCl_3$ sample, depicted in Figure 5.13, exhibits two main emission maxima around 260 nm and 300 nm. This observation

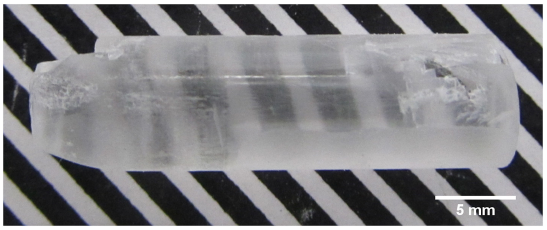

Figure 5.12: $CsCaCl_3$ ingot grown with vertical Bridgman mathod. From reference [88].

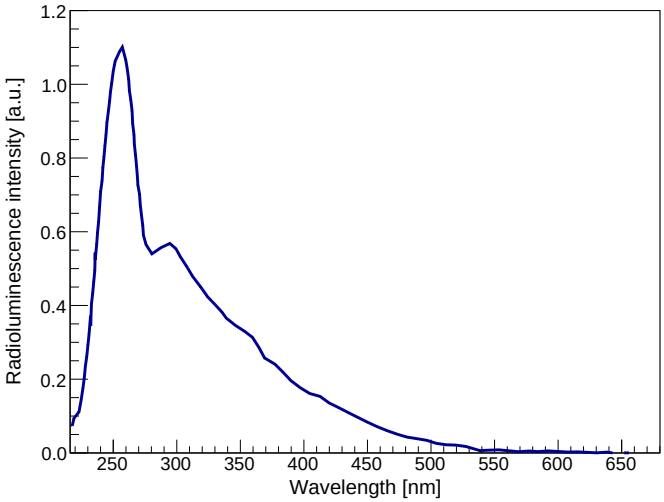

Figure 5.13: Radioluminescence spectrum of $CsCaCl_3$. Extrapolated from reference [88].

confirms the presumption that cross-luminescence in $CsCaCl_3$ from the radiative recombination between the hole in the outermost core band mainly composed of 5p states of Cs^+ and the valence band mostly consisting of 3p states of Cl^-. This presumption is further supported by the results of band structure calculations [82, 89] and the peak positions are in line with the values reported in literature [84, 32, 89]. $CsCaCl_3$ also shows a long tail at longer wavelengths originated by exciton or defect-related emission.

5.4.3 Scintillation Kinetics under X-ray Irradiation

The scintillation kinetics of the sample was measured using the usual setup described in detail in Section 3.4.1. The spectrally unresolved scintillation kinetics was modelled using two decay time components. Figure 5.14 shows the emission-time distributions measured and the fit applied: the decay time constants obtained are 151 ps and 2.2 ns with weights of 6.5 % and 93.5 % respectively. The rise time value can not be resolved from this measurement since it is below the resolution of the setup.

To further investigate the scintillation kinetics of $CsCaCl_3$, the measurement was also repeated placing a 254 nm and a 300 nm optical bandpass filter (with 40 nm FWHM) in front of the hybrid PMT window (see Figure 5.15). The scintillation pulse obtained employing the 254 nm centred filter is well-described by a single exponential decay of 2.2 ns, a value in agreement with the slowest component of the spectrally unresolved measurement. On the other hand, as for the distribution obtained using the 300 nm centred filter, the emission kinetics can be modelled through two decay time components with values compatible with those obtained for the spectrally unresolved measurement ($\tau_{d,1}$ = 266 ps (8.4 %) and $\tau_{d,2}$ = 2.1 ns (91.6 %)).

The dominant 2.2 ns component can be attributed to cross-luminescence in $CsCaCl_3$, while the $\sim$ 200 ps component to a heavily quenched excitonic or defect-related emission.

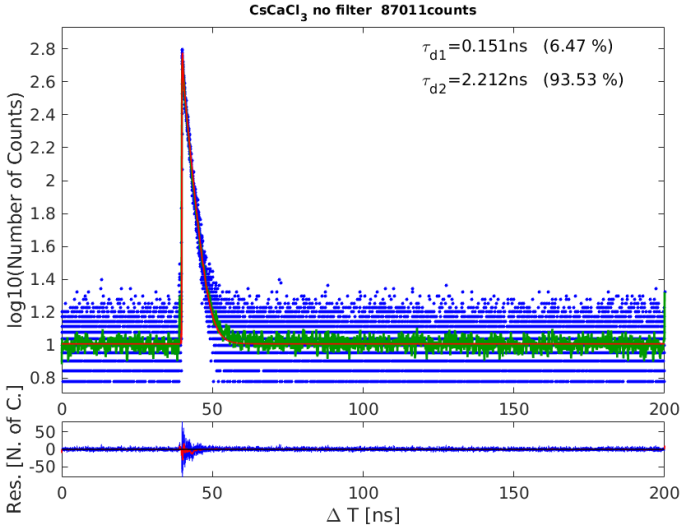

(a) Full scintillation range

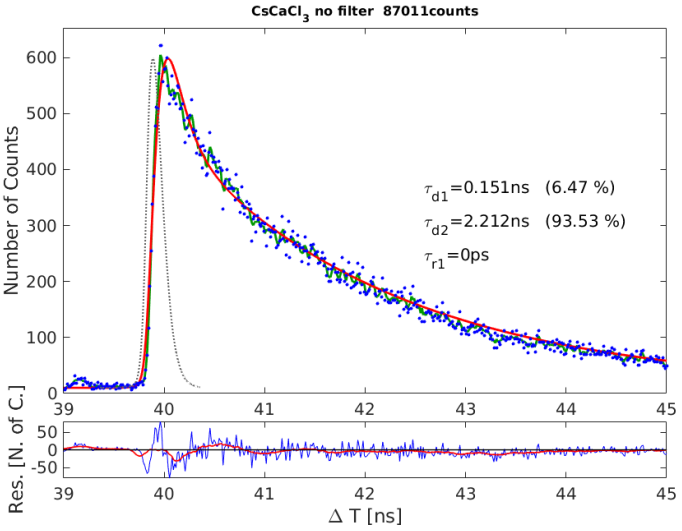

(b) Rising edge

Figure 5.14: Spectrally unresolved TCSPC measurement of a $CsCaCl_3$ sample excited using a 9 keV X-ray beam. The black dotted line is the IRF of the setup, the green line represents a sliding average of the distribution, and the red line is the fit of the data. From reference [88].

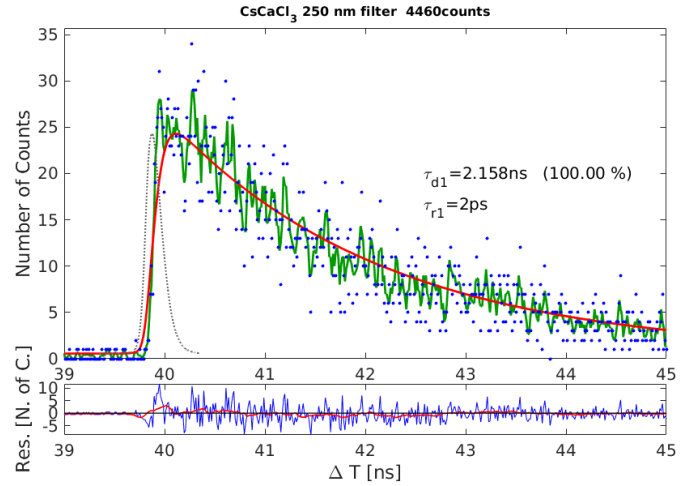

(a) 254 nm bandpass filter

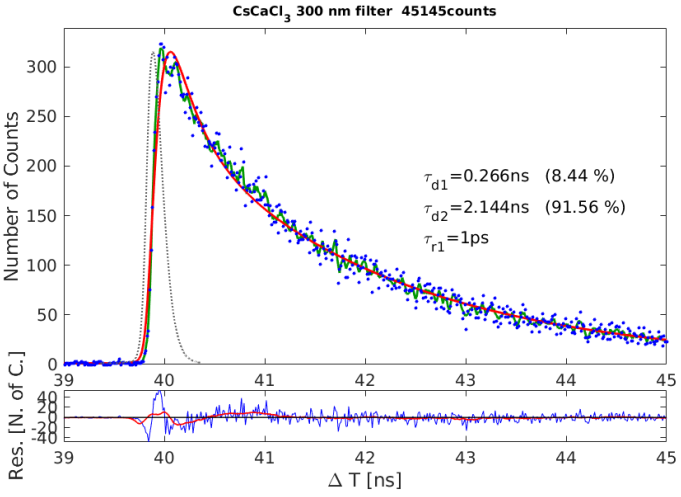

(b) 300 nm bandpass filter

Figure 5.15: Rising edge of the scintillation-time distributions of $CsCaCl_3$ measured under X-ray excitation applying a) 254 nm and b) 300 nm bandpass filters in front of the hybrid PMT photocathode. The black dotted line represents the IRF of the setup, the green line is a sliding average of the distribution, and the red line is the fit of the data. From reference [88].

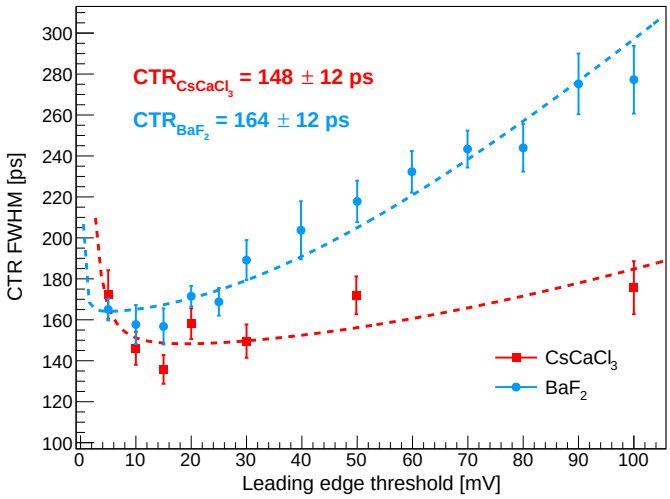

Figure 5.16: CTR FWHM plotted against the leading edge threshold set on the time signal for both $CsCaCl_3$ and BaF_2 samples. The data points are fitted using Equation 4.3.

5.4.4 Coincidence Time Resolution at 511 keV

The CTR of a $2 \times 2 \times 3$ mm^3 $CsCaCl_3$ pixel was measured against a $2 \times 2 \times 3$ mm^3 LSO:Ce, 0.4 % Ca sample coupled with Cargille Meltmount glue to a 4×4 mm^2 FBK NUV-HD SiPM. The sample under test was wrapped in several layers of Teflon and coupled in standing position to a Hamamatsu VUV SiPM (model S13370-3075CN, 3×3 mm^2 active area). Because of the hygroscopic nature of $CsCaCl_3$, Fluka Immersion oil was employed for crystal-SiPM coupling to protect the sample from air moisture. Unfortunately, the coupling oil absorbs light with wavelengths below ~ 280 nm, thus yielding a significant scintillation light loss harvested to the SiPM.

In a similar way as described for the characterization of the yttrium-doped BaF_2 samples, a leading edge threshold scan was performed on the time signal to identify the optimal setting of the measurement (see Figure 5.16). The measured CTR so obtained was 148 ± 12 ps FWHM, while BaF_2 measured under the same conditions of optical coupling and SiPM yielded a CTR of 164 ± 12 ps. It is worth noting that the emission of BaF_2, being deeper in the UV, is more affected by the coupling agent. Based on the scintillation properties of $CsCaCl_3$ and the preliminary CTR achieved, the timing performance should be comparable to that of BaF_2. With improved conditions of optical coupling and SiPM (resulting in better photon detection efficiency), a CTR close to 50 ps may be achieved, as demonstrated in BaF_2 [74].

5.5 Conclusions and Outlook

The study realized on BaF_2 and BaF_2:Y samples confirmed the possibility of efficiently suppressing the contribution of the STE slow component by either exploiting dedicated VUV-transparent optical filters or increasing the dopant concentration in the crystal lattice. From a systematic measurement campaign of the timing performance of BaF_2 samples doped with yttrium amounts ranging from 0 to 10 mol. %, no significant variation in CTR was noticed with values of $\sim$ 75 ps FWHM when the samples are dry-coupled to FBK VUV-HD SiPMs and of $\sim$ 110 ps FWHM when an HPK device is employed. Therefore, the employment of BaF_2:Y leads to a decrease in the contribution of the slow component, resulting in the mitigation of pile-up effects in high-radiation environments while maintaining the same time performance as achieved by the undoped BaF_2 .

A study of the potentialities of BaF_2 and BaF_2:Y as MIP timing detectors will be presented in Chapters 7 and 8.

To meet the requirements of fast timing applications with high photo-detection efficiency, a good spectral match between the scintillator and photodetector is essential. Cesium-based ternary chlorides have the potential to provide a red-shift ($\sim$ 1.5 eV) of cross-luminescence towards the sensitive region of the photodetector (PMT or SiPM), while simultaneously maintaining light output and timing characteristics comparable to BaF_2. Among the materials investigated $CsCaCl_3$ has emerged as the most promising candidate, with a decay time of $\sim$ 2.2 ns and a light output close to 1 400 photons/MeV. These results proved the promising potential of developing cross-luminescent scintillators with properties comparable to BaF_2 , while also achieving a better spectral match with the photodetector.

Chapter 6

Hybrid Organic-Inorganic Perovskite Scintillators

The final category of materials explored in this PhD thesis comprises perovskite scintillators, which are of particular interest due to their easily tunable properties and great timing characteristics.

The chapter provides an overview of the current state of the art concerning these materials and directs attention to the specific materials investigated in this study. It proceeds to outline the results of a characterization campaign conducted on both undoped and lithium-doped PEA_2PbBr_4 samples. Finally, the timing performance achieved by other hybrid organic-inorganic perovskite crystals is assessed and presented.

6.1 State of the Art

Over the past century, metal halide perovskite materials have been extensively studied for their magnetic, optical and electronic properties. Nonetheless, it is in the last decades that these materials, particularly those based on germanium, tin and lead, have experienced an explosion of interest [90].

One of the main reasons for this surge in interest is the unique semiconductor characteristics exhibited by metal halide perovskites. These materials possess electronic structures that offer direct tunable bandgaps, efficient light absorption, relatively balanced and small effective masses for electrons and holes, and remarkable resistance to defects, with dominant defects causing minimal non-radiative recombination [91].

Another intriguing aspect is the extraordinary flexibility to tailor the structural, optical, and electronic properties of these materials independently and synergistically. This flexibility arises from the combination of organic and inorganic components in hybrid members of the metal halide perovskite family.

Metal halide perovskites represent the state of the art as solar cells material [92]. Specifically, three-dimensional halide perovskites, or ABX_3 compounds being A small organic or inorganic cation, B a metal cation (e.g. Pb^{2+}, Sn^{2+}, Ge^{2+}) and X a halogen (e.g. I^-, Br^-, Cl^-), represent the leading material for photovoltaic applications capturing the attention of the global scientific community since 2012.

Besides this field, during the last decades metal halide perovskites revealed great scintillating and timing properties yielding active research for their application in X-ray and γ-ray detection for medicine, homeland security and particle physics. Among the materials investigated, hybrid organic-inorganic halide perovskite (HOIP) scintillators have initially received relatively less attention due to their low stability and quality [93, 94]. However, these solution-based scintillators hold great potential as they could be produced at a fraction of the cost with respect to traditional furnace-grown scintillators. Recent advances in the research of high-efficiency HOIP solar cells have also led to increased interest in the development of HOIP scintillators [95, 96].

Notably, during the 2010s' there have been significant improvements in the quality and performance of HOIP scintillators through variations of compounds and better material preparation techniques [97, 98]. Two-dimensional (2D) HOIP scintillators, in particular, have shown higher light yield compared to their three-dimensional counterparts, also exhibiting larger Stokes shifts helping to prevent self-absorption and enhancing the overall performance [97]. The layered structures of 2D HOIP crystals introduce quantum confinement effects resulting in large binding energies, typically several hundreds of meV, which favour excitonic recombination over luminescence quenching [97]. Recently developed 2D HOIP scintillators demonstrated promising characteristics, including light yield exceding 20 000 photons/MeV, energy resolutions below 10 % and scintillation kinetics with decay time components below 15 ns [99, 100].

A characterization campaign of two kinds of a PEA_2PbBr_4 scintillator was realized and the effect of lithium-doping on its scintillating and timing performance was investigated. The results of this study led to a joint publication with the Łukasiewicz Research Network-PORT Polish Center for Technology Development in Wrocław (Poland) and the CINTRA UMI laboratory in Singapore: *"Sub-100-picosecond time resolution from undoped and Li-doped two-dimensional perovskite scintillators"* on Applied Physics Letters [101]. The timing performance of other promising 2D and 3D HOIP scintillators was also measured, yielding to other joint publications within the Crystal Clear Collaboration framework [102, 103].

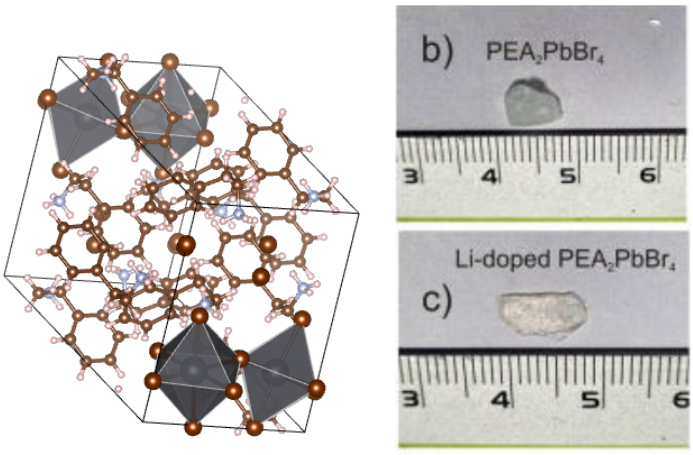

(a) (b)

Figure 6.1: Crystallographic structure of PEA_2PbBr_4 and pictures of two PEA_2PbBr_4 and lithium-doped PEA_2PbBr_4 samples. From reference [101].

6.2 Undoped and Lithium-doped PEA_2PbBr_4 Crystals

6.2.1 Crystallographic Structure and Samples

The structure of phenethylammonium lead bromide ($(C_6H_5(CH_2)_2NH_3)_2PbBr_4$ or PEA_2PbBr_4) consists of inorganic $[PbBr_6]^{4-}$-octahedra sheets separated by a layer of organic ammonium cations, as shown in Figure 6.1. The alternating layers in the crystal structure effectively confine the exciton within the inorganic layer, leading to enhanced scintillation performance, particularly in response to high-energy radiation such as γ-rays [104].

The samples characterized during this study have irregular shape and surface condition, with sizes around $5 \times 5 \times 2$ mm^3. The reason behind their not-perfect geometry relies on the non-easily controllable solution-based fabrication method which also limits the growth of large size samples [104].

The photoluminescence spectra of the two samples are reported in Figure 6.2. Both samples exhibit two emission peaks at $\sim$ 410 and $\sim$ 435 nm, indicating the presence of dual bandgaps arising from differences between surface and bulk states [99, 100]. In the photoluminescence spectra of the lithium-doped sample, a lower emission peak is observed at 410 nm in comparison to the undoped crystal. This phenomenon is attributed to self-absorption and becomes more pronounced when the crystal is

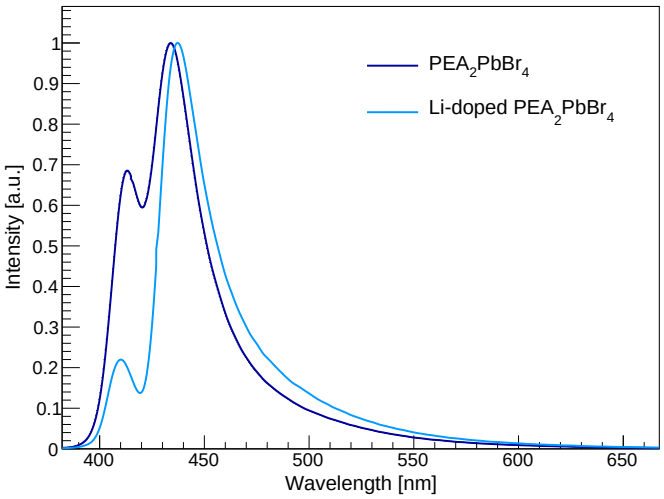

Figure 6.2: Photoluminescnce spectra of the PEA_2PbBr_4 and lithium-doped PEA_2PbBr_4 samples. From reference [101].

excited by X-rays.

Stability and hygroscopic tests were conducted on these materials, and the results revealed that their photoluminescence intensity only decreased by $\sim 10\,\%$ after one week [100]. This indicates that the crystals exhibit good stability and are relatively resistant to air moisture absorption over the tested period.

6.2.2 Light Output

The light output of the samples was measured using the Hamamatsu R2509 PMT and ^{137}Cs as excitation source. The samples were wrapped in Teflon and coupled to the PMT photocathode through a thin layer of Rhodorsil optical grease. The integrated charge spectra are shown in Figure 6.3. Both samples exhibit two peaks: the right one is the photopeak at 662 keV, while the left one is the escape peak from the K-shell absorption edge of lead [100].

The light output and energy resolution values obtained are reported in Table 6.1. The introduction of Li-doping in PEA_2PbBr_4 resulted in a significant increase in light yield, achieving a boost of $\sim 24\,\%$, and an improvement in energy resolution of about $31\,\%$. These improvements are consistent with previous reports which also demonstrated similar enhancements in light yield and energy resolution with Li-doped PEA_2PbBr_4 crystals [100].

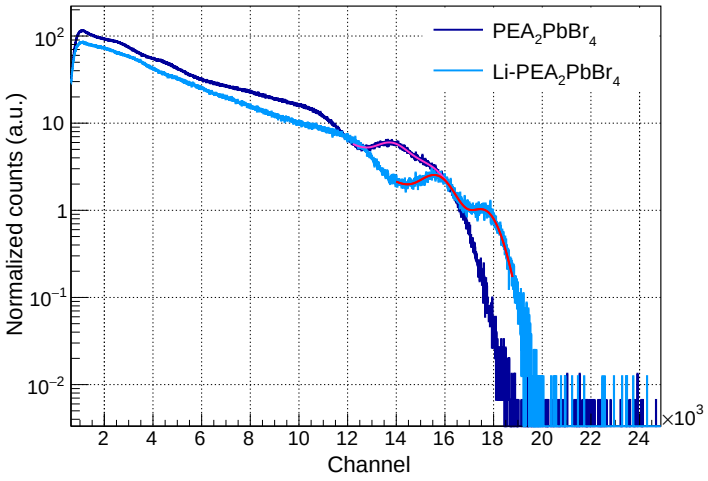

Figure 6.3: Integrated charge distribution obtained for the 2D HOIP samples tested under 662 keV γ-rays excitation. From reference [101].

Sample	**Light output** (photons/MeV)	**Energy resolution** **FWHM** (%)
PEA_2PbBr_4	17 300 ± 1 730	11.5 ± 1.2
Li-doped PEA_2PbBr_4	21 400 ± 2 140	8.0 ± 0.8

Table 6.1: Light output and energy resolution of the 2D HOIP samples measured.

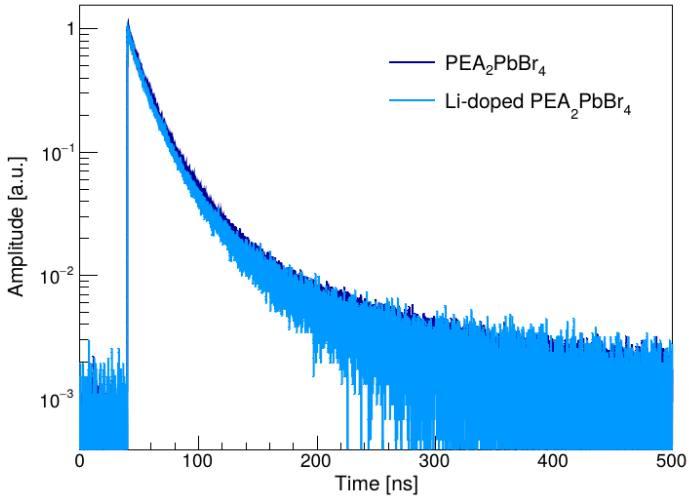

Figure 6.4: Emission-time distributions of the PEA_2PbBr_4 and lithium-doped PEA_2PbBr_4 samples under X-ray excitation.

6.2.3 Scintillation Kinetics under X-ray Excitation

The emission-time distributions of the two samples were measured by applying a bandpass filter centered at 450 nm (40 nm FWHM) in front of the hybrid PMT photocathode to suppress potential air excitation contributions. Their superposition is reported in Figure 6.4.

Since a (semi-)prompt scintillation component was observed, the scintillation pulse was modelled as a sum of three bi-exponential functions and a Dirac-delta function in a similar way used to model the signal coming from Cherenkov photons [42]. The decay time components and the fraction of prompt signal G resulting from the fit are reported in Table 6.2, while their rise time components were not precisely determined since they are below the resolution of the setup. A faster scintillation kinetics was observed for the lithium-doped sample, with an effective decay time of 14.7 ± 0.8 ns with respect to the 16.1 ± 0.9 ns achieved for the undoped PEA_2PbBr_4 sample and comparable G fraction.

Sample	τ_{d1} [R_1] (ns)	τ_{d2} [R_2] (ns)	τ_{d3} [R_3] (ns)	G (%)	$\tau_{\mathrm{d,eff}}$ (ns)
PEA_2PbBr_4	2.4 (2.3 %)	15.5 (62 %)	83.8 (20 %)	13 ± 2	16.1 ± 0.9
Li-doped PEA_2PbBr_4	2.3 (2.5 %)	13.7 (59 %)	68.0 (23 %)	14 ± 2	14.7 ± 0.8

Table 6.2: Fit results of the scintillation kinetics meeasurements for PEA_2PbBr_4 and Li-doped PEA_2PbBr_4. G is the weight of the Dirac-delta function used to model the ultra-fast component, τ_{d1}, τ_{d2} and τ_{d3} are the exponential decay components and R_1, R_2 and R_3 their respective weights. $\tau_{\mathrm{d,eff}}$ is the effective decay time. An uncertainty of 5% can be assumed on the values of τ_{d1}, τ_{d2} and τ_{d3} extracted from the distributions respectively.

6.2.4 Coincidence Time Resolution at 511 keV

In order to evaluate the time performance of these materials at 511 keV, a CTR measurement of both samples was realized in coincidence with a reference $2 \times 2 \times 3$ mm^3 LSO:Ce, 0.4 % Ca reference detector glued with Cargille Meltmount to an FBK NUV-HD SiPM of 3×3 mm^2 active area. Each sample was wrapped in several layers of Teflon and Meltmount-coupled to a Hamamatsu SiPM (model S13360-3050PE, 3×3 mm^2 active area, 50×50 μm^2 spad size) biased at 61 V (about 10 V overvoltage).

Similarly as discussed already for the BGSO and BaF_2:Y samples, a selection on the photopeak events was performed in both reference and detector under test. Therefore the CTR was obtained as the FWHM of the time delay distributions obtained for the full-energy deposition events. In order to evaluate the CTR of two identical samples, the contribution related to the reference detector needs to be subtracted in quadrature according to Equation 4.2.

A leading edge threshold scan on the time branch was performed to identify the settings providing the best time resolution (see Figure 6.5). The CTR values extracted from the fit minimum are 100 ± 4 ps and 84 ± 5 ps FWHM for the undoped and lithium-doped PEA_2PbBr_4 samples respectively. Due to their short decay times and high light outputs, both samples exhibited a pretty impressive time performance considering the non-optimal geometry of the sample if compared, for instance, with the 75 ps FWHM achieved for a $2 \times 2 \times 3$ mm^3 LSO:Ce,Ca pixel in similar conditions [49].

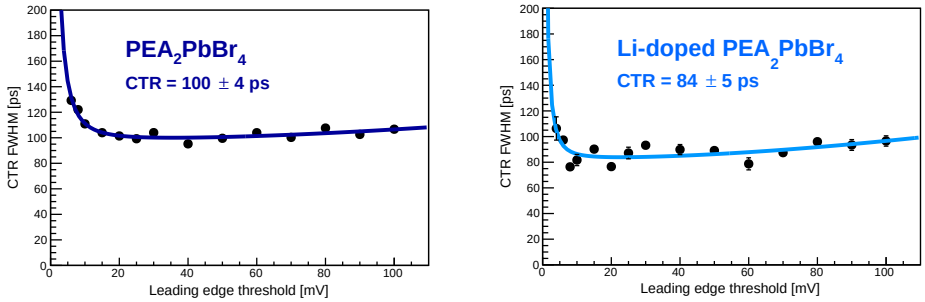

Figure 6.5: CTR FWHM plotted against the leading edge threshold set on the time signal for the two HOIP samples tested. The data points are fitted using Equation 4.3. Adapted from reference [101].

6.3 Other $A_2B_{n-1}Pb_nX_{3n+1}$ (n = 1,2) HOIP Scintillators

From the different measurements campaigns performed, PEA_2PbBr_4 stands out as one of the best scintillators among the various 2D HOIPs, showcasing excellent attributes such as high light yield and decay time in the few nanoseconds scale. Nonetheless, its sensitivity to X- and γ-rays is constrained due to its relatively low mass density and effective atomic number.

For such a reason, it may be of interest to investigate other HOIP scintillators with higher density and stopping power, for instance, obtained by exchanging the halide from bromide to iodide or modifying the cation from PEA to BA. A full characterization campaign of the scintillating and timing properties of some HOIP scintillators synthesised in Łukasiewicz Research Network-PORT Polish Center for Technology Development in Wrocław (Poland) was conducted through a joint collaboration among many institutes in the frame of the Crystal Clear Collaboration. The results obtained are published in *"PEA_2PbI_4: fast two-dimensional lead iodide perovskite scintillator with green and red emission"* in Materials Today Chemistry [102] and in *"$A_2B_{n-1}Pb_nX_{3n+1}$ (A = BA, PEA; B = MA; n = 1, 2): Engineering Quantum-Well Crystals for High Mass Density and Fast Scintillators"* in the Journal of Physical Chemistry [103].

The timing performance at 511 keV of some promising samples was measured with the setup illustrated in Section 3.5. The samples investigated include BA_2PbBr_4, PEA_2PbI_4, BA_2PbI_4 and $PEA_2MAPb_2I_7$.

Sample	**Density** (g/cm^3)	**Light output** (photons/MeV)	**CTR FWHM** (ps)
PEA_2PbBr_4	2.4	17 300	100 ± 4 [a]
Li-doped PEA_2PbBr_4	2.4	21 400	84 ± 5 [a]
BA_2PbBr_4	2.4	40 000	81 ± 6 [a]
PEA_2PbI_4	2.6	1 000	138 ± 10 [b]
BA_2PbI_4	2.7	2 000	149 ± 10 [b]
$PEA_2MAPb_2I_7$	3.0	1 400	207 ± 14 [b]

Table 6.3: Density, light output and CTR FWHM (obtained either with Meltmount- [a] or dry-coupling [b]) of some of the samples tested. All densities and the light output values of BA_2PbBr_4, PEA_2PbI_4, BA_2PbI_4 and $PEA_2MAPb_2I_7$ are from [103].

6.3.1 Coincidence Time Resolution at 511 keV

The samples tested were measured in similar conditions against a LSO:Ce, 0.4 % Ca reference detector as the undoped and lithium-doped PEA_2PBBr_4 samples. The samples had irregular shapes ($\sim 3 \times 3 \times 1$ mm^3) and roughly-polished surface conditions. The only major difference is that the PEA_2PbI_4, BA_2PbI_4 and $PEA_2MAPb_2I_7$ samples were dry-coupled to their SiPM due to the hygroscopic nature of these materials, thus affecting the light collection and the overall time performance. On the other hand, the BA_2PbBr_4 sample was coupled to a 3×3 mm^2 HPK SiPM via Cargille Meltmount.

Even for this measurement campaign, a leading edge threshold scan was performed for each sample, as shown in Figure 6.6. The results obtained extracting the fit minimum are reported in Table 6.3 along with both density and light output at room temperature of each material.

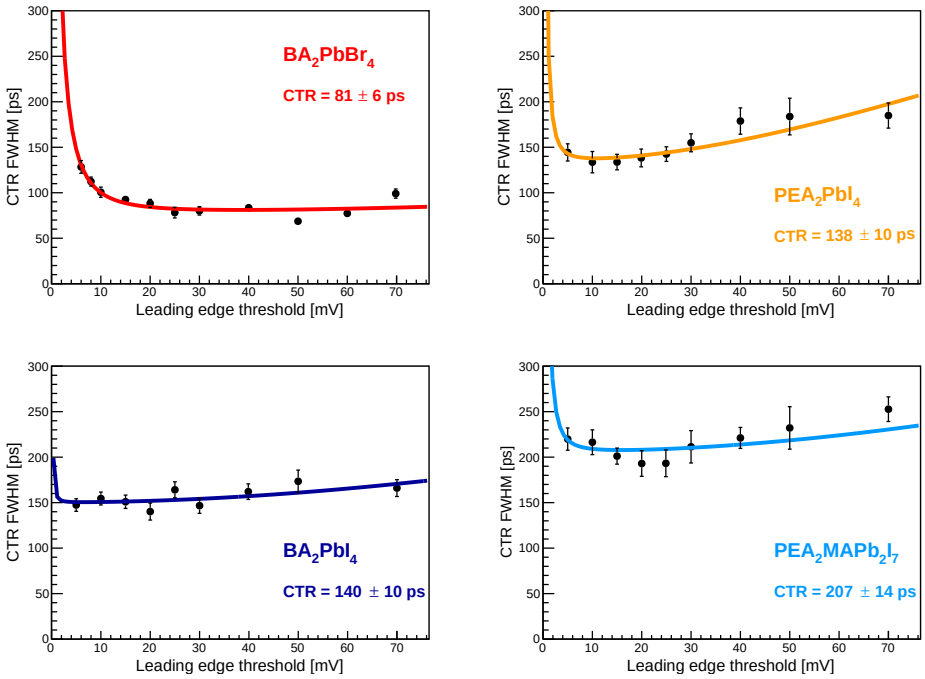

Figure 6.6: CTR FWHM plotted against the leading edge threshold set on the time signal for the HOIP samples tested. The data points are fitted using Equation 4.3. The plot for PEA_2PbI_4 is adapted from [102], while those for BA_2PbI_4 and $PEA_2MAPb_2I_7$ are adapted from [103].

6.4 Conclusions

These studies revealed scintillation and timing properties of these HOIP materials competitive with other organic and inorganic scintillators, but with manufacturing costs tens of times lower. For instance, the light output achieved by the PEA_2PbBr_4 and lithium-doped PEA_2PbBr_4 demonstrated good competitiveness with other commonly used scintillators, e.g. LYSO:Ce, BGO and $LaBr_3$:Ce, and fast emission kinetics with respect to most of the inorganic scintillators. Some of these materials also exhibited quite impressive time performance below 100 ps considering the bad surface state of the samples and the non-optimal measurement conditions.

The major drawback of these materials is given by their low mass density and effective atomic number thus increasing the absorption length for X-rays, γ-photons and high-energy particles. Nonetheless, these HOIP crystals may be either combined with dense materials, e.g. BGO or LYSO:Ce, in heterostructured scintillators for TOF-PET applications [104] or exploited as charged particles time tagging detectors in front of a calorimeter.

Part III

Materials Investigation for MIPs Timing Detectors

Chapter 7

Simulation Studies for MIPs Timing Detectors

As already illustrated in Chapter 1, precise time tagging of charged particles will be of crucial importance to mitigate vertex merging in the high pile-up environments expected in future high-energy physics experiments. It is clear that various technologies are more suited for distinct environments. Among them, the combination of scintillating material and SiPM represents a viable option as timing detectors to cover large areas with relatively contained costs. Among the materials investigated in the past, LYSO:Ce demonstrated to be a material of great interest due to its good timing, scintillating and radiation resistance properties. For these reasons, LYSO:Ce was the crystal chosen for building the CMS Barrel timing detector [23].

Given the growing interest from various research groups in fast scintillating materials for a wide range of applications, exploring the potential of alternative materials and ultra-fast light emission processes, such as Cherenkov emission, hot intraband luminescence and cross-luminescence, holds significant promise for precise timing detection in high-luminosity experiments. In order to test novel concepts and investigate parameters typically beyond experimental measurements, key tools are offered by Monte Carlo simulations.

For this purpose, a Monte Carlo simulation framework based on the GEANT4 toolkit [105] was developed to investigate the timing properties of charged particle detectors. This framework was built upon a previous one, originally designed in the frame of the collaboration between the University of Milano-Bicocca and CERN groups, primarily focused on the study of pixellated crystal matrices for PET.

The software reproduces various key aspects of the detection chain. It starts with modelling the energy deposition of high-energy charged particles within pixel crystals, then simulates the generation and propagation of Cherenkov and scintillation light. Finally, it mimics the response of photodetectors to extract a timestamp for each event.

The chapter preliminary provides an overview of the framework setup, covering its essential steps. It begins with the primary beam generation, then proceeds to illustrate the interaction of the incident beam with the material and describe optical photons generation and propagation, concluding with the evaluation of event timestamps from the obtained digitized pulse. Subsequently, the performance of several selected materials is explored and the findings from the software are presented and discussed.

7.1 Simulation Setup: Geometry, Radiation-Matter Interaction, Light Generation and Propagation

The software simply reproduces a crystal with flexible geometry made of several materials of interest. It also replicates a detector of arbitrary size coupled to one of the crystal faces.

The simulation framework allows to generate one or more energetic charged particle to investigate their interaction output with the simulated material. The radiation-matter interaction was regulated through the default physics list QGSP_BERT. The interaction of the incoming particle with the detector is simulated by GEANT4 and results in the creation of energy deposits in specific 3D coordinates. This energy deposit map, along with other data such as the initial momentum coordinates and the generation position of the incident particles, is stored in ROOT files and available for further analysis.

In addition to energy deposits, particles interacting with the detector produce Cherenkov photons, while the energy deposits are converted into scintillation photons. This step is performed according to the scintillation parameters given in input for the crystal material, including emission spectrum, light yield, rise and decay times of its scintillation components. The travel of these photons in the medium is carried out using GEANT4 ray-tracing library: ray-tracing is a method that models the propagation of optical photons by representing them as rays travelling in discrete steps according to geometric optics principles. In addition to light transport phenomena, ray-tracing accurately models the effects brought by surface imperfections [106]. The interaction between photons and optical surfaces is reproduced through the UNIFIED model [107]. It characterizes the interaction of an

optical photon with rough surfaces by dividing it into micro facets oriented according to a user-defined distribution centered around the direction of a perfectly polished surface. Each generated photon propagates within the active material and may reach the surface coupled to the detector: if it undergoes refraction on that surface, its propagation is halted and its main features, e.g. its timestamp, wavelength, production and stopping positions, are recorded.

7.2 Analog Pulse Production and Timestamp Extraction

The following step realized by the framework is the simulation of the photodetector pulse originating from the optical photons stopped in it. In order to properly reproduce the response of a SiPM, the information obtained from the previous part of the software was merged with some specifics of the sensor given in input, as illustrated in the following.

- At first, the SiPM quantum efficiency is employed to selectively filter out photons based on their wavelength.
- To create a digitalized pulse, an array of zero voltages with sampling and length set by the user is produced. Electronic noise may be introduced by adding a random voltage value to each sample, following a Gaussian distribution with a user-defined standard deviation.
- To account for the transit time spread of the SiPM for each detected photon, a Gaussian time smearing is applied to the timestamps acquired.
- Subsequently, the individual photoelectron pulse is parametrized photon by photon as

$$A(t) = A_0 \left(e^{-t/\tau_d} - e^{-t/\tau_r} \right), \tag{7.1}$$

  being A_0 randomly distributed according to a narrow Gaussian distribution. The single pulses are then summed to digitalize the waveform of the event.

  In this simplified model, the detector is assumed to be linear and with an infinite dynamic range. This is a fair assumption for the purpose of the framework as only the very first photons contribute to the timestamp determination. Therefore, in such operational range, the response of a SiPM is linear with a good approximation.

Starting from the digitalized pulse the timestamp of the event is extracted setting a threshold defined by the user for leading edge discrimination.

7.3 Simulated Materials and SiPMs

As mentioned above, this simulation framework was developed and employed to have a clear understanding of the potentiality of interesting materials as timing detectors for energetic charged particles. The simulations performed tried to reflect as accurately as possible the measurement conditions of the testbeam activities described in detail in the following chapter.

The simulated primary particle beam was composed of 150 GeV π^+. Nonetheless, when the particle reaches relativistic speeds, its energy parameter becomes less crucial because its energy deposition through medium ionization exhibits almost negligible dependence on it. The pion beam was directed parallel to the crystal's axis, targeting the face opposite to the photodetector.

The crystals simulated include common dense inorganic scintillators known to have fast scintillation kinetics, i.e. LYSO:Ce, LSO:Ce,Ca and GAGG:Ce (specifically GFAG from C&A, as aluminium garnet crystals exhibit producer-dependant scintillation and timing properties [108]). The timing properties of these materials have already been investigated in past studies [109, 110] and led to the choice of LYSO:Ce as the material for the CMS Barrel MIP timing detector. A further light-production process of great interest may be Cherenkov emission, as its light is promptly generated with the passage of the particle through the medium. For this reason, two common materials exploiting Cherenkov light for timing applications were investigated: BGO and $PbWO_4$. Finally, cross-luminescence, known to be a sub-nanosecond emission phenomenon, was taken into account and BaF_2 was added to the list of simulated materials.

A preliminary length scan of LYSO:Ce crystal of dimension $2 \times 2 \times L$ mm^3 was performed, while $2 \times 2 \times 10$ mm^3 was the crystal standard size varying the material simulated. Their surface condition was modelled to accurately replicate that of a commercial-available polished bulk crystal. The faces not coupled to the SiPM were covered with a reflector to enhance light collection towards the SiPM. Furthermore, a thin layer mimicking Meltmount glue (or Viscasil 100M grease for BaF_2) was placed between the crystal and the detector.

For all crystals with the exception of BaF_2, the silicon detector modelled was a Hamamatsu Photonics S13360-3050PE device, which has a 3×3 mm^2 active area and a 50×50 μm^2 SPAD size. Data regarding its PDE dependence on light wavelength and overvoltage applied were taken from datasheet figures. All simulations were performed assuming a SiPM operated at 3 V of overvoltage and an SPTR of 80 ps (sigma) [49]. As for BaF_2, a HPK VUV S13370-3050CN device was chosen as it allows light detection in the vacuum-UV. It shares the same dimension and SPAD distance as the 13360-3050PE SiPM but it exhibits a worse SPTR ($\sigma_{\mathrm{SPTR}} = 140$ ps [49]). As the PDE along BaF_2 emission range was not provided by the datasheet, a constant 20%

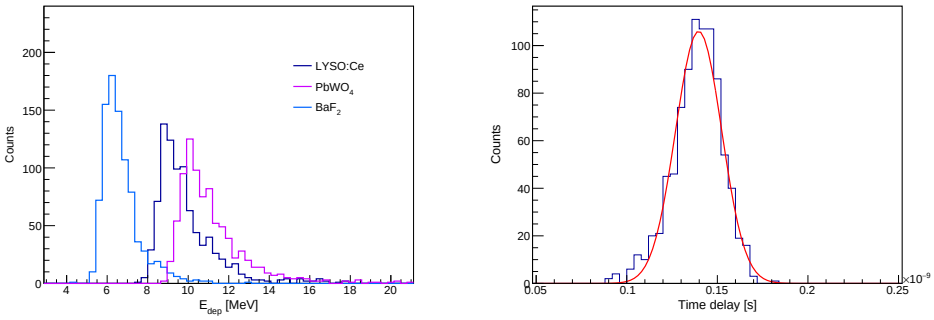

Figure 7.1: Energy deposited by the π^+ beam in 10 mm long LYSO:Ce, $PbWO_4$ and BaF_2 (left) and timestamps distribution extracted from a $2 \times 2 \times 10$ mm^3 LYSO:Ce pixel fitted using a Gaussian function (right).

PDE was assumed.

7.4 Simulations Outputs

7.4.1 Energy Deposition and Time Performance Evaluation

A pivotal output of the simulation software is given by the amount of energy deposited by the incident pion beam inside the material. Examples of energy distributions are shown in Figure 7.1 (left).

As for the time resolution evaluation, the timestamps evaluated from the digitalized waveforms at a fixed threshold are employed to fill a histogram as the one presented in Figure 7.1 (right). The time performance reached by the simulated detector is therefore evaluated as the standard deviation of the Gaussian function fitting the data distribution. To identify the threshold leading to the best time resolution, a scan over it is performed over each simulated crystal, in a similar fashion as illustrated for CTR measurements in previous chapters. The time resolution of the detector is finally obtained from the fit minimum of these graphs. Threshold scans of length variable LYSO:Ce pixels are displayed in Figure 7.2 as an example.

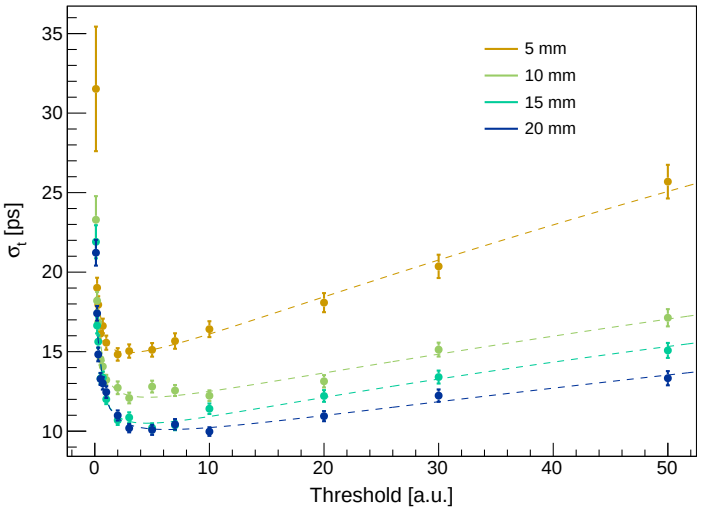

Figure 7.2: Time resolution achieved for $2 \times 2 \times L$ mm^3 LYSO:Ce crystals (with L = 5, 10, 15 or 20 mm) against the threshold employed to extract the timestamp from the digitalized pulses in output from the simulations. The time performance of each detector is evaluated at the fit minimum. As the single SPAD pulse simulated has an amplitude of about 0.6 in these arbitrary units, the optimum is usually achieved for a threshold corresponding to about 10 times the single SPAD amplitude.

7.4.2 LYSO:Ce Pixel Length Scan

The time resolution of a LYSO:Ce pixel was evaluated by varying the crystal length along the pion beam direction between 2.5 mm and 20 mm (see Figure 7.3). The performance achieved improves with the crystal length as the incoming particle deposits more energy and more photons are generated. Above 15 mm length, no significant improvement was observed.

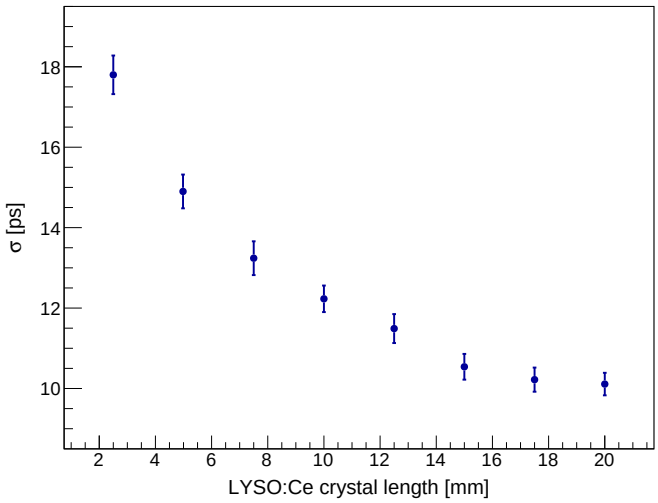

Figure 7.3: Time resolution in output of the simulations of $2 \times 2 \times L$ mm^3 LYSO:Ce pixels as a function of the length L of the crystal.

7.4.3 Time Resolution across Various Materials

The energy deposited on average by the incoming pion beam as well as the time resolution achieved for beam detection was evaluated through the simulation framework for pixels made of different materials. The results obtained are reported in Table 7.1 and displayed one against the other in the plot in Figure 7.4.

The material performing the best with $\sigma = 11.8 \pm 0.3$ ps was LSO:Ce,Ca. This was also confirmed experimentally by previous studies performed on LSO:Ce,Ca, LYSO:Ce and aluminium garnet crystals [109, 110]. In general, the time resolution output values obtained for LSO:Ce,Ca, LYSO:Ce, GFAG and BaF_2 is similar. Remarkably, the performance of BaF_2 stands out, considering that the SiPM used to detect its light has significantly lower PDE and a poorer SPTR when compared to the visible light-sensitive photodetectors employed for the other pixels. Moreover, BaF_2 delivers impressive timing performance despite relatively low energy deposition by high-energy charged particles within the detector. This characteristic offers the advantage of requiring less material budget in front of a hypothetical calorimeter compared to other materials of the same length.

As for the material simulated whose timing performance is mainly determined by Cherenkov light, i.e. BGO and $PbWO_4$, the resolution obtained is considerably worse, due to the poor amount of light generated by the Cherenkov effect.

Crystal material	$\mathbf{E_{dep}}$	σ
LYSO:Ce	9.9 ± 0.1 MeV	12.2 ± 0.3 ps
LSO:Ce,Ca	10.3 ± 0.1 MeV	11.8 ± 0.3 ps
GFAG	9.6 ± 0.1 MeV	14.7 ± 0.4 ps
BGO	9.8 ± 0.1 MeV	36.6 ± 0.9 ps
$PbWO_4$	11.1 ± 0.2 MeV	29.4 ± 0.8 ps
BaF_2	6.7 ± 0.1 MeV	12.5 ± 0.3 ps

Table 7.1: Average energy deposited by the pion beam and time resolution achieved for the crystal materials simulated.

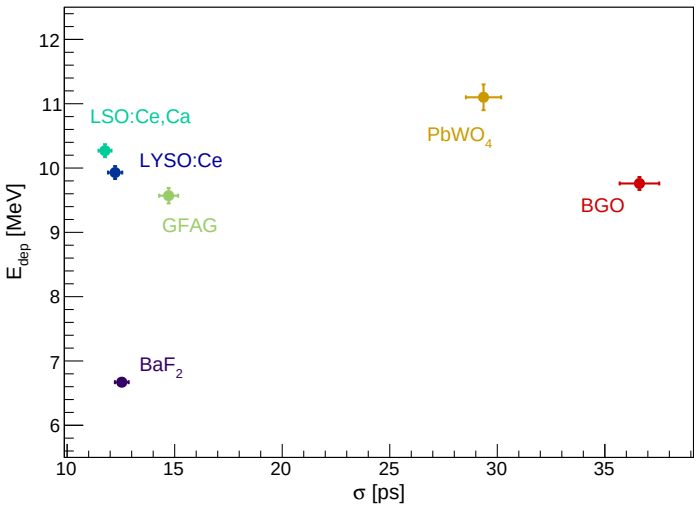

Figure 7.4: Average energy deposited by the pion beam in each of the six simulated pixels against the time performance achieved.

Chapter 8

Testbeam Campaigns for Studies on Charged Particle Timing Detectors

In light of the promising results obtained from simulations, a series of crystal detector tests were conducted at the CERN Super Proton Synchrotron (SPS) facility along the H2 extraction beamline during two separate testbeam sessions.

The first campaign, which took place in September 2022, was primarily focused on exploring the timing capabilities of conventional dense scintillators, Cherenkov radiators, BaF_2 and BaF_2:Y coupled to silicon detectors. These tests made use of custom high-frequency electronics for signal readout. Additionally, this initial testbeam provided a valuable opportunity to investigate critical parameters of the measurement campaign, such as the overvoltage applied to the SiPM detectors and the radiation damage brought by the particle beam on these detectors.

Building on the knowledge gained during the 2022 testbeam, a second testbeam session was conducted in June 2023. This session involved testing a new group of samples, including a GAGG:Ce,Mg pixel from a second production batch, a BSO crystal manufactured by SICCAS, and BaF_2 and BaF_2:Y samples with improved geometry and SiPM coupling. The same readout electronics and particle beam detection chain used in the 2022 campaign were employed also for the 2023 campaign. Notably, the main distinction between this testbeam campaign and the first was the implementation of a temperature stabilization system within the box containing the samples.

This chapter begins by detailing the materials examined and the measurement setups used during the two testbeam campaigns. Subsequently, the data analysis procedure is outlined, and the resulting findings are presented and discussed. To conclude, a com-

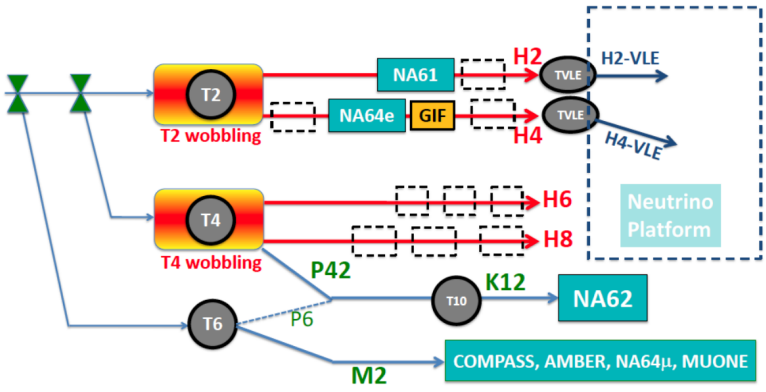

Figure 8.1: Simple schematics of SPS North Area beamlines at CERN. From reference [111].

parative analysis is provided between time performances achieved in the testbeams in relation to the expectations derived from simulations.

8.1 Materials and Methods

8.1.1 Testbeams Facility

The CERN SPS facility serves a dual purpose as an injector for the LHC and as a source of test beams for the North Area on the Prevessin site. As depicted in Figure 8.1, in this facility the primary proton beam from the SPS is sent towards some targets (T2, T4, T6), generating secondary particles which are then filtered through magnet spectrometers and fed into test beamlines (H2, H4, H6, H8). This setup allows the facility to provide a wide variety of particle beams, encompassing leptons ($e^{\pm}$, $\mu^{\pm}$) and charged hadrons ($\pi^{\pm}$, $K^{\pm}$, p), with energies ranging from a few tens to hundreds of GeV in few seconds long spills to different beamlines.

8.1.2 Testbeam Setups

A simplified sketch of the setup employed for 2022 and 2023 testbeams is illustrated in Figure 8.2 and a picture of it is shown in Figure 8.3.

Following the beam trajectory, positioned in front of the light-tight experimental box during both the 2022 and 2023 testbeams were:

- **two plastic scintillating pads** providing the hardware trigger of the incident particle arrival.

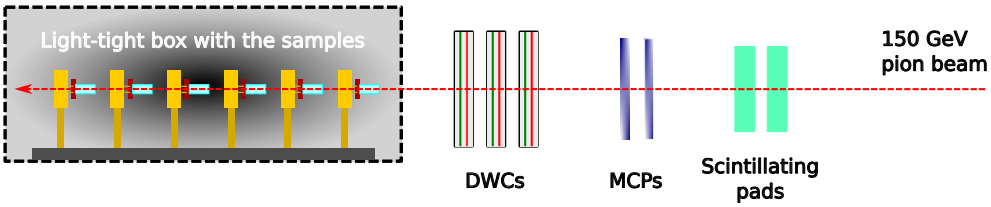

Figure 8.2: Schematics of the experimental setup employed in both testbeams for the measurement of the time performance achieved by the crystal samples under 150 GeV pions irradiation. Inside the light-tight box, the crystal samples (in light blue) coupled to their SiPMs (in brown) are traversed along their length by the pion beam. Their readout boards are stored in a metal case (in yellow in the sketch) and kept in place by custom-made supports.

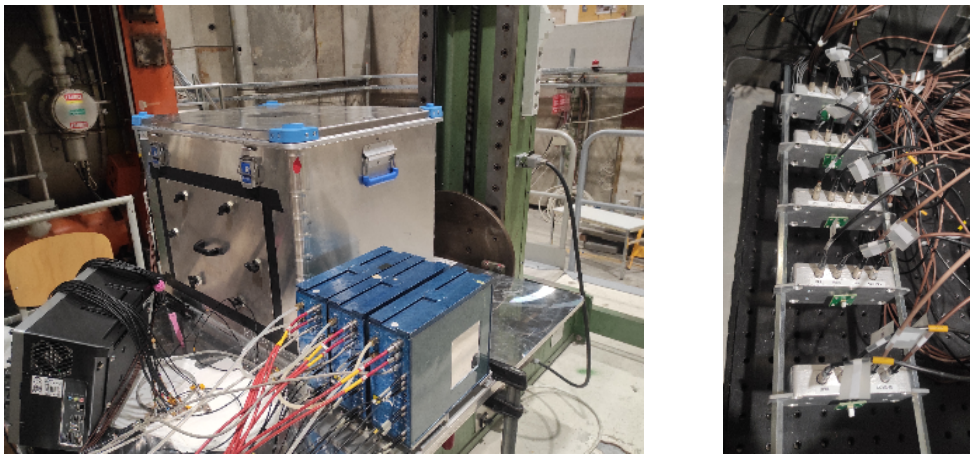

Figure 8.3: Pictures from the 2023 testbeam of the dark-tight box housing the samples with three DWCs in front of it (left) and of the samples connected to their respective readout boards, shielded by a metal case (right).

- **two microchannel plate detectors (MCPs)** in combination establishing the time reference. To determine the timestamp of each MCP, constant fraction discrimination was applied at 30 % on the digitized waveform. The average of the two timestamps obtained from the MCPs was employed as time reference with time resolution assessed on a run-by-run basis, ranging from 13 and 15 ps in standard deviation.

- **three delay wire chambers (DWCs)** tracking the incoming beam. The chambers were filled with a mixture of Ar/CO_2 gas and a CAEN TDC (model V1290N) was employed for the DWCs readout.

The samples were housed in a light-tight box installed on a DESY table moving in the plane orthogonal to the beam direction. Each crystal-SiPM detector was attached to a readout board shielded through a metal case. Custom-made supports were used to secure and align the samples and their board with the beam. The setup employed in 2022 allowed the simultaneous measurement of up to six samples, while in 2023 the amount of supports to be employed concurrently was reduced to five. One of the measurement slots was always occupied by a $2 \times 2 \times 3$ mm^3 LYSO:Ce,Ca sample from FLIR to monitor drifts of the experimental setup.

In a similar fashion as illustrated for the CTR bench working at 511 keV and exploiting high-frequency electronics, the signals detected by each SiPM were split into two branches: the former fed into an analog amplifier for the energy signal extraction, the latter read out by custom-made high-frequency electronics providing the time information. About one-meter-long cables were employed within the experimental box to establish connections between each readout board and a patch panel located on the box's surface. A few meters long cables were employed to connect the patch panel to the electronics rack or to power suppliers providing a bias voltage either for the SiPMs or the operational amplifiers for the front-end electronics.

The Data Acquisition system (DAQ) consisted of several electronic modules. NIM modules were employed to control trigger logic. To bias the MCPs and the DWCs, a CAEN high-voltage power supply was used, which could be remotely controlled through a CAEN GECO2020 interface. The time and energy pulses of the samples as well as the MCPs signals were fed into a CAEN V1742 Digitizer module based on a DRS4 chip [112] sampling waveforms at rates up to 5 GS/s and having a 500 MHz bandwidth for timing measurements.

The main difference between the two testbeam setups lies in the temperature stabilization system, which was implemented in 2023 to avoid temperature-related drifts in the measurement conditions of the SiPMs and the other electronic components in the experimental box. Along all the 2023 testbeam campaign, the box was kept at the stable temperature of 16 °C.

8.1.3 Materials Tested: Crystals and SiPMs

The crystal samples investigated for these studies and their manufacturers are listed in Table 8.1. All crystals exhibited mirror-polished surfaces, were wrapped in several layers of Teflon and attached to a SiPM via one of their smaller surfaces. The majority of the samples exhibited a good internal condition without apparent defects. The sole exceptions were the BGSO sample, which displayed some impurities within its bulk, and the GAGG:Ce,Mg crystal from the first production batch, which revealed a significant crack at its core.

With the exception of BaF_2 and BaF_2:Y, the samples were glued with Cargille Meltmount to Hamamatsu Photonics SiPMs model S13360-3050PE, featuring a 50 μm SPAD size and an active area measuring 3×3 mm^2.

In the case of undoped and Y-doped BaF_2, their light readout was realized using vacuum-UV sensitive Hamamatsu Photonics SiPMs. A thin layer of Viscasil 100M optical grease was applied to improve light extraction out of the crystals. Previous studies have confirmed the excellent transparency of this silicon-based grease to the cross-luminescent emission of BaF_2 in the deep UV [113, 34]. In the 2022 testbeam campaign, $3 \times 3 \times 10$ mm^3 BaF_2 samples were coupled to HPK S13370-6050CN SiPMs, having 50 μm SPAD dimension and a larger 6×6 mm^2 active area. On the other hand, smaller BaF_2 samples of size $2 \times 2 \times 10$ mm^3 were tested in the 2023 campaign and read out through HPK S13370-3050CN SiPMs, having the same SPAD dimensions, but smaller active area (3×3 mm^2). These SiPMs were powered at 58 V for these testbeams campaigns.

To maintain alignment with the beam axis, both the BaF_2 and BaF_2:Y samples and their respective SiPMs were secured in position using a 3D-printed plastic holder (see Figure 8.4).

Some of the scintillating and timing properties of the samples employed are also reported in Table 8.2. Values presented in the table include both literature data and experimental measurements conducted in laboratory, following the same methodology and equipment detailed in Sections 3.3 and 3.4.1 for light output and scintillation kinetics, respectively.

As for the light output measurements, ^{137}Cs was employed as excitation source. The samples labelled with ^{a} were matched using Rhodorsil grease to a Hamamatsu Photonics R2059 PMT. In contrast, BaF_2 and BaF_2:Y samples, marked with ^{b} were directly coupled to a vacuum-UV sensitive Hamamatsu Photonics H6610 PMT without any optical coupling.

Sample material	**Producer**	**Dimensions** [mm^3]	**Testbeam campaign** **2022**	**2023**
LYSO:Ce	*CPI*	$2 \times 2 \times 10$	✓	
LSO:Ce,Ca	*Agile*	$2 \times 2 \times 10$	✓	
GFAG	*C&A*	$2 \times 2 \times 10$	✓	✓
GAGG:Ce,Mg (1^{st} batch)	*FZU Prague*	$2 \times 2 \times 10$	✓	
GAGG:Ce,Mg (2^{nd} batch)	*FZU Prague*	$2 \times 2 \times 10$		✓
EJ232	*Eljen Technology*	$3 \times 3 \times 3$	✓	
BGO	*EPIC*	$2 \times 2 \times 10$	✓	✓
BGSO	*ISMA*	$2 \times 2 \times 10$	✓	✓
BSO	*SICCAS*	$2 \times 2 \times 10$		✓
$PbWO_4$		$2 \times 2 \times 10$	✓	
PbF_2	*EPIC*	$2 \times 2 \times 10$	✓	
BaF_2	*SICCAS*	$3 \times 3 \times 10$	✓	
BaF_2: 1 mol.% Y	*SICCAS*	$3 \times 3 \times 10$	✓	
BaF_2: 3 mol.% Y	*SICCAS*	$3 \times 3 \times 10$	✓	
BaF_2: 5 mol.% Y	*SICCAS*	$3 \times 3 \times 10$	✓	
BaF_2: 10 mol.% Y	*SICCAS*	$3 \times 3 \times 10$	✓	
BaF_2	*SICCAS*	$2 \times 2 \times 10$		✓
BaF_2: 3 mol.% Y	*SICCAS*	$2 \times 2 \times 10$		✓

Table 8.1: List of the samples measured during the two testbeams, including their producer and size. The checkmarks indicate whether the sample was measured in the 2022, 2023, or both testbeam campaigns.

Figure 8.4: BaF_2 samples and their SiPM kept in place within black 3D-printed plastic holders. The detector on top, whose holder houses a Teflon-wrapped $3 \times 3 \times 10$ mm^3 sample coupled to a 6×6 mm^2 SiPM, was measured in the 2022 testbeam, while the one on the bottom was tested in 2023 and is composed of a $2 \times 2 \times 10$ mm^3 crystal coupled to a 3×3 mm^2 SiPM.

Sample material	**Density** [g/cm^3]	**Refractive index**	**Decay time(s)** [ns]	**Light output** [ph/MeV]
LYSO:Ce [43]	7.1	1.81	24 (15 %) 45 (85 %)	27 000
LSO:Ce,Ca [43]	7.4	1.81	8 (6 %) 33 (94 %)	22 000
GFAG [108]	6.6	1.92	41 (65 %) 172 (35 %)	32 000
GAGG:Ce,Mg [114]	6.6	1.92	1.3 (8 %) 10 (43 %) 42 (49 %) *	17 000 [a]
EJ232 [115]	1.0	1.58	1.6 (100 %)	8 400
BGO [60]	7.1	2.15	2.0 (1 %) 42 (7 %) 337 (92 %) *	9 300 [a]
BGSO [60]	7.1	2.1	2.0 (1 %) 40 (17 %) 174 (82 %) *	3 100 [a]
BSO [60]	7.1	2.1	2.9 (2 %) 27 (10 %) 107 (88 %) * *	1 800 [a]
$PbWO_4$ [24]	8.3	2.16	6 (100 %)	100
PbF_2 [116]	7.8	1.77	-	-
BaF_2 [117]	4.9	1.55	0.04 (1 %) 0.7 (5 %) 643 (94 %) *	3 700 [b]
BaF_2: 1 mol.% Y [117]	4.9	1.55	0.03 (1 %) 0.7 (30 %) 294 (69 %) *	890 [b]
BaF_2: 3 mol.% Y [117]	4.9	1.55	0.04 (1 %) 0.7 (29 %) 318 (70 %) *	1 100 [b]
BaF_2: 5 mol.% Y [117]	4.9	1.55	0.03 (1 %) 0.7 (32 %) 303 (67 %) *	810 [b]
BaF_2: 10 mol.% Y [117]	4.9	1.55	0.06 (5 %) 0.7 (52 %) 145 (43 %) *	530 [b]

Table 8.2: Summary of some physical, scintillation and timing properties of the materials tested for these studies. The scintillation kinetics of the samples marked with * was measured under X-ray excitation with the setup described in Section 3.4.1, while the light output was measured in the test bench illustrated in Section 3.3 using a ^{137}Cs excitation source with a Hamamatsu Photonics R2059 PMT and Rhodorsil grease ($n = 1.41$) as optical coupling [a] or a vacuum-UV sensitive Hamamatsu Photonics H6610 PMT and dry-coupling [b]. The non-marked values were instead taken from literature.

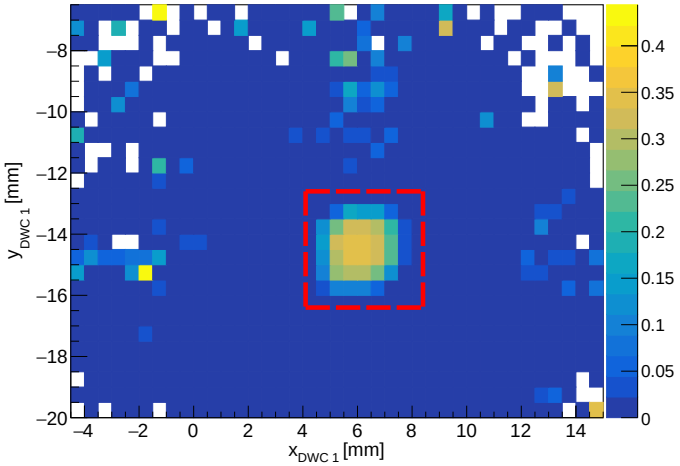

Figure 8.5: Two-dimensional histogram depicting the transverse position of the incident beam as measured by one of the three DWCs in relation to the signal amplitude detected in the $2 \times 2 \times 10\,\mathrm{mm}^3$ LYSO:Ce pixel. The area delimited by the red square encompasses the events in which the incoming pion traversed the entire length of the pixel.

8.2 Data analysis

In this section, a description of the steps involved in data analysis, including event exclusion criteria and applied corrections, is provided.

Event tagging and tracking

A preliminary event selection was conducted based on the recoded energy deposition inside the MCPs. Additionally, a subsequent filtering criterion was applied, which involved the precise determination of the beam's x-y crossing position through the three DWCs, providing tracking information with a 200 μm precision. By examining a two-dimensional histogram of the x-y coordinates recorded by each chamber alongside the corresponding amplitude registered in the crystal for the event (an example is illustrated in Figure 8.5), events in which the pion failed to interact with the crystal were effectively excluded from the analysis. For each DWC and sample, the delimiting region for event selection was slightly larger than the expected physical dimension of the crystal. Therefore the events that passed this filtering criterion were those with x-y coordinates valuea within the selected area for each DWC.

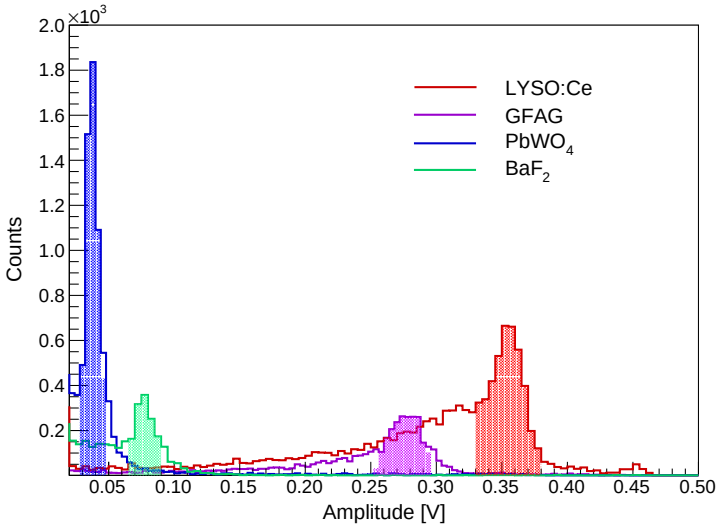

Figure 8.6: Energy signal amplitude distributions for LYSO:Ce, GFAG, $PbWO_4$, and BaF_2 samples. The highlighted regions contain the events where the incoming pion deposited some of its energy along the entire sample length..

Energy signal amplitude

For each sample and event, the amplitude was determined by calculating the difference between the baseline of the analog energy pulse, computed as the average over the first 200 samples, and its maximum value. Some examples of observed amplitude distributions are presented in Figure 8.6. As indicated by simulations, the events represented by the peak in the distributions are those in which the pion travelled the entire length of the crystal, making them the events selected for analysis. The continuum with smaller amplitudes includes events in which the pion only partially traversed the sample due to beam divergence from the beam axis.

Timestamp extraction and time resolution calculation

On one hand, the timestamp of the reference MCPs was determined through constant fraction discrimination at 30 % of the amplitude of their signal. On the other hand, a leading edge threshold scan was conducted on the time pulses of each crystal sample to identify the settings yielding the best time resolution.

Starting from the events selected, a distribution of the time delay $\Delta t(\theta)$ between the threshold crossing time $t_s(\theta)$ of the signal generated in the crystal and the average timestamp of the two MCPs, expressed as $\Delta t(\theta) = t_s(\theta) - (t_{\mathrm{MCP}\,1} + t_{\mathrm{MCP}\,2})/2$

was created for each sample varying the leading edge threshold θ set on the time pulse. Gaussian functions were employed to model such delay distributions, and the standard deviation σ obtained from the fit provided the measured CTR (σ_{meas}) between the sample and the reference MCPs. To subtract the contribution of the MCPs (σ_{MCPs}) and assess the time resolution of the individual photodetector, the following calculation was performed:

$$\sigma_{\text{sample}} = \sqrt{\sigma^2_{\text{meas}} - \sigma^2_{\text{MCPs}}}. \tag{8.1}$$

Time-walk effect

Due to the significant Landau fluctuations in the energy deposition of the incoming particles, an expected time-walk effect occurred due to the leading edge threshold discrimination. This resulted in a more or less pronounced correlation between the time delay and the signal amplitude depending on the sample, as previously observed in [109, 110]. A showcase of this effect is provided in Figure 8.7, where a two-dimensional histogram of the time delay versus amplitude is shown for the LYSO:Ce sample at 400 mV threshold set on the time signal. By modelling this correlation with a linear function and subsequently adjusting the time delay distributions to account for this correction, a notable enhancement in time performance was observed for many samples, as depicted in Figure 8.8.

This procedure was repeated by varying the leading edge threshold on the time signal in order to find the setting leading to the best possible value. A threshold scan, which accounts for the time-walk effect and evaluates the time resolution, is presented in Figure 8.9 for several of the tested samples.

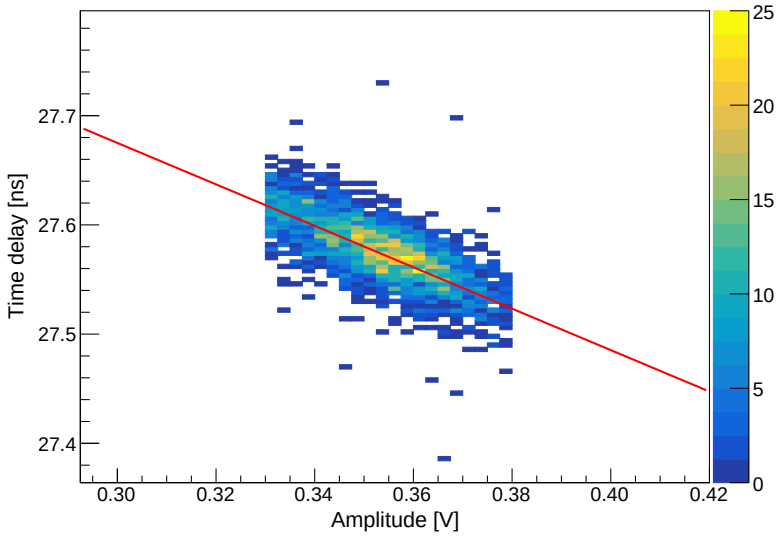

Figure 8.7: Scatter plot of the time delay Δt versus the energy pulse amplitude for the LYSO:Ce sample, with a 400 mV threshold applied on the time signal. A linear fit was used to model the correlation between these two variables.

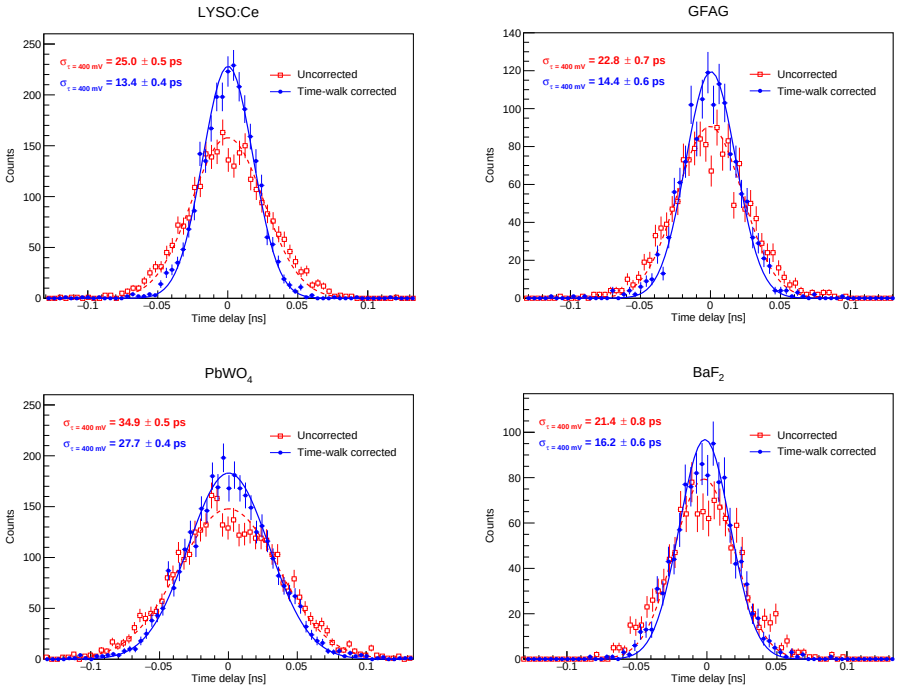

Figure 8.8: Time delay distributions for some selected samples, considering both cases with and without time-walk correction.

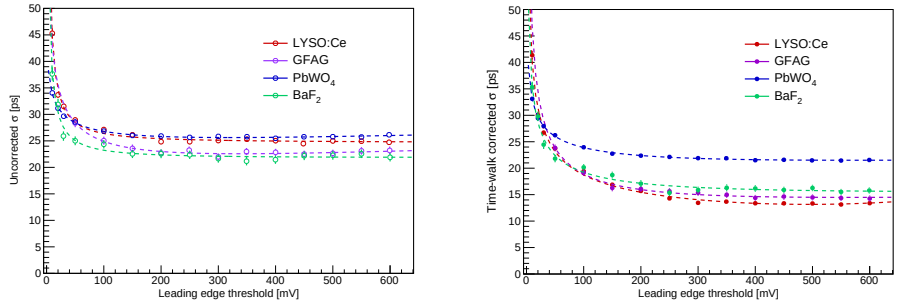

Figure 8.9: Leading edge threshold scan of uncorrected (left) and time-walk corrected (right) time resolutions for some tested samples. The time resolution associated with each sample is the one corresponding to the fit minimum.

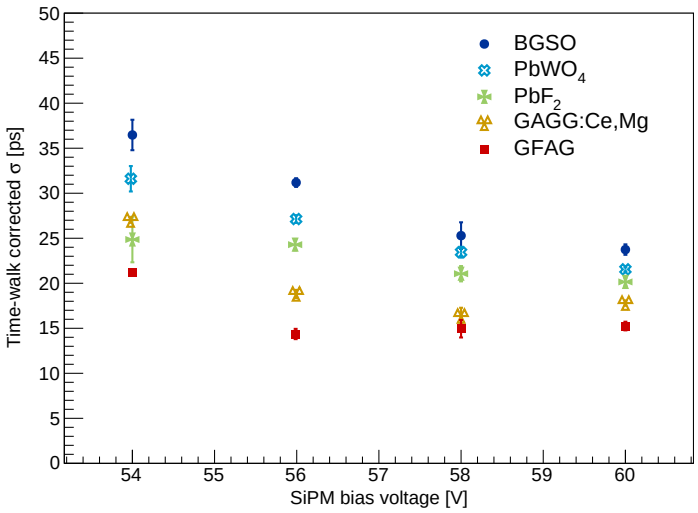

Figure 8.10: Time resolution, corrected for time-walk effect, of various crystals plotted against the SiPM bias voltage.

8.3 Results Discussion

8.3.1 2022 Testbeam

SiPM bias voltage scan

To assess the impact of the SiPM overvoltage on time resolution, a preliminary bias voltage scan was conducted on some selected samples (GFAG, GAGG:Ce,Mg, BGSO, $PbWO_4$ and PbF_2). Figure 8.10 shows the time-walk corrected values of σ plotted against the SiPM bias voltage. Generally, an improvement in time performance was observed with increasing SiPM overvoltage, corresponding to an enhanced PDE. However, it is worth noting that when SiPMs were powered above 58 V signal degradation occurred, leading to increased baseline fluctuations and spurious noise events during data acquisition. As a result, all other samples were measured at a 56 V bias voltage.

Samples time performance

Both uncorrected and time-walk corrected values of the time resolution of the samples tested in 2022 testbeam are reported in Table 8.3.

LYSO:Ce and LSO:Ce,Ca, when coupled to Hamamatsu SiPM, exhibited improved time resolutions of 13.1 ps and 12.1 ps, respectively, in contrast to earlier studies

Sample	**Dimensions** [mm^3]	**E $_{\mathbf{dep}}$** [MeV]	σ **$_{\mathbf{uncorr}}$** [ps]	σ **$_{\mathbf{TW\ corr}}$** [ps]
LYSO:Ce	$2\times2\times10$	9.9	24.7 ± 0.5	13.1 ± 0.4
LSO:Ce,Ca	$2\times2\times10$	10.3	19.4 ± 0.4	12.1 ± 0.4
GFAG	$2\times2\times10$	9.6	22.6 ± 0.7	14.3 ± 0.6
GAGG:Ce,Mg	$2\times2\times10$	9.6	20.7 ± 0.5	18.8 ± 0.5
EJ232	$3\times3\times3$	0.5	19.8 ± 0.2	17.2 ± 0.2
BGO	$2\times2\times10$	9.8	41.4 ± 2.1	36.4 ± 1.5
BGSO	$2\times2\times10$	9.8	34.3 ± 0.6	31.1 ± 0.5
$PbWO_4$	$2\times2\times10$	11.1	31.4 ± 0.5	27.0 ± 0.4
PbF_2	$2\times2\times10$	10.3	37.8 ± 1.2	24.2 ± 0.6
BaF_2	$3\times3\times10$	6.7	21.8 ± 0.8	15.8 ± 0.6
BaF_2: 1 mol.% Y	$3\times3\times10$	6.7	20.1 ± 0.4	16.0 ± 0.4
BaF_2: 3 mol.% Y	$3\times3\times10$	6.7	20.4 ± 0.4	17.0 ± 0.4
BaF_2: 5 mol.% Y	$3\times3\times10$	6.7	20.2 ± 0.5	17.7 ± 0.5
BaF_2: 10 mol.% Y	$3\times3\times10$	6.7	20.6 ± 0.3	15.7 ± 0.3

Table 8.3: Summary of the single detector time resolutions (both uncorrected and time-walk corrected) measured for the samples tested in the 2022 campaign. The average energy deposition by a 150 GeV charged pion within the crystal is also provided.

[109, 110]. Such a disparity may be attributed to the utilization of different readout electronics. As detailed in [46], the custom high-frequency amplifiers employed in this study demonstrated superior time performance compared to the NINO electronics used in [109, 110], owing to their higher bandwidth and speed. GFAG, on the other hand, achieves a result of 14.3 ps, which is remarkably close to that of LYSO:Ce. Although one would have expected similar performance for GFAG and the highly doped GAGG:Ce,Mg samples based on their scintillation properties, the presence of cracks within the GAGG:Ce,Mg sample and its imperfect surface condition may account for its worse time performance. In the case of the sole plastic scintillator tested (EJ232), a time resolution of 17.2 ps was obtained despite the material low density and Z_{eff} and the shorter length traversed by the pion beam, leading to an extremely low amount of energy deposited inside the sample.

Regarding materials in which a notable quantity of Cherenkov photons is produced, significantly contributing to their time performance, the overall time-walk corrected σ values obtained vary from 24 to 36 ps, thus achieving a worse performance compared to the other scintillators mentioned earlier. When compared to BGO, the BGSO sample exhibited a slightly improved time resolution which may be attributed to the compensation of its lower light output with faster scintillation kinetics. Among the Cherenkov radiators tested, $PbWO_4$ and PbF_2 demonstrated the best time perfor-

mance, reaching resolutions of 27.0 ps and 24.2 ps respectively. The high refractive index and wide transparency range of PbF_2, which enables it to harvest a substantial amount of Cherenkov photons on the SiPM, balance its lower density and lack of scintillation compared to $PbWO_4$, thus leading to a slightly better result for the PbF_2 sample.

Coherently with the CTR measurements at 511 keV reported in Section 5.2.5, the study conducted on BaF_2 samples doped with varying amounts of yttrium demonstrated that the time performance remained independent of the quantity of dopant used. Small variations in the values could be attributed either to potential sample-beam misalignment or suboptimal crystal-SiPM coupling. Moreover, all BaF_2 and BaF_2:Y samples achieved a time resolution of approximately 16 ps, which is only a few picoseconds worse than LYSO:Ce, the leading candidate for the MIP detector of CMS barrel [23]. This is particularly noteworthy considering the differences in measurement setup, such as larger sample sizes and suboptimal matching between the SiPMs' active area and the coupled face size of the crystal. A further notable factor is given by the fact that the energy deposited by a high energy charged particle in BaF_2 is lower with respect to LYSO:Ce, thus providing less material budget of a hypothetical timing detector in front of a calorimeter. A significant limitation of these materials is the low detection efficiency of their VUV SiPMs, in contrast to photosensors sensitive to longer wavelengths, which can achieve PDEs of around 60 % [46, 52, 78].

Correlation between scintillating and timing properties

As already illustrated in Section 8.11, for any scintillating crystal the time performance may be predicted using analytical models which take into account the scintillating properties of the material and certain detector characteristics. Considering almost crystal-independent the contributions related to light transport efficiency and the PDE of the SiPM, the expected time resolution can be linked to parameters such as the crystal effective decay time τ_d, its light output LO in photons/MeV and the energy deposited by the incident pion E_{dep}, as expressed below:

$$\sigma_{exp} \propto \sqrt{\frac{\tau_d}{LO \cdot E_{dep}}}. \tag{8.2}$$

In Figure 8.11 the time-walk corrected time resolution is plotted against the quantity $\sqrt{\tau_d/(LO \cdot E_{dep})}$ for those samples exhibiting significant light output and coupled to visible light-sensitive Hamamatsu SiPMs. With the exception of the GAGG:Ce,Mg sample, which has been discussed previously, the remaining data points follow a linear trendline within a certain approximation.

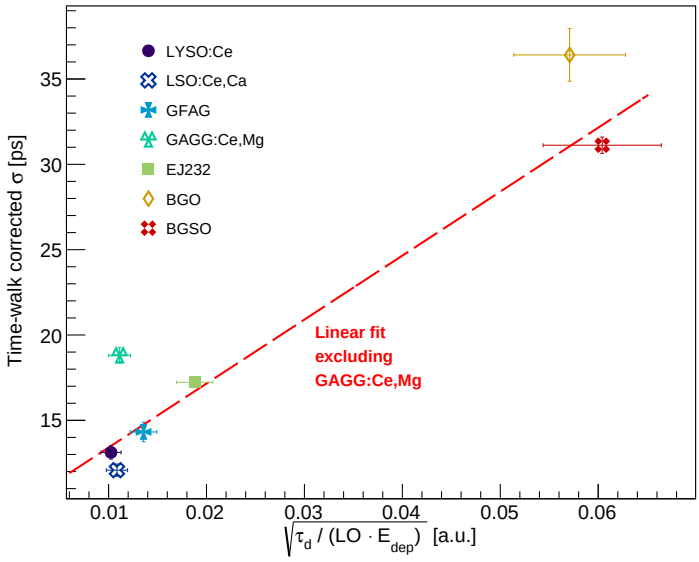

Figure 8.11: Time-walk corrected σ values of the samples exhibiting a large scintillation light yield against the quantity $\sqrt{\tau_d/(LO \cdot E_{\mathrm{dep}})}$ which is proportional to the expected time resolution. The red line fits the data points excluding the one corresponding to GAGG:Ce,Mg.

Considerations on the time-walk effect

To finalize the study on the samples measured during the 2022 testbeam, further work was pursued to gain a deeper understanding of the impact of the time-walk effect on various samples. When comparing the results with and without time-walk correction, significant enhancements in time performance were evident for crystals with low light output as well as for Cherenkov radiators. To analyze this further, the unsigned slope values $|m|$ were extracted from the linear fit of the 2D histogram plotting time delay versus the energy pulse amplitude, as the one presented in Figure 8.7. These slope values were determined at leading edge thresholds of 20, 100 and 500 mV. Subsequently, their absolute values were plotted against the average energy signal amplitude $\langle\varphi\rangle$ for events in which the pion traversed the entire length of the crystal, as shown in Figure 8.12. As outlined in [118], the fitting function for the data points is not trivial, but may be approximated as follows:

$$m(\langle\varphi\rangle) \simeq p_0/(\langle\varphi\rangle + p_1). \tag{8.3}$$

A good agreement may be noted between the modelling lines and the data points

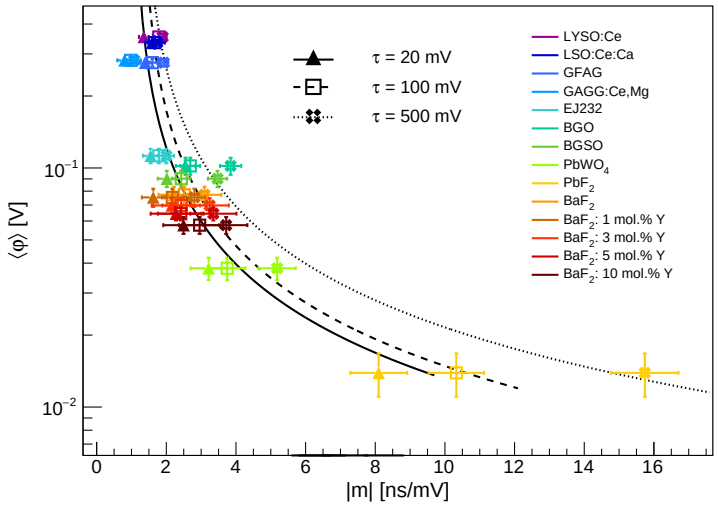

Figure 8.12: Average energy pulse amplitude $\langle\varphi\rangle$ produced by a charged pion traversing the full length of the crystal plotted against the unsigned slope $|m|$ obtained from the linear fit of the time delay - amplitude scatter plot (as shown in Figure,8.7) at 20, 100, and 500 mV thresholds on the time signal.

at various thresholds, indicating that time-walk correction has a more pronounced impact on samples with lower energy pulse amplitudes.

8.3.2 2023 Testbeam

Table 8.4 presents both uncorrected and time-walk corrected values of the time resolution for the samples tested during the 2023 testbeam.

In general, the time performance of the samples tested in both testbeams, i.e. GFAG, BGO, and BGSO, is consistent with the results from the first testbeam campaign. This indicates that temperature stabilization of the electronics had no significant impact on the obtained results.

Differently from the sample grown in the first batch, the highly doped GAGG:Ce,Mg sample measured in 2023 testbeam achieved a time resolution of 13.3 ps, which is in line with the result obtained for GFAG and expected according to [114]. As for the BGO, BGSO and BSO samples, the best time performance of about 33 ps is measured for the BGSO sample, in agreement with the timing achieved at 511 keV [60].

The most impactful result obtained during the 2023 campaign came out from the $2 \times 2 \times 10$ mm^3 BaF_2 and BaF_2:Y samples, which both demonstrated a time perfor-

Sample	**Dimensions** [mm^3]	**E $_{\mathbf{dep}}$** [MeV]	σ **$_{\mathbf{uncorr}}$** [ps]	σ **$_{\mathbf{TW\ corr}}$** [ps]
GFAG	$2 \times 2 \times 10$	9.6	18.1 ± 0.8	14.1 ± 0.8
GAGG:Ce,Mg	$2 \times 2 \times 10$	9.6	19.3 ± 1.1	13.3 ± 0.9
BGO	$2 \times 2 \times 10$	9.8	43.5 ± 2.1	37.9 ± 0.9
BGSO	$2 \times 2 \times 10$	9.8	38.4 ± 2.2	32.9 ± 1.7
BSO	$2 \times 2 \times 10$	9.8	38.4 ± 2.2	35.7 ± 1.3
BaF_2	$3 \times 3 \times 10$	6.7	16.2 ± 0.4	14.3 ± 0.6
BaF_2: 3 mol.% Y	$3 \times 3 \times 10$	6.7	17.3 ± 1.1	13.4 ± 0.9

Table 8.4: Summary of the average energies deposited by the pion beam in each sample and their single detector time resolutions (both uncorrected and time-walk corrected) achieved in the 2023 testbeam campaign.

mance compatible with a LYSO:Ce sample of the same dimension and coupled to a photosensor of the same active area.

8.4 Measurements-Simulations Matching

The time resolutions measured during the testbeam campaigns were compared to the simulations realized using the Monte Carlo framework presented in the previous chapter. Figure 8.13 presents the agreement between experimental measurement and simulations. A contribution of $\sigma_{\text{setup}} = 4$ ps was assumed as an estimate for the intrinsic time resolution of the experimental setup and was added in quadrature to the simulation outputs reported in Section 7.4. The simulation data points are drawn with 1-standard-deviation error bands.

A good match is achieved between measurements and simulations. The only exception is given by the $PbWO_4$ sample, for which the simulations predict a ~ 3 ps worse value compared to the experimental value. This might be due to mismatches between the scintillating and timing properties fed into the software for this material and the real ones of the sample.

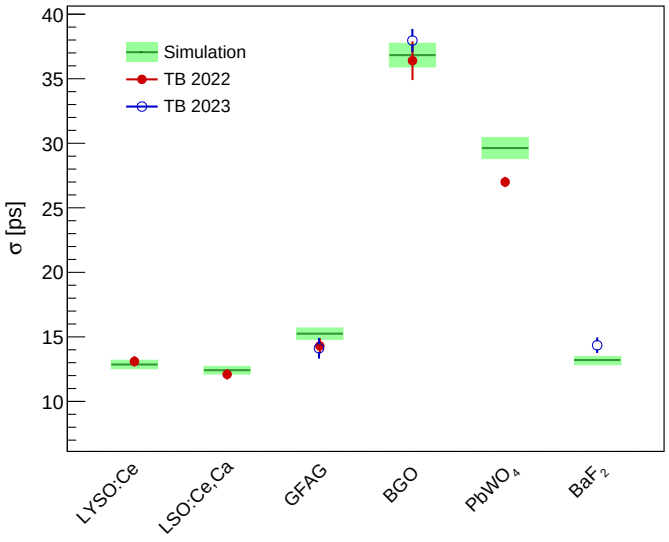

Figure 8.13: Comparison between single detector time resolutions under 150 GeV π^+ irradiation for several materials obtained from testbeam measurements (TB 2022 and TB 2023) and simulations. 1-standard-deviation error bands are drawn for the simulations output values.

8.5 Conclusions

These studies aimed to investigate the performance of numerous materials, including well-known dense scintillators and crystals exploiting either Cherenkov light or cross-luminescence for timing, as timing detectors for high energy charged particles.

The results obtained for the LYSO:Ce, LSO:Ce,Ca, and GFAG samples represent an extension and enhancement of previous tests that utilized different readout electronics. For instance, an optimal time resolution of approximately 12 ps was achieved for a $2 \times 2 \times 10$ mm^3 LSO:Ce,Ca sample coupled with a HPK S13360-3050PE SiPM. Additionally, various other materials, such as highly codoped GAGG:Ce,Mg, EJ232, BGSO, $PbWO_4$, and other Cherenkov radiators, exhibited noteworthy time performance, with time resolution values ranging from 13 to 38 ps.

Surprisingly, $3 \times 3 \times 10$ mm^3 BaF_2 and BaF_2:Y samples achieved an impressive time resolution of approximately 16 ps in 2022 testbeam, with no significant dependence on the quantity of yttrium used as a dopant. Furthermore, when measuring $2 \times 2 \times 10$ mm^3 BaF_2 and BaF_2:Y samples with improved geometry in 2023 campaign, a time performance compatible with LYSO:Ce was reached.

This work underscores the potential of numerous cost-effective materials that generate light through various mechanisms. Some of these materials have the capacity to compete with LYSO:Ce for precision timing applications in high radiation environments at future colliders.

Part IV

Studies on Dual Readout Calorimetry

Chapter 9

Simulation Studies for Dual Readout Capability in $PbWO_4$

The different response of a calorimeter to electromagnetic and hadronic showers represents a fundamental challenge in accurately reconstructing the energy of hadrons in calorimetry. As discussed in the introduction of this thesis, various techniques and approaches have been developed to address this issue. One particularly intriguing strategy in light-based calorimetry is the dual readout approach, extensively studied by the DREAM collaboration [19, 20]. The core principle of dual readout relies on the correlation between the production of Cherenkov light and the electromagnetic fraction f_{em} of a shower.

The objective of the studies conducted in this thesis is to explore the potential of utilizing dual readout to extract the f_{em} information on an event-by-event basis in a $PbWO_4$ crystal designed to longitudinally contain an electromagnetic shower. Knowledge of f_{em} can offer advantages in achieving a linear response to hadrons when combined with information obtained from a rear-mounted hadronic calorimeter.

This investigation was initially carried out through GEANT4-based Monte Carlo simulations. First, the influence of crystal size on dual readout capability was examined. Subsequently, the feasibility of utilizing pulse shape to extract event-specific f_{em} information was explored using machine learning techniques. The second phase of this research involved the verification of simulation findings through testbeam activities.

The chapter initially provides an overview of the simulation software employed. This framework is then utilized for two distinct studies. The initial study focuses on investigating the dual readout capability using variable-sized $PbWO_4$ crystals, following

the DREAM collaboration approach. Building on the findings gained from the initial test, the second objective involves identifying key features in the digitized waveforms extracted from simulated PMT readouts of a $3 \times 3 \times 22$ cm^3 $PbWO_4$ crystal to explore an alternative method for evaluating the event f_{em}. These computed features are subsequently input into a Python-based machine learning software, and the outcomes of this analysis are presented.

9.1 The Simulation Framework

The framework employed for these studies shares many components with the one introduced for charged particle timing detectors. It simulates a $PbWO_4$ crystal with variable geometry, and the generated light can be detected by a PMT sensor of adjustable size coupled to one of the crystal faces.

The procedures for primary particle generation, radiation-matter interaction, and light generation and propagation are identical to those described in Section 7.1. However, this software places a greater emphasis on the nature of optical photons, distinguishing whether they are produced via the Cherenkov or scintillation mechanisms, both at the generation and detection stages.

The generation of PMT signals follows the steps outlined in Section 7.2, with the only variation being the parametrization of the single photoelectron pulse. This parametrization is designed to better match the response of a PMT rather than that of a SiPM. The single photoelectron waveform over time is thus modelled as:

$$A(t) = \frac{A_0}{\sqrt{2\pi}\sigma} e^{-\frac{(t-\mu)^2}{2\sigma^2}}, \tag{9.1}$$

typically setting A_0 according to a narrow Gaussian distribution and $\mu \sim 3\sigma$.

9.2 Dual Readout Capability in a Variable-size $PbWO_4$ Crystal

To examine the impact of shower leakages, an evaluation of the Cherenkov and scintillation photons generated within $PbWO_4$ crystals of variable dimensions was conducted, aiming to replicate the plot depicted in Figure 1.11 for the simulated configurations.

In this investigation, 20 GeV electron and pion beams were directed towards the center of the crystal face. The average number of Cherenkov and scintillation photons, denoted as C_e and S_e, respectively, generated by a 20 GeV electron-initiated shower

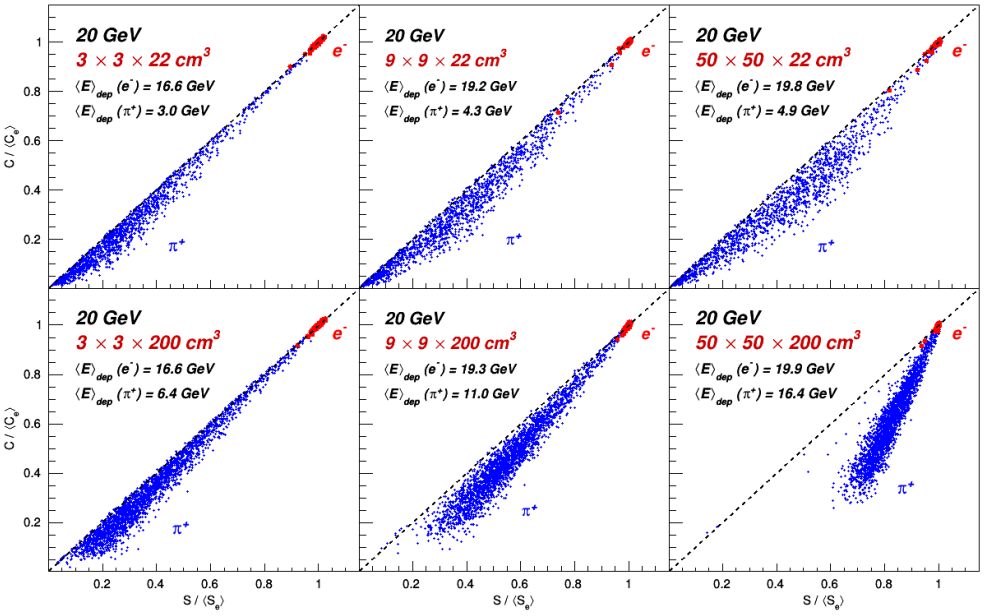

Figure 9.1: Scatter plots of the normalized number of Cherenkov and scintillation photons produced by 20 GeV electrons (red) and pions-induced showers (blue) for different $PbWO_4$ crystal sizes. The bisector $C = S$ was drawn as a dotted black line to better understand the applicability of the DREAM collaboration method to evaluate the f_{em} information.

served as a scaling factor for the number of photons of each type (C and S) produced on an event-by-event basis by the hadronic showers generated by the pion beam.

To explore different levels of containment for the hadronic showers, $PbWO_4$ sections of varying dimensions were simulated, including 3×3 cm^2, 9×9 cm^2, and 50×50 cm^2, as well as variable lengths of 22 cm and 200 cm.

Figure 9.1 displays the scatter plots for all the feasible combinations. As expected, an increase in crystal dimensions leads to a greater separation of the point cloud associated with the pion events from the bisector. Consequently, only the $50 \times 50 \times 200$ cm^3 crystal, capable of fully containing both longitudinally and transversely the hadronic shower, enables the effective application of the method detailed in Section 1.6 for evaluating f_{em} and compensating for the energy deposition of hadrons.

Given that the approach pioneered by the DREAM collaboration is inapplicable to small crystals, exploring alternative means of extracting f_{em} information even for smaller crystals, is an area of interest, as discussed in the subsequent sections.

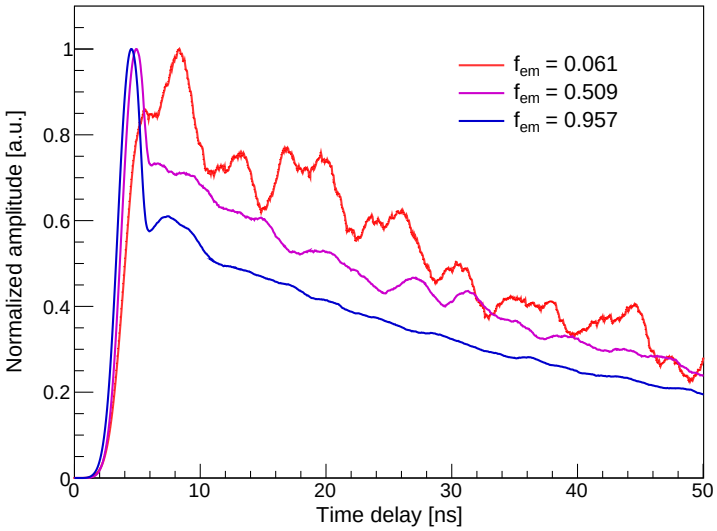

Figure 9.2: Examples of simulated waveforms that have been normalized over their amplitudes, representing events with low, medium, and high values of f_{em}. Noticeable differences in the pulse shapes are apparent to the naked eye.

9.3 Key Features of the Simulated Pulses

One potentially viable method for small-sized crystals is to exploit the pulse shape to extract quantities that may be related to the electromagnetic fraction of an event (see Figure 9.2). $PbWO_4$ is a suitable material for such an investigation, as the production of Cherenkov light in response to an electromagnetic shower is of the same order of magnitude as scintillation light.

A $3 \times 3 \times 22$ cm^3 $PbWO_4$ crystal, wrapped in a reflective material, with its light read out from one of its smaller faces was recreated using the simulation software. In this case, primary particles of 20 GeV electrons and pions were directed towards the center of the face opposite to the readout. A pivotal factor of this study is to minimize time jitters between photon production moment and waveform generation. To achieve this, the response of one of the fastest photomultipliers available on the market, namely the Hamamatsu R7600U-M4 multianode PMT, was simulated to detect the $PbWO_4$ light.

The key features of interest should ideally be independent of the primary particle energy and deduced solely from the pulse shapes. The features considered for this study, illustrated in Figure 9.3 include:

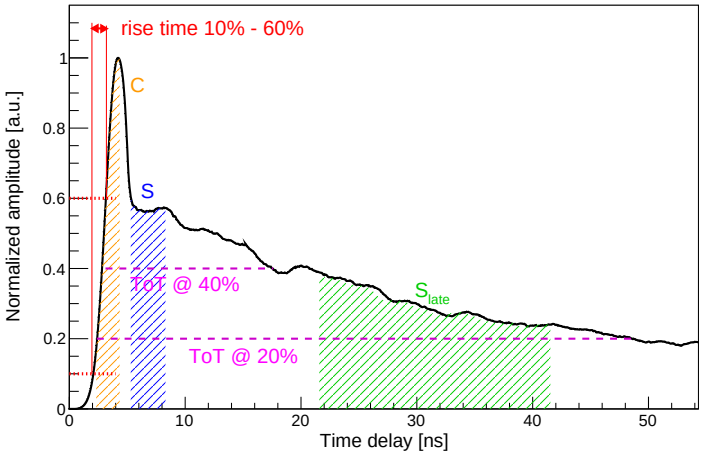

Figure 9.3: Main features extracted from an illustrative waveform.

- the ratios C/S and S_{late}/S, where C represents the integrated charge of the Cherenkov portion of the waveform in the initial 2 ns from the pulse start (t_0), S represents the integrated charge of early scintillation within the time range of $t_0 + 3$ ns to $t_0 + 6$ ns, and S_{late} represents the integrated charge of late scintillation between $t_0 + 20$ ns and $t_0 + 40$ ns;
- the time-over-threshold values at 20 % and 40 % of the pulse amplitude;
- the signal rise time, calculated between 10 % and 60 % of the waveform amplitude.

These quantities were plotted against the f_{em} of each event, as depicted in Figure 9.4. Notably, a clear correlation was observed for some of these quantities, with the most promising features being the time-over-threshold values and the C/S ratio.

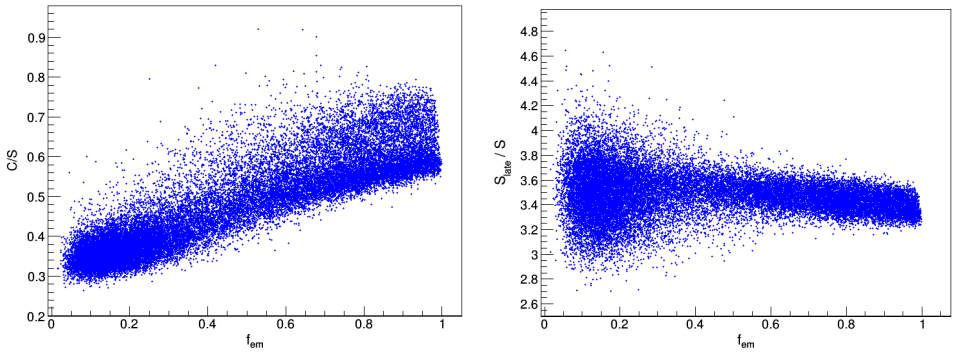

(a) C/S

(b) S_{late}/S

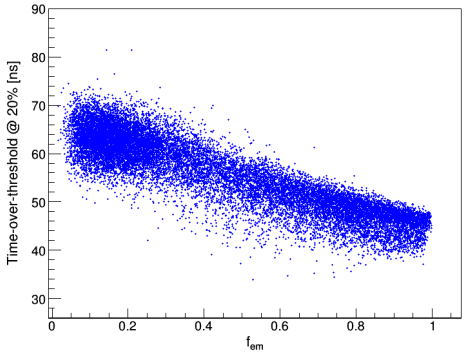

(c) Time-over-threhsold @ 20 %

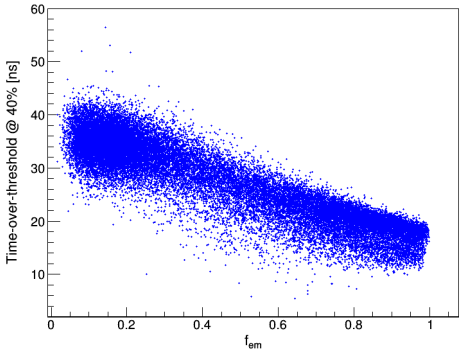

(d) Time-over-threhsold @ 40 %

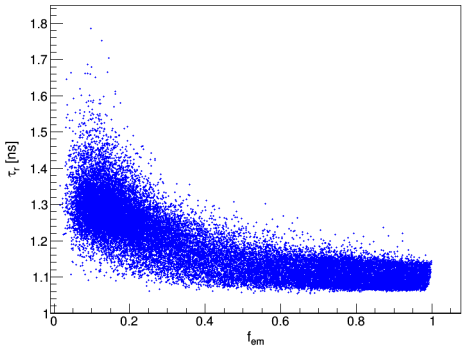

(e) Rise time

Figure 9.4: Features of interest plotted against the f_{em} of each hadronic event.

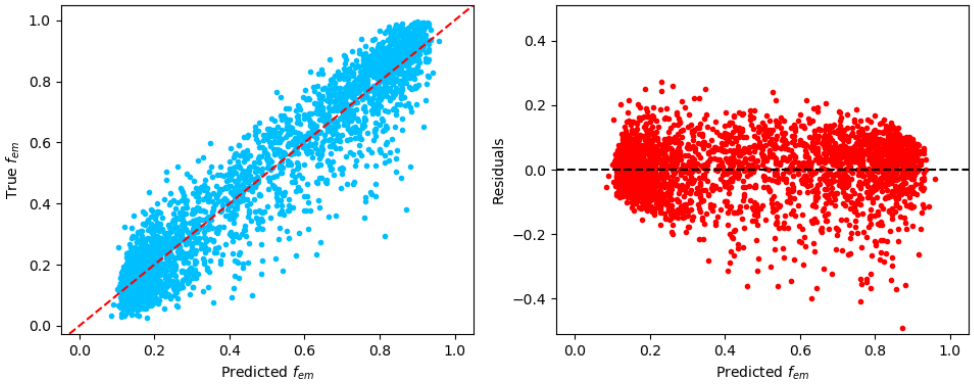

Figure 9.5: Left: true f_{em} value given in input to the machine learning program against the value predicted. Right: scatter plot of the residuals (true f_{em} - predicted f_{em}) versus the value of f_{em} predicted by the algorithm.

9.4 Extrapolation of the f_{em} through machine learning techniques

These features were then utilized as inputs for a Python-based machine learning algorithm to estimate the electromagnetic fraction from the test dataset. The most suitable model for this task was the GradientBoostingRegressor, a robust and versatile algorithm designed to handle intricate regression problems, specifically available in the scikit-learn library in Python.

Initially, all five features were provided as input to the algorithm. However, it was found that only the time-over-thresholds at 20 % and 40 % and the C/S ratio significantly contributed to an accurate prediction of f_{em}. Consequently, only these three features were used for the analysis. The dataset consisted of 30 000 samples, with 90 % allocated for training and 10 % for testing.

Figure 9.5 illustrates the results of the program, using the selected features for each dataset sample. The data points, representing the true and predicted values of f_{em} for each sample, are evenly clustered around the line from (0,0) to (1,1). On the left side, event-by-event residuals are plotted against the predicted values of f_{em} generated by the algorithm. The distribution of these residuals is subsequently presented in Figure 9.6, and it provides an estimate of the method precision in determining f_{em} with a resolution of 0.187 ± 0.010 FWHM.

The achievement of this resolution in f_{em} from the waveforms of a single fast detector represents a significant advancement compared to other methods that necessitate separate Cherenkov and scintillation readouts. Consequently, it is worthwhile to

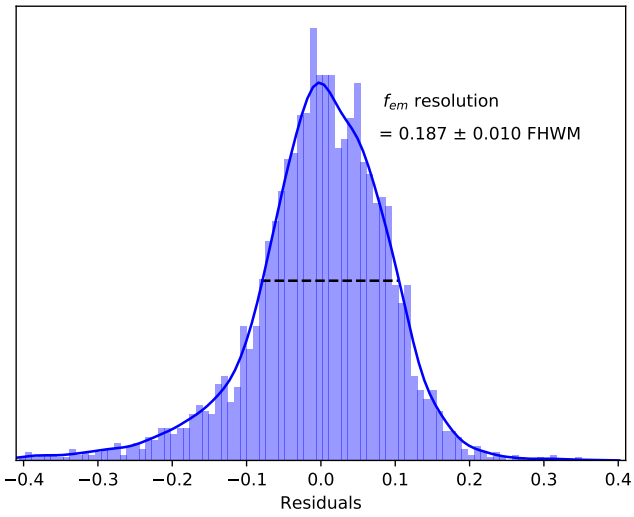

Figure 9.6: Distribution of the residuals in output from the machine learning algorithm. An average resolution of 0.187 ± 0.010 is achieved for f_{em} on all the events simulated.

explore its experimental feasibility, and the following chapter will delve into some studies in this direction.

Chapter 10

Testbeam Campaigns for Dual-Readout Studies

Along with the studies about charged particles timing detectors, during the testbeam campaigns conducted at the CERN SPS facility (H2 extraction line) in September 2022 and June 2023, an investigation into the dual readout capability of a $PbWO_4$ crystal measuring approximately $3 \times 3 \times 22$ cm^3 was carried out both with electrons and pions beams.

In the following chapter, an overview of the instrumentation utilized and the experimental setups employed is initially provided. Then, the results obtained in the 2022 testbeam, which focused on front-back anisotropy studies of $PbWO_4$, as well as the discrimination of Cherenkov and scintillation light using double side PMTs readout and optical filters, are presented. Subsequently, the findings obtained in 2023, aimed at investigating pulse shapes via single-ended PMT readout, are discussed. Finally, the outputs of these testbeams are commented upon and compared to the simulations illustrated in the previous chapter.

10.1 Materials and Methods

The $PbWO_4$ crystal employed for these studies does not have a regular shape. Its length is about 22 cm, allowing it to longitudinally contain an electromagnetic shower ($\sim$ 24 X_0), while its section is $\sim 3 \times 3$ cm^2 from one side and $\sim 2 \times 2$ cm^2 from the other. One of the largest faces of the crystal is unpolished, while all the remaining ones are mirror-polished. All faces not read out by PMTs were wrapped in several layers of Teflon.

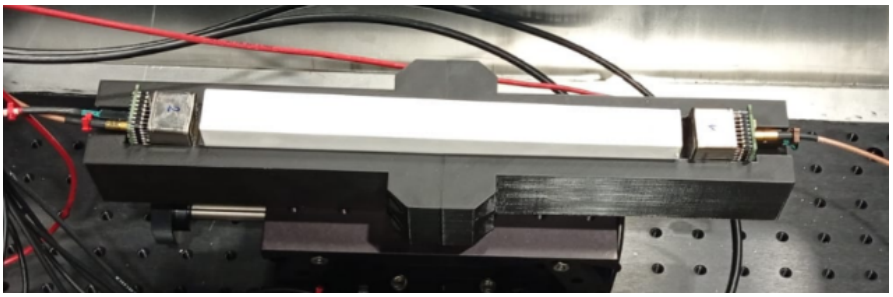

Figure 10.1: Picture of one of the configurations tested in the 2022 campaign. The $PbWO_4$ crystal, wrapped in multiple layers of Teflon is read out by two Hamamatsu R11187 PMTs from both its ends. Crystal and PMTs are housed in a 3D-printed holder to keep the prototype aligned with the beam axis.

In 2022 testbeam, two Hamamatsu R11187 PMTs were coupled to both ends of the $PbWO_4$ crystal to detect the optical photons and convert them into an electronic signal. Optical filters to enhance either scintillation or Cherenkov photons collection were employed during some of the measurements performed.

On the contrary, for the 2023 testbeam studies, a photomultiplier tube (PMT) with a considerably faster time response was required. The selected detector was a Hamamatsu multianode PMT (model R7600U-M4), which was coupled to the $\sim 3 \times 3$ mm^2 face of the crystal using optical grease. This particular PMT features four distinct anodes, each capturing electrons generated by a quarter of the photocathode. Optical filters were coupled to three of these quarters, while one quarter remained unfiltered. Only the signals produced by the unfiltered quarter were considered for this study. Furthermore, prior to digitalization, the PMT output passed through an analog attenuator.

The $PbWO_4$ crystal and the PMTs were placed on a 3D-printed support and housed in the same light-tight box employed for the MIPs timing detectors studies (see Figure 10.1). Both the setup in front of the experimental box and the DAQ illustrated in detail in Section 8.1 were utilized also for these studies. The pulses produced by the PMTs were digitalized and recorded at 5 GS/s for offline analysis even in this case.

10.2 Forward-backward Anisotropy Studies

The first study conducted in 2022 testbeam was the investigation of forward-backward light anisotropy produced by electromagnetic and hadronic showers in a single $PbWO_4$ crystal. This investigation was realized in a similar way as performed by the DREAM collaboration [54] which used a matrix of $PbWO_4$ crystal, thus allowing to tilt their prototype to maximize Cherenkov photons collection while keeping enough radiation

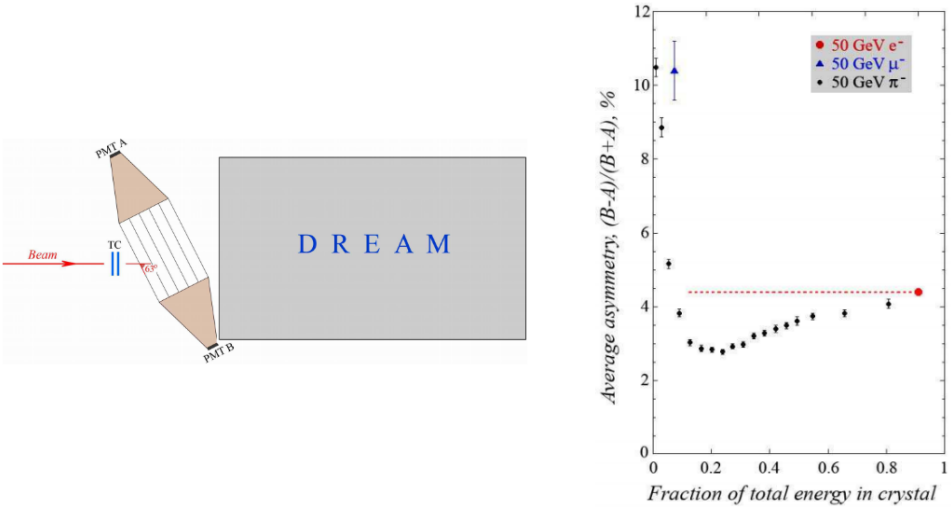

Figure 10.2: Left: schematics of the prototype tested by the DREAM collaboration. The $PbWO_4$ matrix is tilted to improve Cherenkov photons harvesting towards PMT B. Right: average forward-backward asymmetry as a function of the fraction of energy deposited in the prototype for 50 GeV electron, muon and pion beams. From reference [54].

lengths of material to contain a significant fraction of the shower (see Figure 10.2). However, as a single crystal was used in this study, the tilt of the prototype did not allow to properly contain the shower, and as a result, the crystal was irradiated along its main axis.

As previously discussed, Cherenkov light production presents a directional preference (about 63° in $PbWO_4$), in contrast with scintillation light which is isotropically emitted. For this reason, more Cherenkov light is expected to be detected from the back of the crystal. Since both front and back receive the same rate of scintillation light, the forward-backword anisotropy $(B-A)/(B+A)$, being A and B the energies deposited in the front and back detectors respectively, provides an estimation of the fraction of Cherenkov light.

As detailed described in [54], a correlation between the energy deposited by a hadronic shower in the ECAL and the fraction of Cherenkov light (thus the forward-backword anisotropy) may be expected, as observed for the data points associated with pions in Figure 10.2. As a matter of fact, in a thin and short calorimeter like the one tested, only the residual effects of the initial nuclear reactions during the development of a hadronic shower will be contained. Therefore, if the initial interaction occurs within the first centimetres of $PbWO_4$, it is likely that the π^0 particles generated in this first interaction point will release their energy in the crystal.

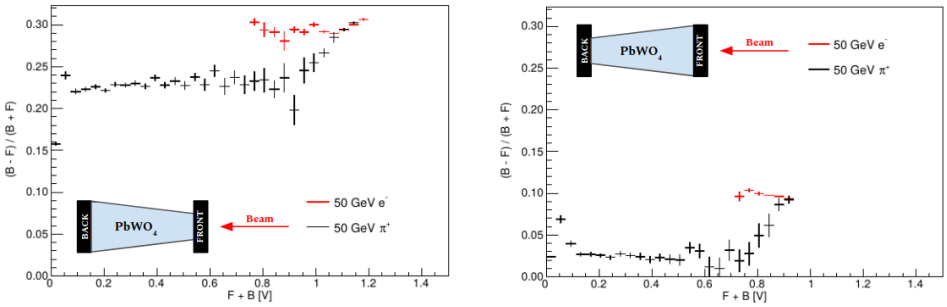

Figure 10.3: Forward-backward anisotropy profiles versus the sum $F + B$ of the signal amplitudes of the front and back PMTs for showers produced by 50 GeV electrons (in red) and pions (in black). Plots of both configurations in which the crystal was oriented are reported.

To perform this investigation, the R11187 PMTs were coupled to both ends of the crystal. Furthermore, the crystal was irradiated by placing in the front both the large and small sections in order to comprehend the impact of the light propagation due to the non-parallelepiped shape of the crystal. The prototype was irradiated both with electron and pion beams of 50 GeV/c transverse momentum.

Data analysis

In a similar way as illustrated for the charged particles timing detectors studies, the beam transverse crossing position was determined using the three DWCs. In all cases, only the events in which the incoming particle hit the central part of the crystal face were taken into account for the analysis.

For each event which passed the tracking selection, both the signal amplitudes F and B produced in the front and back detectors were extrapolated. The sum of the amplitude of the signals produced in both PMTs, which is proportional to the energy deposited by the shower, was determined event by event.

Results discussion

Figure 10.3 shows forward-backward anisotropy profiles against the sum of the front and back PMTs signal amplitudes obtained for showers generated either by electron or pion beams. These profiles were drawn for both configurations tested.

The trend observed in both plots at higher energies is in agreement with that observed by the DREAM collaboration [54]. On the other hand, a higher anisotropy due to Landau tail of pions penetrating the crystal would be expected at lower energies. This phenomenon was not observed due to the poor containment of the hadronic shower in the $PbWO_4$ crystal. Differences between the two configurations examined are clearly

related to the geometry of the crystal in which the shower containment is enhanced whether the smaller face is on the front.

10.3 Optical Filters Studies

During the 2022 testbeam campaign, in addition to performing forward-backward anisotropy tests, the potential to separately detect Cherenkov and scintillation light within the $PbWO_4$ crystal was explored. This investigation involved the use of dedicated optical filters and R11187 PMTs for light detection. More specifically, an optical filter with a transparency range of around 450 nm (with a 40 nm FWHM) to optimize the harvesting of $PbWO_4$ scintillation light was employed. In contrast, a filter with transparency above 550 nm was used to suppress scintillation emission and enhance the collection of Cherenkov photons.

For each test, a filter was placed between a PMT photocathode and one end of the crystal. It is worth noting that data acquisition was carried out by swapping the positions of the filters while consistently irradiating the crystal's smallest face.

In both test configurations, the crystal was exposed to 50 GeV electron and pion beams.

Data analysis

In a manner similar to the approach employed for the forward-backward anisotropy tests, the transverse crossing position of the beam was determined by utilizing data from the three DWCs. Even in this case, it is important to emphasize that, throughout the analysis, only events in which the incoming particle interacted with the central region of the crystal were taken into consideration.

For the events that met the tracking selection criterion, the signal amplitudes generated in both PMTs were measured. Initially, the average amplitudes $\langle C_e \rangle$ and $\langle S_e \rangle$ generated by events with the most effective containment of electromagnetic showers produced by the electron beam in the PMTs equipped with Cherenkov and scintillation filters, respectively, were evaluated. Subsequently, these average amplitudes served as normalization factors for the amplitude values C and S obtained from the two PMTs during each event under pion exposure.

Results discussion

The scatter plots, depicting the rescaled amplitudes acquired from both PMTs coupled to Cherenkov and scintillation filters under the exposure of 50 GeV electrons and pions, are illustrated in Figure 10.4. Distinct plots are presented for the two tested configurations.

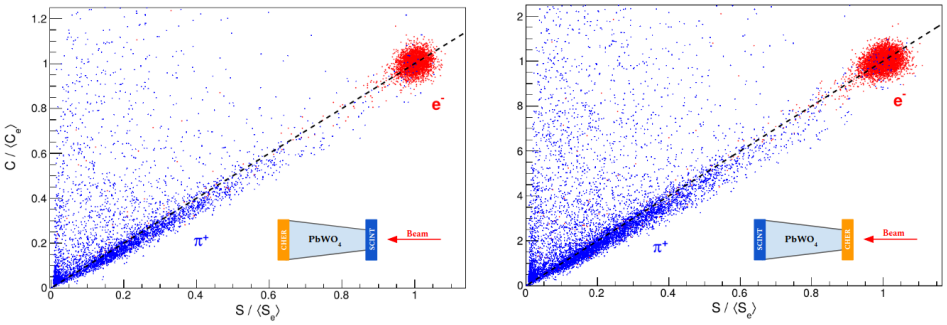

Figure 10.4: Scatter plots of the rescaled amplitude of the signals extracted by the PMTs with the Cherenkov (orange) and scintillation (blue) filters in front for events generated by 50 GeV electron and pion beam. Two different plots are provided for both configurations tested (sketched on the bottom right of each plot).

Given that Cherenkov photons are mostly directed towards the back face of the crystal, the data points for both electrons and pions exhibit greater dispersion in the right-hand plot.

The events associated with electromagnetic showers are concentrated around the coordinates (1,1) due to the applied normalization. On the other hand, points linked to hadronic showers predominantly cluster below the bisector, in accordance with simulation predictions. However, there are some data points above the bisector, associated with a significant Cherenkov signal and a low scintillation signal, whose physical explanation remains unclear.

The results obtained from these tests reveal that the conventional procedure employed by the DREAM collaboration to estimate the electromagnetic fraction discussed in Section 1.6, can not be effectively applied to a single $\sim$ $3 \times 3 \times 22$ cm^3 $PbWO_4$ crystal due to the poor containment of hadronic showers. For such a reason, it may be of interest to explore alternative methods for determining the electromagnetic fraction and correcting for energy losses incurred during hadronic showers, as detailed in the next chapter that outlines the 2023 testbeam campaign.

10.4 Pulse Discrimination with R7600U-M4 PMT

The main objective of the dual readout tests in the 2023 campaign was the identification of key parameters extrapolated from signal shapes produced by hadronic showers. These parameters could potentially offer insights into the electromagnetic fraction of events occurring within the $PbWO_4$ crystal. Subsequently, correlations among these features were explored and compared with simulation outputs.

To pursue this study, one of the fastest PMTs available on the market, the Hamamatsu R7600U-M4, was employed. This detector was grease-coupled to the largest end of the crystal and positioned on its back, opposite to the irradiation direction. 25 and 100 GeV electron beams and a 100 GeV pion beam were utilized for this study.

In order to better examine waveforms with low amplitudes primarily generated by pion showers with a poor electromagnetic fraction, an attenuator was employed. Initially, the PMT bias voltage and signal attenuation were fine-tuned to ensure that the average signal produced by a 100 GeV electron-induced shower closely approached the upper limit of the digitizer dynamic range. The values chosen for the PMT bias voltage and attenuation were 580 V and 20 dB, respectively. Subsequently, data acquisitions were performed while applying the 20 dB attenuation to the signals during both 25 GeV electron and 100 GeV pion beam measurements. Furthermore, the 100 GeV pion beam measurement was repeated without attenuation to better focus on events generating signals with a lower number of detected photons.

Data analysis

Similarly to the previous studies, only events occurring within the innermost region of the crystal were selected for analysis, guided by the transverse coordinates of the beam provided by the DWC.

Based on the simulation outputs illustrated in the previous chapter, several noteworthy features were extracted from the recorded pulses for analysis, as depicted in Figure 10.5. The initial features of interest include two integrals obtained by integrating the pulses over regions where either Cherenkov or scintillation light signals predominated over the other. To determine the signal start time t_0, a threshold at 15 % of the waveform height was established. Subsequently, a 4 ns integration window starting from t_0 was used to quantify the Cherenkov contribution C to the pulse, while an integration gate spanning from $t_0 + 10$ ns to $t_0 + 25$ ns was selected to estimate the scintillation light contribution S to the detected signal. Additionally, time-over-threshold values were computed pulse by pulse, with thresholds set at 20 % and 40 % of the pulse height.

Results discussion

Following a methodology similar to that described for the optical filters studies, the integrals over the Cherenkov and scintillation regions were normalized with respect to the average integrals produced by events characterized by optimal containment of 100 GeV electron-induced showers. These rescaled integrals were then plotted against each other for all the measurements conducted, as shown in Figure 10.6.

The cluster of data points associated with 100 GeV electrons is concentrated around the expected point (1,1). Conversely, data points from the waveforms generated by 25 GeV electrons are grouped around coordinates (0.3, 0.45), notably deviating from

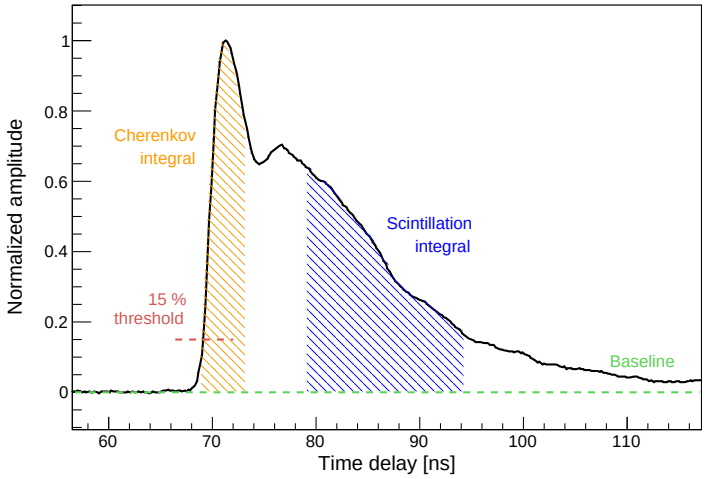

Figure 10.5: Example of a measured waveform obtained for a hadronic event. Some features of interest, e.g. threshold position, integrals over windows enhancing Cherenkov or scintillation detection, are highlighted in the plot.

the bisector. Possible explanations for this behaviour could be attributed to PMT non-linearity or cross-talk with the other three channels of the PMT. This deviation may also account for the distribution of events associated with hadronic showers, maintaining linearity for $S/\langle S_{\mathrm{e}}\rangle$ values less than 0.4. Consistently with the plot presented in Figure 10.4, some hadronic events are situated above the primary cluster of points.

The subsequent step in the data analysis involves an examination of potential correlations among the most significant features derived from the simulations conducted in the previous chapter. Figure 10.7 displays scatter plots of the C/S ratio against time-over-threshold values at 20 % and 40 % of the waveform amplitude. The data points related to electromagnetic showers exhibit precise clustering, whereas those linked to events induced by pion beams are more widely dispersed. For these points, a clear correlation is observable between the plotted quantities, with a stronger correlation emerging from the time-over-threshold at 20 %.

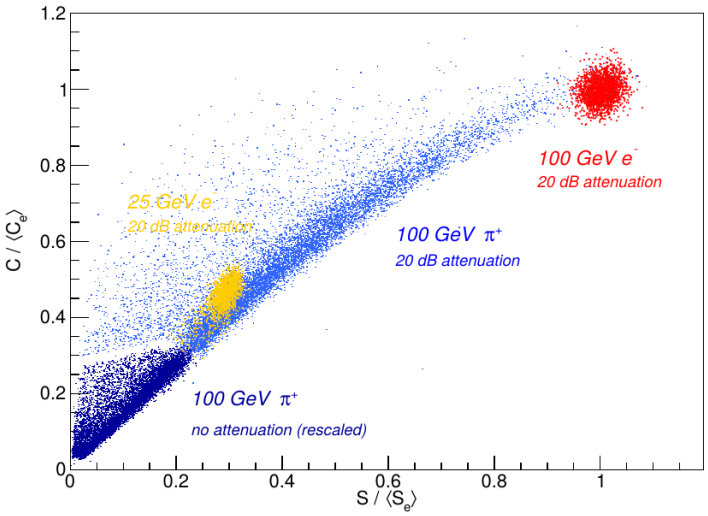

Figure 10.6: Scatter plot of the normalized integrals of the signal over the Cherenkov and scintillation regions. The red and orange cloud of points, associated with 100 and 25 GeV electron-induced shower events, are grouped around specific positions, while the events associated with hadronic showers generated by 100 GeV pions (in light and dark blue) are mainly clustered around a slightly bent line from the point (0,0) to (1,1).

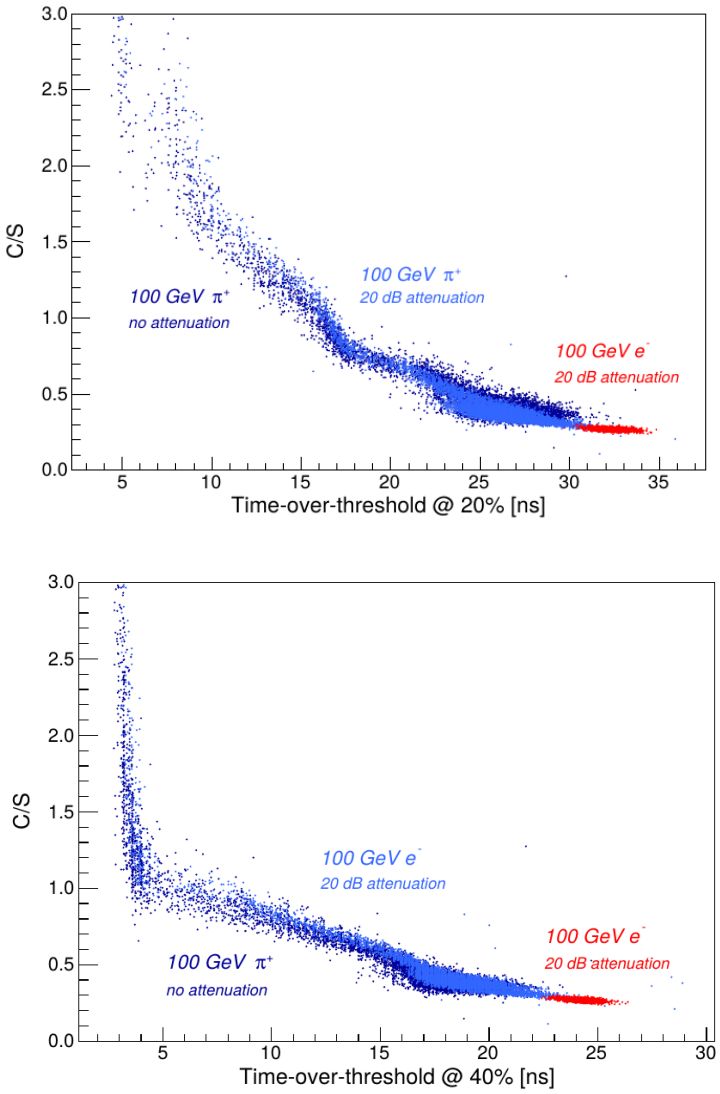

Figure 10.7: Scatter plot of the C/S ratio against the time-over-threshold at 20 % (top) and 40 % (bottom) for the measurements performed. The cloud of points related to electrons beam (in red) is clustered around a precise point, while the data points associated with pion-induced showers (in light - attenuated signal run - and dark blue - non-attenuated signal run) are more spread in the plots.

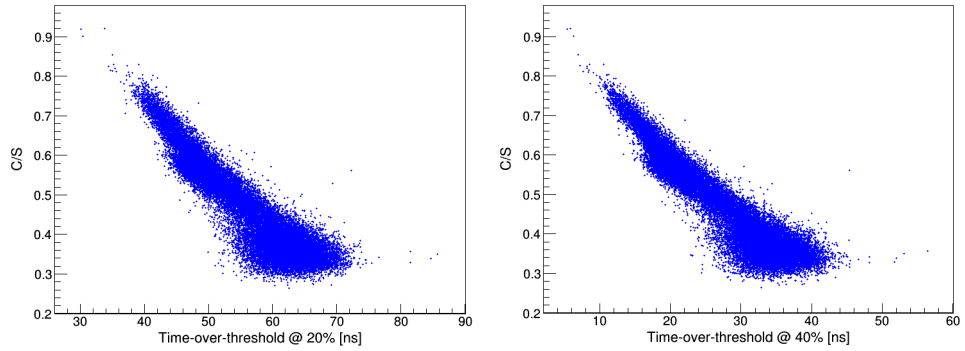

Figure 10.8: Scatter plot of the C/S ratio against the time-over-threshold at 20 % (left) and 40 % (right) obtained out of the simulated pulses produced by 20 GeV pions-induced showers.

10.4.1 Measurements-Simulations Matching

The interdependencies among the key features of the pulses derived from experimental testbeam data were subsequently compared to the simulation results generated using the Monte Carlo software detailed in the previous chapter. Similar scatter plots, as depicted in Figure 10.7, were also constructed to represent the C/S ratio against time-over-threshold values at 20 % and 40 %, drawing from simulated waveforms generated with incident pions (as shown in Figure 10.8).

Despite the differences in crystal geometry and energy scales between simulations and experimental measurements, an anticorrelation between the C/S ratio and the time-over-threshold values is observable in both scenarios.

10.5 Conclusions and Outlook

The aim of the conducted studies was to investigate the dual readout capability of a $PbWO_4$ crystal, capable of fully longitudinally containing an electromagnetic shower, but not a hadronic one. Both simulations and measurements revealed that the approach developed by the DREAM collaboration is not applicable in such cases due to significant hadronic shower leakages, both transversal and longitudinal.

In this thesis work, an alternative method for extracting information about the f_{em} of a hadronic shower using a PMT with fast response was proposed and tested through simulations and testbeam experiments. The results from the Monte Carlo framework showed a correlation between key waveform features and f_{em}. Concurrently, experimental data demonstrated a strong correlation among these features.

To better understand the feasibility of this method, further Monte Carlo simulations

are required to assess the effects on restoring hadronic response when combining information from the short electromagnetic $PbWO_4$ calorimeter on the front with that from a hadronic calorimeter with dual readout capability. Additionally, experimental tests with an improved setup, such as with the implementation of a matrix of $PbWO_4$ crystals and a rear-mounted hadronic calorimeter, are essential to validate the simulation results. One crucial quantity that could not be measured in our current setup was f_{em} itself. Nonetheless, in principle, by combining the electromagnetic fraction information provided by a hadronic calorimeter on the back with the energy deposition within the electromagnetic one, it may be possible to obtain information about f_{em}.

Part V

Conclusions and Outlook

Conclusions and Outlook

The goal of this PhD thesis was to explore innovative materials and fast light-generation processes with potential applications in high-energy experiments at future colliders.

This research was conducted in collaboration with the Crystal Clear Collaboration and the EP R&D at CERN, encompassing a diverse array of topics. These include the development and characterization of scintillating materials, the creation and utilization of Monte Carlo simulation frameworks and machine learning algorithms, along with the testing of promising detector concepts in testbeam activities.

The first facet of this thesis work involved the development and characterization of promising scintillating materials, primarily for their utilization in charged particle timing detectors and dual readout calorimetry. Initial research focused on measuring the scintillation and timing properties of mixed BGSO crystal samples which exhibited intermediate properties between pure BGO and BSO. This research was conducted in collaboration with the Czech Academy of Sciences (FZU) in Prague and the Institute for Scintillation Materials of NAS (ISMA) in Ukraine. The investigation revealed an optimal timing performance for samples with a Ge fraction ranging from 30 % to 50 %. Concurrently, the possibility to separate Cherenkov and scintillation light in BSO crystals was effectively demonstrated using dedicated optical filters opening the way for these materials for dual readout calorimetry applications.

Among scintillating crystals, BaF_2 stood out as one of the fastest due to its sub-nanosecond cross-luminescent emission. A characterization campaign was conducted on BaF_2 samples manufactured by SICCAS and doped with increasing concentrations of yttrium. This study yielded significant findings, including the increased suppression of the slow scintillation component with higher dopant concentrations and the independence of the timing performance achieved at 511 keV from the yttrium concentration. The excellent timing performance led to further investigation of the potential of these materials for use as charged particle timing layers. Additionally, the study also explored the use of dedicated optical filters to reduce the impact of the slow

component in BaF_2.

Furthermore, the thesis involved the characterization of key scintillating and timing properties of some hybrid organic-inorganic perovskite materials. This investigation yielded promising results in terms of timing and light output and particularly impressive time performance at 511 keV. These materials are well-suited for timing applications in calorimetry due to their cost-effectiveness and fast scintillation kinetics, although further work is necessary to produce larger samples with improved surface and internal characteristics.

The second major research focus of this thesis involved the design and testing of innovative prototypes based on the most promising scintillating materials currently available. The work encompassed two different research lines: charged particles timing detectors and dual readout calorimetry.

To explore the potential of various materials, a Monte Carlo simulation framework was developed, leading to the identification of several crystals with exceptional timing capability, including LSO:Ce,Ca, LYSO:Ce, GFAG, and BaF_2. The performance of these materials, along with many others, was subsequently evaluated under high-energy pions during two testbeam campaigns at CERN's SPS facility. In addition to conventional scintillation, this investigation delved into faster light generation processes, such as Cherenkov emission and cross-luminescence, with their light being detected using SiPM devices. The outcomes of these activities revealed that numerous materials achieved a single-detector time resolution of less than 20 ps (sigma), with the best result being achieved by LSO:Ce,Ca, which attained σ values as low as 12.1 ps. GFAG, highly codoped GAGG:Ce,Mg, BaF_2, and BaF_2:Y samples also demonstrated impressive performance comparable to LYSO:Ce, representing the leading material choice for the CMS barrel MIP timing detector.

The final study pursued in this thesis investigated the dual readout capability of a $PbWO_4$ crystal. Initially, the feasibility of applying the method developed by the DREAM collaboration was explored via Monte Carlo simulations involving crystals of varying sizes. However, it was observed that the DREAM method was not effective for smaller crystals incapable of adequately containing hadronic showers. Consequently, an alternative approach was investigated, focusing on the discrimination of pulse shapes using a significantly fast PMT to extract the electromagnetic fraction information. Subsequently, a crystal measuring approximately $3 \times 3 \times 22$ cm^3 was tested during two testbeam campaigns. The first campaign aimed to explore its forward-backward anisotropy and the possibility of achieving dual readout capability using optical filters. The second campaign concentrated on extracting key features, e.g. ratios between integrals over different time windows and time-over-thresholds, identified through simulations to investigate potential correlations among them. Nonetheless, further work, encompassing both simulation and experimental data acquisition, is needed to validate the applicability of this method.

Bibliography

[1] C. Fabjan and R. Wigmans. "Energy measurement of elementary particles". *Rep. Prog. Phys.* 52 (1989), p. 1519.

[2] C. W. Fabjan and F. Gianotti. "Calorimetry for particle physics". *Rev. Mod. Phys.* 75 (2003), pp. 1243–86.

[3] R. Wigmans. *Calorimetry: Energy Measurement in Particle Physics*. Oxford University Press, 2017.

[4] V. S. Murzin. *Progress in elementary particle and cosmic-ray physics*. Vol. 9. J. G. Wilson and I. A. Wouthuysen, eds., North Holland Publ. Co., Amsterdam, 1967, p. 247.

[5] P. B. Cushman. "Electromagnetic and hadronic calorimeters". In: *Instrumentation in High Energy Physics*. Ed. by F. Sauli. Vol. 9. Advanced Series on Directions in High Energy Physics. World Scientific, 1992, p. 281.

[6] B. Adeva *et al.* "The construction of the L3 experiment". *Nuclear Instruments and Methods in Physics Research Section A: Accelerators, Spectrometers, Detectors and Associated Equipment* 289.1 (1990), pp. 35–102.

[7] The CMS Collaboration. "The CMS electromagnetic calorimeter project: Technical Design Report". *Geneva: CERN* (1997).

[8] CMS Collaboration. "CMS Hadron Calorimeter Technical Design Report". *Geneva: CERN* (1997).

[9] ATLAS Collaboration. "ATLAS liquid-argon calorimeter: Technical Design Report". *Geneva: CERN* (1996).

[10] O. Ganel and R. Wigmans. "On the calibration of longitudinally segmented calorimeter systems". *Nuclear Instruments and Methods in Physics Research Section A* 409.1 (1998), pp. 621–8.

[11] Particle Data Group. "Review of Particle Physics". *Progress of Theoretical and Experimental Physics (PTEP)* 083C01 (2022).

[12] R. Wigmans. "Advances in Hadron Calorimetry". *Annual Review of Nuclear and Particle Science* 41 (1991), p. 133.

[13] D. Acosta *et al.* "Lateral shower profiles in a lead/scintillating fiber calorimeter". *Nuclear Instruments and Methods in Physics Research Section A: Accelerators, Spectrometers, Detectors and Associated Equipment* 316.2 (1992), pp. 184–201.

[14] N. Akchurin *et al.* "Beam test results from a fine-sampling quartz fiber calorimeter for electron, photon and hadron detection". *Nuclear Instruments and Methods in Physics Research Section A: Accelerators, Spectrometers, Detectors and Associated Equipment* 399.2 (1997), pp. 202–226.

[15] R. Wigmans. "New Developments in Calorimetric Particle Detection". *Progress in Particle and Nuclear Physics* 103 (2018), pp. 109–161.

[16] CMS Collaboration. "Particle Flow Calorimetry". *J. Phys. Conf. Ser.* 110 (2008), p. 092032.

[17] U. Amaldi. "Fluctuations in Calorimetry Measurements". *Physica Scripta* 23.4A 409 (1981).

[18] The ZEUS Calorimeter Group. "Response of a uranium-scintillator calorimeter to electrons, pions and protons in the momentum range 0.5–10 GeV/c". *Nuclear Instruments and Methods in Physics Research Section A: Accelerators, Spectrometers, Detectors and Associated Equipment* 290.1 (1990), pp. 95–108.

[19] N. Akchurin *et al.* "Hadron and jet detection with a dual-readout calorimeter". *Nuclear Instruments and Methods in Physics Research Section A: Accelerators, Spectrometers, Detectors and Associated Equipment* 537.3 (2005), pp. 537–561.

[20] M. Livan S. Lee and R. Wigmans. "Dual-readout calorimetry". *Reviews of Modern Physics* 90.2 (2018).

[21] "High-Luminosity Large Hadron Collider (HL-LHC): Technical Design Report". *Geneva: CERN* (2020).

[22] W. Herr and B. Muratori. "Concept of luminosity". *Geneva: CERN* (2006).

[23] CMS Collaboration. "A MIP Timing Detector for the CMS Phase-2 Upgrade: Technical Design Report". *Geneva: CERN* (2019).

[24] P. Lecoq *et al. Inorganic Scintillators for Detector Systems.* Springer Cham: Springer International Publishing Switzerland 2017, 2016, pp. 1–41.

[25] K. Pauwels *et al.* "Effect of aspect ratio on the light output of scintillators". *IEEE Transactions on Nuclear Science* 59.5 (2012), pp. 2340–2345.

[26] M. Conti. "State of the art and challenges of time-of-flight PET". *Physica Medica: European Journal of Medical Physics* 25.1 (2009), pp. 1–11.

[27] P. Lecoq *et al.* "Roadmap toward the 10 ps time-of-flight PET challenge". *Physics in Medicine & Biology* 65.21 (2020), 21RM01.

[28] P. A. Rodnyi *et al.* "Energy loss in inorganic scintillators". *physica status solidi (b)* 187.1 (1995), pp. 15–29.

[29] J. B. Birks. "Scintillations from organic crystals: Specific fluorescence and relative response to different radiations". *Proceedings of the Physical Society. Section A* 64.10 (1951), p. 874.

[30] P. A. Rodnyi. *Physical Processes in Inorganic Scintillators*. CRC Press LLC, 1997. Chap. 3.
[31] P. A. Rodnyi. "Core-valence luminescence in scintillators". *Radiation Measurements* 38.4 (2004), pp. 343–352.
[32] C. van Eijk. "Cross-luminescence". *Journal of Luminescence* 60-61 (1994), pp. 936–41.
[33] T. Ikeda *et al.* "Electronic structure of alkaline-earth fluorides studied by model clusters. ii. auger-free luminescence". *Journal of the Physical Society of Japan* 66.4 (1997), pp. 1079–87.
[34] R. H. Pots *et al.* "Exploiting cross-luminescence in BaF_2 for ultrafast timing applications using deep-ultraviolet sensitive HPK silicon photomultipliers". *Front Phys* 8 (2020), p. 482.
[35] O. Ganel and R. Wigmans. "Quartz fiber calorimetry for LHC experiments". *Nuclear Instruments and Methods in Physics Research Section A* 365 (1995), p. 360.
[36] P. Gorodetzky *et al.* "Quartz fiber calorimetry". *Nuclear Instruments and Methods in Physics Research Section A: Accelerators, Spectrometers, Detectors and Associated Equipment* 361.1 (1995), pp. 161–79.
[37] M. Lundin. "On the electromagnetic energy resolution of Cherenkov-fiber calorimeter". *Nuclear Instruments and Methods in Physics Research Section A* 372 (1996), p. 359.
[38] A. Penzo *et al.* "The CMS-HF quartz fiber calorimeters". *Journal of Physics: Conference Series* 160 (2009), p. 012014.
[39] L. M. Bollinger and G. E. Thomas. "Measurement of the time dependence of scintillation intensity by a delayed-coincidence method". *Review of Scientific Instruments* 32.9 (1961), pp. 1044–50.
[40] S. Derenzo *et al.* "Measurements of the intrinsic rise times of common inorganic scintillators". *IEEE Transactions on Nuclear Science* 47.3 (2000), pp. 860–64.
[41] S. Seifert *et al.* "Accurate measurement of the rise and decay times of fast scintillators with solid-state photon counters". *Journal of Instrumentation* 7.09 (2012), P09004.
[42] S. Gundacker *et al.* "Precise rise and decay time measurements of inorganic scintillators by means of x-ray and 511 keV excitation". *Nuclear Instruments and Methods in Physics Research Section A: Accelerators, Spectrometers, Detectors and Associated Equipment* 891 (2018), pp. 42–52.
[43] S. Gundacker *et al.* "Measurement of intrinsic rise times for various L(Y)SO and LuAG scintillators with a general study of prompt photons to achieve 10 ps in TOF-PET". *Physics in Medicine & Biology* 61.7 (2016), p. 2802.
[44] F. Anghinolfi *et al.* "NINO: an ultrafast low-power front-end amplifier discriminator for the time-of-flight detector in the ALICE experiment". *IEEE Transactions on Nuclear Science* 51 (2004), pp. 1974–8.

[45] S. Gundacker *et al.* "Time of flight positron emission tomography towards 100 ps resolution with L(Y)SO: an experimental and theoretical analysis". *Journal of Instrumentation* 8 (2013), P07014.
[46] S. Gundacker *et al.* "High-frequency SiPM readout advances measured coincidence time resolution limits in TOF-PET". *Physics in Medicine & Biology* 64.5 (2019), p. 055012.
[47] J. W. Cates *et al.* "Improved single photon time resolution for analog SiPMs with front end readout that reduces influence of electronic noise". *Physics in Medicine & Biology* 63 (2013), p. 185022.
[48] S. Vinogradov. "Approximations of coincidence time resolution models of scintillator detectors with leading edge discriminator". *Nuclear Instruments and Methods in Physics Research Section A: Accelerators, Spectrometers, Detectors and Associated Equipment* 912 (2018), pp. 149–53.
[49] S. Gundacker *et al.* "Experimental time resolution limits of modern SiPMs and TOF-PET detectors exploring different scintillators and Cherenkov emission". *Physics in Medicine & Biology* 65.2 (2020), p. 025001.
[50] P. Gianotti on behalf of the PADME collaboration. "The calorimeters of the PADME experiment". *Nucl. Instrum. Methods A* 936 (2019), pp. 150–151.
[51] R. Wigmans. "Energy measurement at the TeV scale". *New J. Phys.* 10 (2008), p. 025003.
[52] A. Gola *et al.* "NUV-sensitive silicon photomultiplier technologies developed at Fondazione Bruno Kessler". *Sensors* 19 (2019), p. 308.
[53] M. T. Lucchini *et al.* "New perspectives on segmented crystal calorimeters for future colliders". *J. Instrum.* 15 (2020), P11005.
[54] N. Akchurin *et al.* "Separation of crystal signals into scintillation and Cherenkov components". *Nucl. Instrum. Methods A* 599 (2008), p. 359.
[55] N. Akchurin *et al.* "A comparison of BGO and BSO crystals used in dual-readout mode". *Nucl. Instrum. Methods A* 640 (2011), pp. 91–8.
[56] M. Ishii *et al.* "Development of BSO (Bi_4Si_3O12) crystal for radiation detector". *Opt. Mater.* 19 (2002), pp. 201–12.
[57] F. Yang *et al.* "A study on radiation damage in BGO and PWO-II crystals". *J. Phys.: Conf. Ser.* 404 (2012), p. 012025.
[58] F. Yang *et al.* "BSO crystals for the HHCAL detector concept". *J. Phys.: Conf. Ser.* 587 (2015), p. 012064.
[59] E. Galenin *et al.* "Engineering of mixed $Bi_4(Ge_xSi_{1-x})_3O_{12}$ scintillation crystals". *Funct. Mater.* 22 (2015), pp. 423–8.
[60] R. Cala' *et al.* "Characterization of mixed $Bi_4(Ge_xSi_{1x})_3O_12$ for crystal calorimetry at future colliders". *Nuclear Instruments and Methods in Physics Research Section A: Accelerators, Spectrometers, Detectors and Associated Equipment* 1032 (2022), p. 166527.
[61] A. Gektin and A. Vasil'ev. "Scintillator energy resolution and a way to improve it by kinetic waveform analysis". *Radiat. Meas.* 122 (2019), pp. 108–114.

[62] S. E. Brunner and D. R. Schaart. "BGO as a hybrid scintillator / Cherenkov radiator for cost-effective time-of-flight PET". *Phys. Med. Biol.* 62 (2017), p. 4421.
[63] N. Kratochwil *et al.* "Pushing Cherenkov PET with BGO via coincidence time resolution classification and correction". *Phys. Med. Biol.* 65 (2020), p. 115004.
[64] N. Kratochwil *et al.* "Exploring Cherenkov Emission of BGO for TOF-PET". *IEEE Transactions on Radiation and Plasma Medical Sciences* 5.5 (2020), pp. 619–629.
[65] M. R. Furukhi *et al.* "Barium fluoride as a gamma ray and charged particle detector". *IEEE Trans Nucl Sci* 18 (1971), pp. 200–204.
[66] N. N. Ershov *et al.* "Spectral-kinetic study of the intrinsic-luminescence characteristics of a fluorite-type crystal". *Optic Spectrosc* 18 (1982), pp. 200–204.
[67] J. Andriessen *et al.* "Electronic structure and transition probabilities in pure and Ce^{3+} doped BaF_2, an explorative study". *Molecular Physics* 74.3 (1991), pp. 535–546.
[68] P. Dorenbos *et al.* "Absolute light yield measurements on BaF_2 crystals and the quantum efficiency of several photomultiplier tubes". *IEEE Trans Nucl Sci* 40 (1993), pp. 424–430.
[69] Z. W. Bell *et al. Handbook of Particle Detection and Imaging.* Scintillation Counters. In: Grupen, C., Buvat, I. 2nd edn. Berlin, Springer, 2012.
[70] R. Novotny. "The BaF_2 Photon Spectrometer TAPS". *IEEE Trans Nucl Sci* 38.2 (1991).
[71] R. Y. Zhu. "On quality requirements to the barium fluoride crystals". *Nucl Instrum Methods Phys Res Sect A Accel Spectrom Detect Assoc Equip* 340.3 (1994), pp. 442–57.
[72] S. Diehl *et al.* "Readout concepts for the suppression of the slow component of $BaF_2$for the upgrade of the TAPS spectrometer at ELSA". *J Phys Conf Ser* 587 (2015), p. 012044.
[73] C. Hu *et al.* "Development of Yttrium Doped BaF_2 Crystals for Future HEP Experiments". *IEEE Trans Nucl Sci* 66 (2019), pp. 1854–1860.
[74] S. Gundacker *et al.* "Vacuum ultraviolet silicon photomultipliers applied to BaF_2 cross-luminescence detection for high-rate ultrafast timing applications". *Phys Med Biol* 66.114002 (2021).
[75] K. Herweg *et al.* "On the Prospects of BaF_2 as a Fast Scintillator for Time-of-Flight Positron Emission Tomography Systems". *IEEE Trans Rad and Plasma Med Sci* 7.3 (2023), pp. 241–52.
[76] A. Jamil *et al.* "VUV-Sensitive Silicon Photomultipliers for Xenon Scintillation Light Detection in nEXO". *IEEE Trans Nucl Sci* 65.11 (2018), pp. 2823–33.
[77] P. Ferrario on behalf of PETALO collaboration. "Status and perspectives of the PETALO project". *J Instrum* 17.01 (2022), p. C01057.

[78] G. Gallina *et al.* "Characterization of the Hamamatsu VUV4 MPPCs for nEXO". *Nucl Instrum Methods Phys Res Sect A Accel Spectrom Detect Assoc Equip* 940 (2019), pp. 371–379.
[79] P. Rodnyi *et al.* "Radiative core-valence transitions in barium-based fluorides". *J Lumin* 47 (1991), pp. 281–284.
[80] R. Nepomnyashchikh *et al.* "Defect formation in BaF_2 crystals doped with cadmium". *Nucl Instrum Methods Phys Res Sect A* 537 (2005), pp. 27–30.
[81] J. Chen *et al.* "Slow scintillation suppression in yttrium doped BaF_2 crystals". *IEEE Trans Nucl Sci* 65 (2018), pp. 2147–2151.
[82] G. Shwetha *et al.* "$CsMgCl_3$: A Promising Cross Luminescence Material". *Journal of Solid State Chemistry* 227 (2015), pp. 110–6.
[83] G. Shwetha and V. Kanchana. "Impurity Induced Cross Luminescence in $KMgCl_3$: An Ab Initio Study". *Journal of Physics: Condensed Matter* 31 (2019), p. 115501.
[84] E. Melchakov *et al.* "Radiative Core-Valence Transitions in CsCl and $CsCaCl_3$". *Fiz. Tverd. Tela* 31 (1989), pp. 276–8.
[85] M. A. Macdonald *et al.* "Radiative Core-Valence Transitions in $CsMgCl_3$ and $CsSrCl_3$". *Journal of Luminescence* 65 (1995), pp. 19–23.
[86] K. Sugawara *et al.* "Luminescence and Scintillation Properties of Ce-doped Cs_2ZnCl_4 Crystals". *Opt. Mater.* 41 (2014).
[87] K. Takahashi *et al.* "Luminescence and Scintillation Properties of Cs_2ZnCl_4 and Cs_3ZnCl_5". *Jpn. J. Appl. Phys.* 59 (2020), p. 072002.
[88] V. Vaněček *et al.* "Ultraviolet Cross-Luminescence in Ternary Chlorides of Alkali and Alkaline-Earth Metals". *Optical Materials: X* 12 (2021), p. 100103.
[89] Y. Chornodolskyy *et al.* "Features of the Core–Valence Luminescence and Electron Energy Band Structure of $A_{1-x}Cs_xCaCl_3$ (A = K,Rb) Crystals". *Journal of Physics: Condensed Matter* 19 (2007), p. 476211.
[90] D. B. Mitzi. "Introduction: Perovskites". *Chemical Reviews* 119.5 (2019), pp. 3033–5.
[91] W. Yin *et al.* "Unique Properties of Halide Perovskites as Possible Origins of the Superior Solar Cell Performance". *Advanced Materials (Weinheim, Germany)* 26.27 (2014), pp. 4653–8.
[92] C. Katan *et al.* "Quantum and Dielectric Confinement Effects in Lower-Dimensional Hybrid Perovskite Semiconductors". *Chemical Reviews* 119.5 (2019), pp. 3140–92.
[93] K. Shibuya *et al.* "Scintillation properties of $(C_6H_{13}NH_3)_2PBI_4$: Exciton luminescence of an organic/inorganic multiple quantum well structure compound induced by 2.0 MeV protons". *Nucl. Instrum. Methods. Phys. Res., Sect. B* 194 (2002), pp. 207–212.
[94] C. W. van Eijk *et al.* "Scintillation properties of a crystal of $(C_6H_5(CH_2)_2NH_3)_2PbBr_4$". In: *IEEE Nuclear Science Symposium Conference Record, NSS/MIC*. IEEE. 2008, pp. 3525–8.

[95] J. Y. Kim *et al.* "High-efficiency perovskite solar cells". *Chem. Rev.* 120 (2020), pp. 7867–918.
[96] L. Jonathan *et al.* "Hybrid organic–inorganic perovskite halide materials for photovoltaics towards their commercialization". *Polymers* 14 (2022), p. 1059.
[97] M. D. Birowosuto *et al.* "X-ray scintillation in lead halide perovskite crystals". *Sci. Rep.* 6 (2016), p. 37254.
[98] N. Kawano *et al.* "Scintillating organic-inorganic layered perovskite-type compounds and the gamma-ray detection capabilities". *Sci. Rep.* 7 (2017), p. 14754.
[99] A. Xie *et al.* "Library of two-dimensional hybrid lead halide perovskite scintillator crystals". *Chem. Mater.* 32 (2020), pp. 8530–9.
[100] F. Maddalena *et al.* "Effect of commensurate lithium doping on the scintillation of two-dimensional perovskite crystals". *J. Mater. Chem. C* 9 (2021), pp. 2504–12.
[101] R. Cala' *et al.* "Sub-100-picosecond time resolution from undoped and Li-doped two-dimensional perovskite scintillators". *Appl. Phys. Lett.* 120.24 (2022), p. 241901.
[102] D. Kowal *et al.* "PEA_2PbI_4: fast two-dimensional lead iodide perovskite scintillator with green and red emission". *Materials Today Chemistry* 29 (2023), p. 101455.
[103] M. A. Sheikh *et al.* "A_2Bn (A = BA, PEA; B = MA; n = 1, 2): Engineering Quantum-Well Crystals for High Mass Density and Fast Scintillators". *The Journal of Physical Chemistry C* 127.22 (2023), pp. 10737–47.
[104] A. Xie *et al.* "Lithium-doped two-dimensional perovskite scintillator for wide-range radiation detection". *Commun. Mater.* 1 (2020), p. 37.
[105] S. Agostinelli *et al.* "GEANT4–a simulation toolkit". *Nucl. Instrum. Meth. A* 506.25 (2003), p. 0.
[106] M. Janeceka and W. Moses. "Simulating scintillator light collection using measured optical reflectance". *IEEE Transactions on Nuclear Science* 57.3 (2010), pp. 964–70.
[107] A. Levin and C. Moisan. "A more physical approach to model the surface treatment of scintillation counters and its implementation into DETECT". In: *1996 IEEE Nuclear Science Symposium. Conference Record.* Vol. 2. IEEE. 1996, pp. 702–6.
[108] L. Martinazzoli *et al.* "Scintillation properties and timing performance of state-of-the-art $Gd_3Al_2Ga_3O_{12}$ single crystals". *Nuclear Instruments and Methods in Physics Research, Section A: Accelerators, Spectrometers, Detectors and Associated Equipment* 1000 (2021).
[109] A. Benaglia *et al.* "Detection of high energy muons with sub-20 ps timing resolution using L(Y)SO crystals and SiPM readout". *Nucl Instrum Methods Phys Res Sect A Accel Spectrom Detect Assoc Equip* 830 (2016), pp. 30–35.

[110] M. T. Lucchini *et al.* "Timing capabilities of garnet crystals for detection of high energy charged particles". *Nucl Instrum Methods Phys Res Sect A Accel Spectrom Detect Assoc Equip* 852 (2017), pp. 1–19.

[111] D. Banerjee *et al.* "The North Experimental Area at the Cern Super Proton Synchrotron" (2021).

[112] S. Ritt. "Design and performance of the 6 GHz waveform digitizing chip DRS4". In: *2008 IEEE Nuclear Science Symposium Conference Record*. 2008, pp. 1512–5.

[113] W. Klamra *et al.* "Properties of optical greases for BaF_2 scintillators". *Nucl Instrum Methods Phys Res Sect A Accel Spectrom Detect Assoc Equip* 254 (1987), pp. 85–87.

[114] L. Martinazzoli *et al.* "Compositional engineering of multicomponent garnet scintillators: towards an ultra-accelerated scintillation response". *Mater Adv* 3 (2022), pp. 6842–52.

[115] *Eljen technology EJ232 datasheet*. URL: https://eljentechnology.com/images/products/data_sheets/EJ-232_EJ-232Q.

[116] N. Kratochwil *et al.* "A roadmap for sole Cherenkov radiators with SiPMs in TOF-PET". *Physics in Medicine & Biology* 66.19 (2021), p. 195001.

[117] R. Cala' *et al. Exploring BaF2:Y Ultra-fast Emission for Future HEP Applications*. 2022.

[118] B. Sigfridsson. "Theoretical analysis of time resolution in scintillation detectors". *Nucl Instrum Methods* 54 (1967), pp. 13–28.

Acknowledgements

This three-year journey I embarked on had its fair share of ups and downs, but it provided me with invaluable opportunities to meet with incredibly smart and kind people from whom gleaned not only professional knowledge but also valuable life lessons. Moreover, I was fortunate to receive unwavering support from friends I had known before starting this unique adventure, as well as, naturally, from my family.

First, I want to thank my supervisor, Prof. Marco Paganoni, for his belief in me and for affording me the opportunity to undertake this research. I also want to express my deepest gratitude to Dr. Etiennette Auffray for welcoming me into the Crystal Clear Group at CERN and for her professional guidance and personal support throughout these three years. I am sincerely thankful to my tutor, Prof. Marco Pizzichemi, for his sage advice and for sharing part of his experience with me.

Moving to my colleagues, my profound acknowledgements go to Loris and Nicolaus, always ready to provide insightful answers to my novice questions about laboratory and testbeam measurements, and for introducing me to scintillating materials, silicon detectors and crystal calorimetry. A special mention is reserved for Giulia, for her friendship, and personal and practical support during most of my time at CERN. My gratitude also extends to Fiammetta, with whom I have shared daily challenges since we embarked on our journey at CERN together, and Isa, for engaging conversations as office neighbours and for her "hardware" support. Of course, I am also thankful to everyone I met who has worked or is currently working at CERN building 27, as their daily chats created a delightful and intellectually stimulating atmosphere.

I want to deeply thank my family for their support throughout my PhD. In particular, I want to express my gratitude to my parents and my brother for their belief in me and for backing me right from the very beginning and, especially, during these three crucial years.

Last but not least, I want to express my thanks to my lifelong friends, Leyla, Nicolò, Claudio, Emanuela, Gennaro, Giuliano, Paoloalberto, Pier Claudio, and Pier Domenico, for their enduring friendship and support throughout these years. They have always made me feel at home each time that "scendo giù".